

# **A Review and Detailed Investigation of Continuum-Based Numerical Modelling Methods for the Simulation of Brittle Rock Failure Around Underground Excavations**

by

Luis Fernando Gomez de Alba

Submitted in partial fulfilment of the requirements  
for the degree of Master of Applied Science

at

Dalhousie University  
Halifax, Nova Scotia  
July 2024

Dalhousie University is located in Mi'kma'ki, the  
ancestral and unceded territory of the Mi'kmaq.  
We are all Treaty people.

# TABLE OF CONTENTS

TABLE OF CONTENTS .....	ii
LIST OF TABLES .....	vi
LIST OF FIGURES.....	viii
ABSTRACT .....	xv
LIST OF ABBREVIATIONS AND SYMBOLS USED.....	xvi
ACKNOWLEDGEMENTS .....	xix
CHAPTER 1 - INTRODUCTION .....	1
1.1 Background .....	1
1.2 Objectives and Methodology.....	8
1.3 Document Overview.....	9
CHAPTER 2 - LITERATURE REVIEW .....	11
2.1 Empirical Methods .....	11
2.1.1 Stress-induced failure prediction .....	12
2.1.2 Depth of failure equation .....	12
2.1.3 Empirical equations of EDZ prediction.....	14
2.2 Continuum numerical methods .....	16
2.2.1 Hoek-Brown Brittle Parameters.....	17
2.2.2 Cohesion Weakening Friction Strengthening (CWFS).....	18
2.2.2.1 Application of the CWFS method.....	22
2.2.2.2 Guidelines for input parameters selection for the CWFS method .....	23
2.2.2.3 Modification of the Critical Plastic Strain Parameters .....	25
2.2.2.4 Instantaneous Cohesion Weakening Friction Strengthening .....	27
2.2.3 Damage Initiation Spalling Limit (DISL).....	29
2.2.3.1 Application of the DISL method.....	31
2.2.3.2 Realistic "as-built" tunnel boundary DISL method .....	32
2.2.3.3 The DISL method for interpreting the EDZ.....	33
2.2.4 <i>FRACOD</i> .....	35
2.2.5 2D Continuum-Based Voronoi Tessellated Models .....	38
2.3 Discontinuum numerical methods.....	41
2.3.1 Bonded Tetrahedral Block Model Method .....	41
2.3.2 The tetrahedral and Voronoi grain-based model method.....	43

2.3.3 The bonded-particle model method .....	46
2.3.4 The flat-jointed material method .....	49
2.4 Hybrid Finite-Discrete Numerical Methods.....	50
2.4.1 Mechanical Analysis and Interpretation of EDZ using IRAZU .....	51
2.4.2 Spalling Depth Prediction Using <i>ELFEN</i> Hybrid Code. ....	53
2.4.3 Imperial College Geomechanics Toolkit Finite Element-Based Discrete Fracture Growth.....	55
2.4.4 Blast-Induced EDZ Modelling Method with FDEM.....	58
2.4.5 Subspring Network Breakable Voronoi Model.....	60
2.5 Summary .....	61
CHAPTER 3 - A Sensitivity Study and Robustness Evaluation of the CWFS and DISL Approaches for Brittle Failure Continuum Modelling Around Underground Excavations .....	65
3.1 Abstract.....	65
3.2 Introduction .....	66
3.3 Background .....	68
3.3.1 Brittle Failure Around Underground Openings .....	68
3.3.2 CWFS and DISL Implementation in FLAC .....	73
3.3.3 The Mine-by Experiment tunnel at the Underground Research Laboratory.....	74
3.4 Overview of the Research Methodology.....	77
3.5 Unconfined and Confined Compression Test Simulations.....	81
3.5.1 Methodology for Laboratory Testing Simulations.....	81
3.5.2 Results for Laboratory Testing Simulations .....	82
3.6 Reproduction of the MBE at the URL Benchmark Modelling Cases .....	84
3.6.1 Methodology for the Benchmark Modelling Cases.....	85
3.6.2 MBE FLAC Model Setup.....	86
3.6.3 CWFS Results.....	87
3.6.4 DISL Results .....	88
3.7 Sensitivity Analysis of Strength Parameters .....	89
3.7.1 Strength Parameters Sensitivity Analysis Methodology.....	90
3.7.2 CWFS Strength Parameters Sensitivity Analysis .....	90
3.7.3 <i>DISL</i> Sensitivity Analysis .....	96

3.8 Sensitivity Analysis of Hypothetical In Situ Stress Magnitudes .....	100
3.8.1 Hypothetical Stress Scenario Sensitivity Analysis Methodology .....	100
3.8.2 CWFS Results .....	101
3.8.3 DISL Results .....	102
3.9 Discussion .....	103
3.10 Conclusion .....	105
CHAPTER 4 - Application of the CWFS method in FLAC2D to model brittle failure around the Qirehataer Diversion tunnel .....	107
4.1 Introduction .....	107
4.2 Background .....	108
4.3 Methodology .....	109
4.4 Results .....	110
4.5 Conclusion .....	113
CHAPTER 5 - <i>The IMASS method for brittle rock failure modelling in underground excavations</i> .....	114
5.1 Introduction .....	114
5.2 IMASS Overview .....	114
5.3 Methodology .....	117
5.3.1 IMASS constitutive model strength envelopes for brittle rock failure modelling .....	118
5.3.2 UCS and Triaxial Tests .....	120
5.3.3 Application to the MBE at the URL .....	122
5.3.4 Input strength parameters sensitivity analysis .....	124
5.3.5 Sensitivity Analysis of Hypothetical In Situ Stress Scenarios .....	125
5.4 Results .....	126
5.4.1 UCS and Triaxial Test .....	126
5.4.2 Application to the MBE at the URL .....	130
5.4.3 Input strength parameters sensitivity analysis .....	131
5.4.4 Sensitivity Analysis of Hypothetical In Situ Stress Scenarios .....	135
5.5 Preliminary set of guidelines for the use of the IMASS method .....	136
5.6 Application of the IMASS method to the Qirehataer Diversion Tunnel .....	137
5.6.1 Methodology .....	138
5.6.2 Calibration and Results .....	139

5.7 Conclusions and recommendations .....141

CHAPTER 6 - CONCLUSION .....143

6.1 Sensitivity Analysis and robustness evaluation of the CWFS and DISL  
Approaches .....143

6.2 Development and Evaluation of the IMASS Approach .....143

6.3 Recommendations and Future Work .....144

BIBLIOGRAPHY .....148

## LIST OF TABLES

Table 1-1 Selection of either the Hoek-Brown constitutive model or alternative brittle rock failure method given the GSI of the rock mass and the rock strength ratio ( $\sigma_{UCS}/\sigma_t$ ) (modified after Diederichs, 2007) .....	7
Table 2-1 EDZ characterization constant multipliers and correlation coefficients (modified after Perras and Diederichs, 2016).....	15
Table 2-2 Strength parameters to model the MBE at the URL using the CWFS method in FLAC (after Hajiabdolmajid et al., 2003) .....	22
Table 2-3 Strength parameters to model the MBE at the URL using the DISL method in Phase2 (after Diederichs, 2007) .....	32
Table 2-4 Strength and deformation properties of VTM in RS2 (Sanipour et al. 2022) .....	39
Table 2-5 Parameter selection for the strength of LdB granite using Voronoi and Tetrahedral Blocks for the grain-based model method (modified after Azocar, 2014) .....	45
Table 2-6 Parameters for LdB granite from laboratory experiments and bonded block particle method in PFC2D and PFC3D (modified after Potyondy and Cundall, 2004) .....	47
Table 2-7 Summary of methods to simulate EDZ around underground excavation in brittle rock.....	62
Table 3-1 The in-situ state of stress at the 420 L of the URL (Martin and Kaiser, 1996).....	75
Table 3-2 LdB intact rock properties using Hoek-Brown failure criterion (Martin and Kaiser, 1996).....	76
Table 3-3 LdB CWFS Material Properties (after Hajiabdolmajid et al. 2002).....	76
Table 3-4 LdB DISL Material Properties (after Diederichs, 2007) .....	77
Table 3-5 MBE measures of failure characterization from the field observation of the 420L (chainage unknown) from observations by Martin and Kaiser (1996) .....	80
Table 3-6 Influence of $\psi$ on the failure profile characteristics in the CWFS model.....	91
Table 3-7 Influence of $cp$ on the failure profile characteristics in the CWFS model .....	92
Table 3-8 Influence of $\phi_i$ on the failure profile characteristics in the CWFS model .....	93
Table 3-9 Influence of $cr$ on the failure profile characteristics in the CWFS model.....	94

Table 3-10 Influence of $\phi m$ on the failure profile characteristics in the CWFS model .....	95
Table 3-11 Influence of $ecps$ and $e\phi ps$ on the failure profile characteristics in the CWFS model .....	96
Table 3-12 Influence of $ecritps$ on the failure profile characteristics in the DISL model .....	97
Table 3-13 Influence of $\psi$ on the failure profile characteristics in the DISL model .....	98
Table 3-14 Influence of Hoek-Brown parameters on the failure profile characteristics in the DISL model .....	99
Table 4-1 Initial parameter selection for the gneissic granite at the Qirehataer Diversion Tunnel for CWFS modelling.....	110
Table 4-2 Calibrated model parameters for the gneissic granite at the Qirehataer Diversion Tunnel for CWFS modeling in FLAC2D. ....	113
Table 5-1 Preliminary IMASS input parameters for the MBE at the URL to obtain a DISL-like behaviour. ....	119
Table 5-2 Preliminary Hoek-Brown values of the peak and post-peak failure envelopes of the IMASS method for the MBE at the URL.....	120
Table 5-3 Range of parameters for the SA of the MBE at the URL using the IMASS method .....	125
Table 5-4 Principal stress values for the hypothetical stress scenarios using the IMASS method. ....	126
Table 5-5 Influence of $\sigma UCSinput$ on the failure profile characterization in the IMASS method.....	132
Table 5-6 Influence of $miinput$ on the failure profile characterization in the IMASS method .....	133
Table 5-7 Influence of $emultips$ on the failure profile characterization in the IMASS method.....	134
Table 5-8 Influence of $\phi b$ on the failure profile characterization in the IMASS method .....	135
Table 5-9 Geotechnical properties of the gneissic granite at the QDT (after Zhao et al., 2017; Zhao et al., 2022).....	138
Table 5-10 Preliminary estimates of the input parameters to simulate the QDT using the IMASS method .....	138

## LIST OF FIGURES

Figure 1-1 Multilayered design of the DGR proposed for the Forsmark site by SKB (modified after Elfving, et al, 2013) .....	2
Figure 1-2 Overview of EDZ nomenclature with a given stress regime for a) a tunnel excavated using the tunnel-boring machine method and b) a tunnel excavated using drill and blast method (after Siren et al. 2015) .....	5
Figure 1-3 Tunnels modes of instability and possible types of failure as a function of the ratio between in situ stresses and unconfined compressive strength, and RMR. In red are the possible occurrences of spalling failure in brittle rock investigated in this study. (modified after Kaiser et al. 2000) .....	6
Figure 2-1 Empirical observations of the depth of failure by Martin et al. (1999) and Diederichs et al. (2010) compared to the empirical prediction equation of $df$ by Martin, et al. (1999) .....	13
Figure 2-2 Comparison of the empirical relationship between $\sigma_{max}/\sigma_{UCS}$ and $Rf/a$ and the predicted values using elastic numerical models and the Hoek-Brown brittle parameters (modified after Martin et al., 1999) .....	17
Figure 2-3 Results from the laboratory investigation of LdB granite under cyclic loading a) cohesion weakening friction strengthening of a UCS sample compared to normalized damage b) CWFS mechanism visualized with Mohr circle in shear-normal stress space (modified after Martin and Chandler, 1994). .....	19
Figure 2-4 Relationship between shear strength component mobilization and excavation boundary fracturing process with respect to fracturing interactions and evolution. ....	20
Figure 2-5 The three distinct CWFS theoretical failure envelopes showing the correlation between the strength parameters $c$ and $\phi$ , and the critical plastic strains $e_{cps}$ and $e_{\phi ps}$ in $\sigma_1 - \sigma_3$ space. ....	21
Figure 2-6 Results of the application of the CWFS method to simulate the MBE using the strength parameters from Table 2-2 (after Hajiabdolmajid et al., 2003) .....	22
Figure 2-7 Results of the simulated triaxial test on LdB granite for 0 MPa, 5 MPa, and 10 MPa using the CWFS method in FLAC with a) linear and non-simultaneous plastic strain relationship b) non-linear and simultaneous plastic strain relationship (modified after Renani and Martin, 2018) .....	26
Figure 2-8 Results of the simulation and calibration of the modified CWFS method for a) the MBE, showing the observed failed profile, and b) the EES-M1, showing the approximated observed failed profiles (modified after Renani and Martin, 2018). .....	27



Figure 2-9 The DISL method theoretical s-shaped envelope in $\sigma_1 - \sigma_3$ space showing the three defining strength envelopes: crack initiation strength, spalling limit strength, and ultimate strength (modified after Diederichs, 2007).....	30
Figure 2-10 "Peak" and "Residual" strength envelopes in $\sigma_1 - \sigma_3$ space for the application of the DISL method in <i>RS2</i> , the zones of the strength increase, and strength decrease after plasticity, and the suggestions for input parameter selection (modified after Diederichs, 2007) .....	31
Figure 2-11 Application of the DISL method in <i>PHASE2</i> (now <i>RS2</i> ) to the MBE at the URL showing the predicted failure profile for the top section of the tunnel (modified after Diederichs, 2007) .....	32
Figure 2-12 a) As-built geometry and discretization of the MBE tunnel applied in <i>RS2</i> for the application of the DISL method. b) Result of the application of the DISL method with as-built geometry with input $\sigma_{UCS} = 0.8 \times \sigma_{UCS}$ showing a <i>df</i> comparable to the field observations (modified after Cai and Kaiser, 2014). .....	33
Figure 2-13 "Peak" and "Residual" strength envelopes in $\sigma_1 - \sigma_3$ space for the application of the DISL method in <i>RS2</i> showing the "problematic" zone where continuum numerical models show yielded elements, but the rock is not part of the HDZ, suggesting the need for an alternative interpretation of the HDZ using this tool. ....	34
Figure 2-14 Mechanical-Thermal-Fluid coupled interactions for the <i>FRACOD</i> BEM software (modified after Shen, 2014).....	36
Figure 2-15 Long-term equilibrium for a theoretical tunnel in Aspo diorite modelled with <i>FRACOD</i> demonstrating the type of fractures and the depth of failure simulated (modified after Barton and Shen, 2017). .....	37
Figure 2-16 Results of the simulation of the v-notch and EDZ at the MBE tunnel using the VTM method in <i>RS2</i> compared to the field observations of failure and micro-seismic event measurements (modified from Sanipour et al., 2022).....	40
Figure 2-17 a) Spalling results for a tunnel using the tetrahedral block model method in <i>3DEC</i> (modified after Garza-Cruz et al., 2014) b) Displacement of the tunnel's left wall with respect of change in support pressure (modified after Garza-Cruz et al., 2014). .....	43
Figure 2-18 Results of the simulation of the MBE at the URL in <i>3DEC</i> with a) Tetrahedral grain-based block model (modified after Azocar, 2014) b) Voronoi grain-based block model (modified after Azocar, 2014) c) compared to the field observations of the field observation (modified after Martin, 1997) .....	45
Figure 2-19 Crack initiation strength envelopes and Ultimate strength envelopes for LdB granite for laboratory tests and PFC simulations with the bonded-block particle method (modified after Potyondy and Cundall, 2004).....	47

Figure 2-20 Modelling results of the MBE tunnel using the bonded-block model method using PFC with a) original bond strength and b) reduced bond strength by a factor of 0.5 (modified after Potyondy and Cundall, 2004) .....	48
Figure 2-21 Theory of the arrangement of particles and bonds for the flat-joint method for a) two particles b) crystalline arrangement of particles in <i>PFC2D</i> (modified after Potyondy, 2015).....	49
Figure 2-22 Simulation results of the Aspö experiment with the flat-jointed material method showing the spalling zone and the EDZ (modified after Potyondy and Mas Ivars, 2020).....	50
Figure 2-23 Methodology for the calibration of micro-mechanical properties for excavations in brittle rock modelling in <i>IRAZU</i> (modified after Vazaios et al., 2017) .....	52
Figure 2-24 a) Results of the modelling of the MBE at the URL using <i>IRAZU</i> after micromechanical calibration (modified after Vazaios et al., 2017) compared to b) fields observations of v-notch formation at the MBE (modified after Martin, 1997).....	53
Figure 2-25 Initiation of spalling near an excavation due to fracture interaction of pre-existing defects in the rock mass (after Hamdi et al., 2017) .....	54
Figure 2-26 a) Results of the MBE modelling using calibrated values in <i>ELFEN</i> showing plastic strain and fracturing (modified after Hamdi et al., 2017) compared to b) fields observations of v-notch formation at the MBE (modified after Martin, 1997).....	55
Figure 2-27 a) Results of the MBE modelling using calibrated values with the Imperial College Geomechanics Toolkit method showing fractures that have developed into a v-notch (modified after Săceanu et al., 2022) compared to b) fields observations of v-notch formation at the MBE (modified after Martin, 1997).....	57
Figure 2-28 Change in Young’s modulus due to fracture formation near an excavation in the Imperial College Geomechanics Toolkit (modified after Săceanu et al., 2022).....	57
Figure 2-29 a) Blasthole location to simulate line blasting for the use of the blast-induced EDZ modelling method b) results of the implementation of the blast-induced EDZ modelling method showing the HDZ location and depth and the EDZ <sub>CI</sub> location and depth (modified after An et al., 2020).....	59
Figure 2-30 SNBV results for modelling the MBE in LdB granite after micromechanical properties calibration to laboratory experiments showing the broken interfaces (left) and broken Voronoi blocks (right) compared to the observer failure at the MBE (modified after Potyondy and Fu, 2024).....	61
Figure 3-1 a) Loss of cohesion and increase in friction angle as a function of normalized damage from the experiments conducted by Martin and Chandler (1994) b) Conceptual representation of cohesion and friction mobilization as functions of	

rock damage and post-peak plastic strain around an underground excavation (Corkum et al., 2012).....	70
Figure 3-2 a) DISL theoretical Bi-Linear Strength Envelope (Diederichs, 2007) b) Application of the theoretical DISL strength envelope with initial (Damage Initiation) and residual (Spalling Limit) strength for continuum numerical models.....	72
Figure 3-3 Simplified MBE failure profile for the 420L (chainage unknown) after full development of the v-notch. The measures of failure were obtained by digitizing the original profile found in the literature (after Martin et al., 1997).....	75
Figure 3-4 General methodology for the comparison of sensitivity and robustness of CWFS and DISL using the URL MBE as a case study. ....	78
Figure 3-5 Graphical demonstration of the measures of failure for the roof of an underground excavation a) $df$ , angle of failure, and area of failure b) shape of failure classification and uncontrolled failure example .....	80
Figure 3-6 Model setup and geometry for unconfined and triaxial test using <i>FLAC</i> .....	82
Figure 3-7 Simulated triaxial test results in deviatoric stress and axial strain space using <i>FLAC</i> for the LdB granite according to a) CWFS suggested parameters and b) DISL suggested parameters. ....	83
Figure 3-8 Peak strength for the triaxial test simulation using CWFS and DISL parameters from literature compared to the theoretical peak and residual envelopes (determined from input parameters) of each approach.....	84
Figure 3-9 Model setup and simplified geometry for the URL MBE using <i>FLAC</i> with rotated stress orientations for simplicity showing the different zone densities. ....	86
Figure 3-10 <i>FLAC</i> results for the CWFS approach showing failure profile with vertical and horizontal stress orientations for a) Hajiabdolmajid, et al. (2002) results rotated to align v-notch with vertical and horizontal axis b) results of the present investigation.....	88
Figure 3-11 Results for the DISL approach failure profile with vertical and horizontal principal stresses for a) the top half of the profile reported by Diederichs (2007) obtained using <i>RS2</i> and b) <i>FLAC</i> results of the present investigation.....	89
Figure 3-12 Influence of $\psi$ on the failure profile in the CWFS approach a) $\psi = 0^\circ$ b) $\psi = 10^\circ$ c) $\psi = 20^\circ$ .....	91
Figure 3-13 Influence of $cp$ on the failure profile in the CWFS approach given a) $cp = 38$ MPa b) $cp = 64$ MPa.....	92
Figure 3-14 Influence of $\phi_i$ on the failure profile in the CWFS approach a) $\phi_i = 10^\circ$ b) $\phi_i = 20^\circ$ .....	93

Figure 3-15 Influence of $cr$ on the failure profile in the CWFS approach a) $cr = 7.25$ MPa b) $cr = 30$ MPa.....	94
Figure 3-16 Influence of $\phi m$ on the failure profile in the CWFS approach a) $\phi m = 45^\circ$ b) $\phi m = 51^\circ$ .....	94
Figure 3-17 Influence of $ecps$ and $e\phi ps$ on the failure profile in the CWFS approach a) ( $ecps = 0.001$ , $e\phi ps = 0.002$ ) b) ( $ecps = 0.002$ , $e\phi ps = 0.004$ ) c) ( $ecps = 0.003$ , $e\phi ps = 0.006$ ).....	96
Figure 3-18 Influence of $ecritps$ on the failure profile in the DISL method a) $ecritps = 0.004$ b) $ecritps = 0.005$ c) $ecritps = 0.01$ .....	97
Figure 3-19 Influence of $\psi$ on the failure profile in the DISL approach a) $\psi = 10^\circ$ b) $\psi = 20^\circ$ c) $\psi = 30^\circ$ .....	98
Figure 3-20 Influence of $sr = 0.1$ on the failure profile in the DISL approach.....	99
Figure 3-21 Influence of $mr$ on the failure profile in the DISL approach a) $mr = 8$ b) $mr = 9$ c) $mr = 10$ .....	99
Figure 3-22 Stress SA for CWFS models at different stress regimes for both constant $\sigma 3$ and constant $k$ compared to the $df$ equations proposed by Martin et al. (1999) and case scenarios observations reported by Diederichs et al. (2010).....	102
Figure 4-1 Results of <i>FLAC2D</i> CWFS models using the suggested strength parameters from Table 4-1 shows $\sigma 1$ plunge angle calibration to obtain the most adequate v-notch direction where the angles used are a) $21^\circ$ , b) $27^\circ$ , c) $35^\circ$ , d) $43^\circ$ , e) $51^\circ$ .....	111
Figure 4-2 Results for the simulation of the Qirehataer Diversion Tunnel using the CWFS in <i>FLAC2D</i> : a) the initial parameters suggested by the guidelines of Walton (2019) b) – e) the calibration procedure, f) the final parameters and results of the calibration with an acceptable match to the field observations. The comparative failure profile key, showing the reported v-notch formed in the field and the interpretation of the authors of other spalling cases as reported by Zhao et al. (2022). .....	112
Figure 5-1 The three IMASS constitutive models strength envelopes in the principal stress space and the mechanisms that control the transition from one envelope to the next with the corresponding $sloss$ values for each transitional state.....	116
Figure 5-2 Theoretical peak and post-peak failure envelopes in principal stress space for the input parameters suggested for the MBE at the URL applying the theory of the DISL method with the IMASS constitutive model.....	120

Figure 5-3 Single zone triaxial test model set up showing the loading velocity boundary in the z-direction and the confining stress application on the y- and x-directions. ....	121
Figure 5-4 Model setup for the MBE at the URL using the IMASS method, showing the excavation location and the mesh sizes. The stresses are rotated to achieve the symmetry, only one-quarter of the tunnel is simulated using roller boundaries for symmetry, and the model is one zone in the y-direction, making it a 2.5D model. ....	123
Figure 5-5 Simulated triaxial test results for LdB granite using the IMASS method a) in deviatoric stress vs strain space b) in principal stress space showing the peak and post-peak failure envelopes of the models compared to the theoretical envelopes. ....	127
Figure 5-6 Simulated triaxial test results for LdB granite using the IMASS method with 0 MPa confinement where a) deviatoric stress, <b><i>σ<sub>loss</sub></i></b> , and volumetric strain compared to axial strain, b) change in strength parameters <b><i>c</i></b> and <b><i>φ</i></b> with respect of axial strain increase. ....	128
Figure 5-7 Simulated triaxial test results for LdB granite using the IMASS method with 5 MPa confinement where a) deviatoric stress, <b><i>σ<sub>loss</sub></i></b> , and volumetric strain compared to axial strain, b) change in strength parameters <b><i>c</i></b> and <b><i>φ</i></b> with respect of axial strain increase. ....	129
Figure 5-8 Simulated triaxial test results for LdB granite using the IMASS method with 20 MPa confinement where a) deviatoric stress, <b><i>σ<sub>loss</sub></i></b> , and volumetric strain compared to axial strain b) change in strength parameters <b><i>c</i></b> and <b><i>φ</i></b> with respect of axial strain increase. ....	130
Figure 5-9 Results of the IMASS method using the preliminary strength parameters showing the failure profile (using zone state) and its characterization compared to the observed failure profile at the MBE rotated for simplicity of visualization compared to the field observation at the MBE by Martin (1997) (chainage unknown). ....	131
Figure 5-10 Influence of <b><i>σ<sub>UCSinput</sub></i></b> on the failure profile in the IMASS method a) <b><i>σ<sub>UCSinput</sub></i></b> = 118 MPa b) <b><i>σ<sub>UCSinput</sub></i></b> = 90 MPa ....	132
Figure 5-11 Influence of <b><i>m<sub>input</sub></i></b> on the failure profile in the IMASS method a) <b><i>m<sub>input</sub></i></b> = 2 b) <b><i>m<sub>input</sub></i></b> = 0.01 ....	133
Figure 5-12 Influence of <b><i>e<sub>multips</sub></i></b> on the failure profile in the IMASS method a) <b><i>e<sub>multips</sub></i></b> = 0.1 b) <b><i>e<sub>multips</sub></i></b> = 0.15 c) <b><i>e<sub>multips</sub></i></b> = 0.20. ....	134
Figure 5-13 Influence of <b><i>φ<sub>b</sub></i></b> on the failure profile in the IMASS method a) <b><i>φ<sub>b</sub></i></b> = 40° b) <b><i>φ<sub>b</sub></i></b> = 60° ....	135
Figure 5-14 Stress SA for the IMASS method at different hypothetical stress regimes compared to the <b><i>R<sub>f</sub></i></b> equation proposed Diederichs et al. (2010) and showing the maximum <b><i>σ<sub>max</sub>/σ<sub>ci</sub></i></b> threshold at which the model becomes unstable. ....	136

Figure 5-15 Numerical model setup for the QDT tunnel using the IMASS method in 2.5D, with the direction and magnitude of the principal stresses shown, the excavation size, the mesh parameters, and boundary conditions. ....139

Figure 5-16 Initial results and calibration of the QDT tunnel using the IMASS method with change in  $\sigma_{UCSinput}$  and  $m_{input}$  where a)  $\sigma_{UCSinput} = 45$  MPa and  $m_{input} = 1$  b)  $\sigma_{UCSinput} = 45$  MPa and  $m_{input} = 0.01$  c)  $\sigma_{UCSinput} = 40$  MPa and  $m_{input} = 0.01$  .....140

## ABSTRACT

Brittle failure occurs around underground excavations when the rock being excavated is competent and the induced stresses are high. Predicting and modelling this type of failure requires special care, as traditional methods of rock strength assessment do not apply directly to this type of ground. Therefore; alternative methods have been proposed to adequately predict the behaviour of brittle rock around excavations. A literature review of current methods was performed where 21 different methods were identified and detailed. These methods can be subdivided into four general categories: empirical methods, continuum numerical modelling methods, discontinuum numerical modelling methods, and hybrid continuum-discrete numerical modelling methods. The list proposed is not exhaustive, and no single method can be suggested to be the best, instead, the user has to determine which method is more suitable for their purpose and experience. Two of the most prominent continuum numerical modelling methods were further investigated, these were the Cohesion Weakening Friction Strengthening (CWFS) method and the Damage Initiation Spalling Limit (DISL) method. Both methods were applied to a common case study, the Mine-by Experiment (MBE) at the Underground Research Laboratory. Then all the input parameters for each method were investigated to determine the effect of each parameter on the simulation results. Alternative stress scenarios were investigated using the rock at the MBE to determine each method's capabilities of modelling brittle failure in different ground stress conditions. From this in-depth investigation of the CWFS and DISL methods, it was found that the CWFS method is a more robust method that can be implemented by rock mechanics practitioners and is ideal for parametric studies and construction monitoring. On the other hand, the DISL method produces hard-to-interpret results which make the method's interpretation subjective and viable for rock mechanics engineers who are experts in numerical modelling. Once noted that the CWFS is a more robust method was applied to a different case study, the Qirehataer Diversion Tunnel (QDT) in Western China. This application to a new case study increased the understanding of the CWFS method and demonstrated that it can be feasibly used to perform a parametric calibration to match field observations. The last stage of this dissertation was the development of a novel method to model brittle failure around underground excavations. The method developed consisted of using the IMASS constitutive model in *FLAC3D* to apply the theory of the DISL and CWFS methods. This new method was developed using the MBE as a case study. The results showed that, by modifying the IMASS input parameters, failure around underground excavations can be predicted. To aid future users of the method a preliminary set of guidelines was proposed. Then, using these guidelines, the IMASS method for brittle rock modelling was applied to the QDT. The results matched the field observations from this study validating both the IMASS method and the proposed guidelines. The investigation of the CWFS and DISL methods expanded on the understanding of both methods from the systematic sensitivity study. This research can be used by future users of the methods as guidance for parameter selection. The development of the IMASS methods provides another tool that rock mechanics practitioners can use for brittle rock failure around underground excavations which has a simpler parameter selection process than other continuum based methods.

Keywords: Brittle rock failure, underground excavations, numerical modelling, DISL, CWFS, IMASS.

## LIST OF ABBREVIATIONS AND SYMBOLS USED

$a$	Tunnel Radius
$A_t, B_t, A_c, B_c$	Mazar's Damage Parameters
$B, D$	Perras and Diederichs (2016) fitting parameters
$c$	Cohesion
$c_p$	Peak Cohesion
$c_{pb}$	Block Peak Cohesion
$c_{pbb}$	Block Boundary Peak Cohesion
$c_r$	Residual Cohesion
$c_{rb}$	Block Residual Cohesion
$c_{rbb}$	Block Boundary Residual Cohesion
CWFS	Cohesion-Weakening Friction-Strengthening
D&B	Drill and Blast
DEM	Distinct-element Method
$d_f$	Depth of failure
DGR	Deep Geological Repositories
DISL	Damage Initiation Spalling Limit
$E$	Young's Modulus of Elasticity
$E_b$	Block Young's Modulus
$\bar{E}_c$	<i>PFC</i> bond's Young's modulus
$e_c^{ps}$	Cohesion Critical Strain
$e_{crit}^{ps}$	Critical Plastic Strain for DISL method
$e^{ps}$	Plastic Shear Strain
$e_\phi^{ps}$	Friction Angle Critical Strain
EDZ	Excavation Damage Zone
EdZ/EIZ	Stress-induced Excavation Disturbed/Influence Zone
EDZ <sub>CI</sub>	Construction-induced Damage Zone
EDZ <sub>i</sub>	Inner Excavation Damage Zone
EDZ <sub>o</sub>	Outer Excavation Damage Zone
EDZ <sub>SI</sub>	Stress-induced Damage Zone
$F$	<i>FRACOD</i> Normalized Fracture Criterion
FDEM	Finite-Discrete Element Method
$\phi$	Friction Angle
$\phi_b$	Basic Friction Angle
$\phi_i$	Initial/Peak Friction Angle
$\phi_m$	Mobilized/Residual Friction Angle
$\phi_{pb}$	Block Peak Friction Angle
$\phi_{pbb}$	Block Boundary Peak Friction Angle
$\phi_{rb}$	Block Residual Friction Angle
$\phi_{rbb}$	Block Boundary Residual Friction Angle



$G_I$	Tensile Mode Fracture Energy
$G_{II}$	Shear Mode Fracture Energy
$GSI$	Geological Strength Index
HDZ	Highly Damage Zone
HLW	High-Level Waste
IMASS	Itasca Model for Advanced Strain Softening
$k$	In situ Stress Ratio
$\bar{k}_n$	<i>PFC</i> bond's normal stiffness
$\bar{k}_s$	<i>PFC</i> bond's shear stiffness
$k_n$	Normal Stiffness
$k_s$	Shear Stiffness
LdB	Lac du Bonnet
$\bar{\lambda}$	<i>PFC</i> bond radii multiplier
MBE	Mine-by Experiment
$m_i, m_b, s, a$	Hoek-Brown Failure Envelope Parameter
$m_{iinput}$	IMASS Input Hoek-Brown Parameter
$m_p, s_p, a_p$	Peak Hoek-Brown Failure Envelope Parameters
$m_r, s_r, a_r$	Residual Hoek-Brown Failure Envelope Parameters
$\nu$	Poisson's Ratio
$\nu_b$	Block Poisson's Ratio
$P_i$	Internal Pressure
$P_o$	Initial Internal Pressure
$\psi$	Dilation Angle
$r$	Extent of the region of interest
$R_f$	Depth of failure measured from the center of the tunnel
RMR	Rock Mass Rating
SA	Sensitivity Analysis
$sloss$	IMASS Softening Monitoring Parameter
$\sigma_1$	Major Principal Stress
$\sigma_2$	Intermediate Principal Stress
$\sigma_3$	Minor Principal Stress
$\bar{\sigma}_c$	<i>PFC</i> bond's tensile strength
$\sigma_{cd}$	Crack Damage Stress
$\sigma_{ci} / \sigma_{CI}$	Crack Initiation Stress
$\sigma_{max}$	Maximum Tangential Stress Calculated Elastically
$\sigma_t$	Tensile Strength of intact rock
$\sigma_{tpb}$	Block Peak Tensile Strength
$\sigma_{tpbb}$	Block Boundary Peak Tensile Strength
$\sigma_{trb}$	Block Residual Tensile Strength
$\sigma_{trbb}$	Block Boundary Residual Tensile Strength

$\sigma_{UCS_{input}}$	IMASS Input Unconfined Compressive Strength
$\sigma_{UCS}$	Uniaxial Compressive Strength
$\bar{\tau}_c$	<i>PFC</i> bond's shear strength
$\theta$	Fracture Direction
URL	Underground Research Lab
$\mu$	Grain Friction Coefficient
VTM	Voronoi Tessellated Model
$VSI_{max}$	Maximum Volumetric Strain Increment
$VSI$	Volumetric Strain Increment

## **ACKNOWLEDGEMENTS**

I would like to start by thanking my co-supervisors Dr. Andrew Corkum and Dr. Navid Bahrani who guided me through this research for the last two years, and whose technical knowledge and enthusiasm for this topic made this thesis possible. Our recurring meetings and discussions made the ideas presented here made the research as fruitful as it is. Not only did they help me complete this research but gave me a more complete perspective of the field of rock mechanics that will transcend my degree and help me in my professional life

Another person I wish to acknowledge is Dr. Diego Mas Ivars, from SKB, who not only provided the funding for the thesis but gave insight and guided the findings. Thanks to his practical and big-picture perspective of the topic, the results in this dissertation are as practical to real-world application as they are. Dr. Mas Ivars helped me understand the purpose and impact my research can have on the world.

This research could not have been possible without the financial aid of the Killiam Laureates Predoctoral Scholarship and the Itasca Education Program (IEP) from the Itasca Consulting Group.

My deep appreciation goes as well to my colleagues from the rock mechanics group at Dalhousie University: Max Trzop, Ryan Ziebarth, Fatimah Amiri Ramsheh, and Farzaneh Hamed Azad. Their constant help and collaboration helped me complete this thesis and improve the quality of my work.

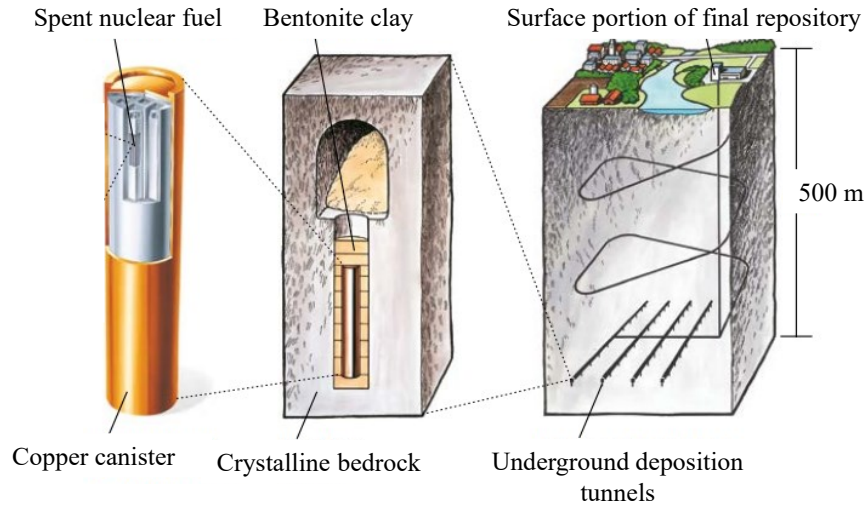
I want to also thank my family who encouraged me and supported me even with thousands of kilometres between us. My father Maximino and my mother Imelda were always there for me as motivators and support.

Lastly, my work would not have been possible without the love and support of my partner Hannah. She was always there as my main support system and her sacrifice, care, understanding, and patience motivated me and helped me give the best of me throughout this degree.

# **CHAPTER 1 - INTRODUCTION**

## **1.1 BACKGROUND**

As energy production moves away from fossil fuels, one of the most compelling alternatives is nuclear power (Barattta, 2009). Nuclear waste is a direct byproduct of energy creation by nuclear fission. This type of nuclear waste is termed High-Level Waste (HLW). It emits Alpha and Beta particles and Gamma rays, the effects of each are varied, but all are harmful to human life if not contained (World Nuclear Association, 2022). These radioactive particles can also significantly affect the environment as all organic matter can be affected by these types of radiation. This HLW is measured to have a radioactive half-life of up to 1 million years (Ahn and Apted, 2010). As such, there is a need to deal with this radioactivity for a long time. Many different methods have been proposed to deal with long-term HLW disposal, from sub-seabed disposal to disposal into the ice sheets of the poles (Ojovan et al. 2019). However, one of the most prominent ideas is using Deep Geological Repositories (DGR) for long-term disposal of HLW. This type of disposal consists of burying HLW in engineered canisters in deep subterranean tunnels (Ahn and Apted, 2010). The deposition of this HLW is multilayered, the first being a copper canister deposited in a tunnel which is filled with bentonite clay surrounded by the competent host rock (Elfving, et al, 2013). The burial of these canisters is often planned to occur at great depths (200 to 1000 m). Figure 1-1 shows the schematic of a multilayer DGR as proposed by the Swedish Nuclear Fuel and Waste Management Co. (SKB). These facilities are designed to last for geological time scales to contain the radionuclides generated by the HLW.



**Figure 1-1 Multilayered design of the DGR proposed for the Forsmark site by SKB (modified after Elfving, et al, 2013)**

As permanent and high-importance structures, DGRs require special care when designing them. Plenty of factors need to be considered before the construction of one can even start. Factors crucial for the design of a DGR include geotechnical, hydrogeological, and geochemical considerations (Ahn and Apted, 2010). The hydrological environment has to be designed to minimize the potential of radionuclide transport into the groundwater. The main goal is to design and excavate within a low porosity/low fractured rock so that the fluid transport is minimized or, at the very least, well understood. On the geochemical side, the DGR is best designed when there are little to no chemical interactions between the host rock and the radiation. The geotechnical considerations include the rock strength, time-dependent behaviour, seismicity, stress regime, etc. (Ahn and Apted, 2010). The geotechnical design criteria for DGR are of interest to this dissertation.

The effect that an excavation has on the host rock is important for the design of a DGR. When excavating in rock, the stresses are altered, creating localized zones of high and low stress. These disturbances affect the rock by generating fractures and, in some cases, resulting in failure around an excavation. This disturbance zone around an excavation is called the Excavation Damage Zone (EDZ). It has been of great interest since the idea of storing radioactive waste underground (Kelsall et al. 1984). One of the most accepted definitions for EDZ in crystalline rock is given by Tsang et al. (2005) as: "Region of irreversible [rock] deformation with fracture propagation and/or development of new fractures". These

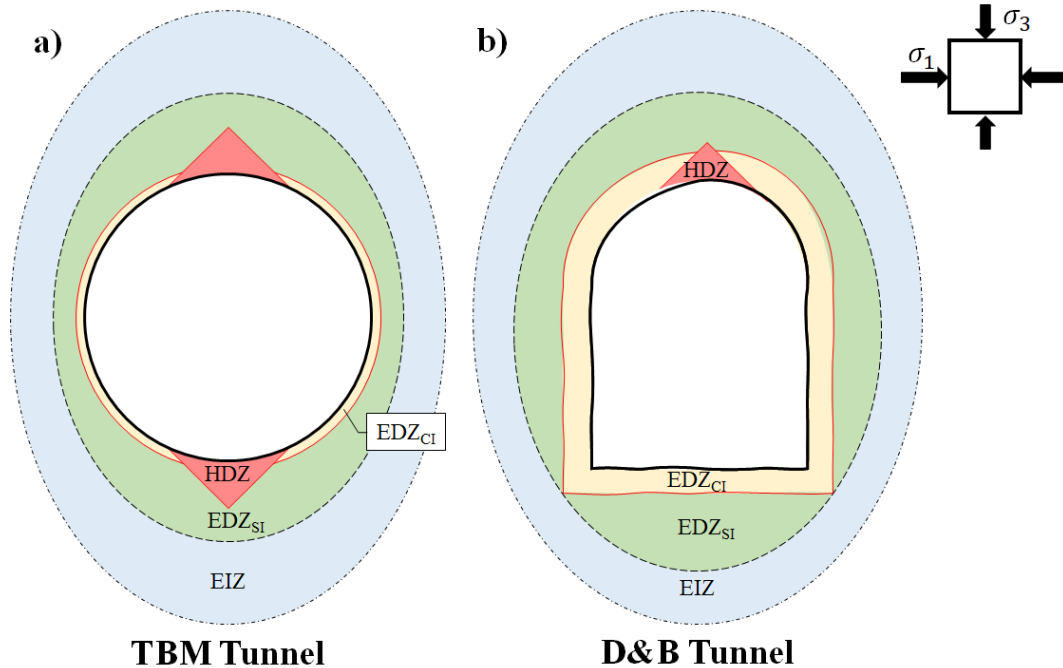
irreversible changes in the rock mass induce significant changes in flow and transport properties. It can change fluid transport of multiple orders of magnitude (Tsang et al. 2005). This definition varies depending on the rock mass where the DGR is planned. Yet, for this study, the definition of interest is that of crystalline hard rock. Some of the main issues from the EDZ in crystalline rock noted by Tsang et al. (2005) include the potential for fast flow of radionuclides due to the change in the hydrological properties of the rock. The inflow of water into the excavation opening can also negatively affect the performance of the DGR as water flows from the rock mass into the excavation due to the decrease in pressure (Siren et al. 2015). There are multiple ways the EDZ can affect the permeability of the host rock; it can fracture the massive rock generating a flow path for water, or it can loosen the crystal structure or increase the porosity of the rock due to reduced confining stresses (Kelsall et al. 1984). When a large EDZ develops, the support design can also be a challenge for engineers (Tsang et al. 2005).

Three main processes contribute to the formation of the EDZ. The first is the stress redistribution due to the excavation (Kelsall et al., 1984; Siren et al., 2015; Perras and Diederichs, 2016). This area is characterized by the irreversible property changes on the rock mass caused by the redistribution of stresses due to the removal of rock as the excavation advances (Siren et al. 2015). The next process that contributes to the formation of the EDZ is the construction method (Kelsall et al., 1984; Siren et al., 2015). The changes can result from the selected excavation method, and they can be almost entirely mitigated if a mechanical construction method such as a Tunnel-Boring Machine (TBM) is selected (Siren et al. 2015). The third mechanism that affects the creation of EDZ is the weathering of the rock mass. As fluid is transported through the new disturbed zone, this generates a weathering effect that increases the length and effects of the EDZ (Kelsall et al. 1984). All these processes differ depending on the rock type that the excavation is taking place in. Weathering or blasting do not have the same effect on a crystalline rock as they do on a clay (Tsang et al. 2005). In this dissertation, the primary mechanism for EDZ formation to be investigated is the stress redistribution in hard brittle rock.

The EDZ is the general name for the mechanism of failure and deformation around an excavation in brittle rock, yet it can be subdivided into different zones, each with its own characteristics and mechanism (Siren et al. 2015). The three main zones proposed by Siren

et al. (2015) are the stress-induced Excavation Damage Zone ( $EDZ_{SI}$ ), the construction-induced Excavation Damage Zone ( $EDZ_{CI}$ ), and the stress-induced Excavation Disturbed/Influence Zone (EdZ or EIZ) (Siren et al., 2015; Perras and Diederichs, 2016). The  $EDZ_{SI}$  is the most significant one and extends several meters from the excavation boundary. The main characteristic of this zone is that it has gone through irreversible/plastic deformation, often associated with the initiation of new fractures and the displacement of existing ones (Siren et al., 2015). This zone can be identified in the field by micro-seismic events near the excavation boundary (Martin, 1997). The  $EDZ_{CI}$  is caused by the selected construction method, it can be diminished significantly if mechanical excavation methods are used rather than drill and blast (D&B). When using D&B as a construction method, the properties of the rock are affected by the creation of fractures from the release of energy and gas migration. As such, the hydraulic properties are affected, increasing the hydraulic conductivity near the excavation (Siren et al., 2015). The EIZ is the zone where the changes are reversible/elastic. The deformation of the rock mass is not enough to cause irreversible damage; therefore, the rock does not experience changes in its hydraulic properties (Siren et al., 2015).

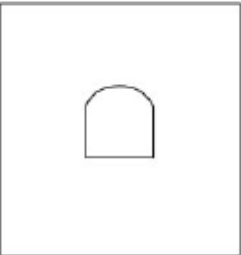
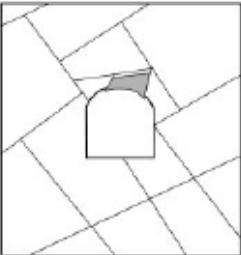
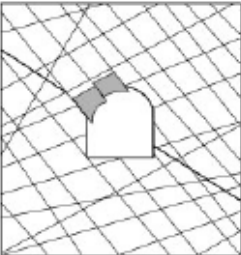

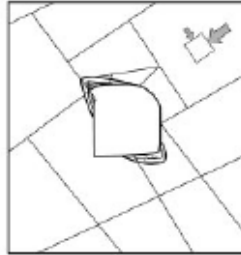
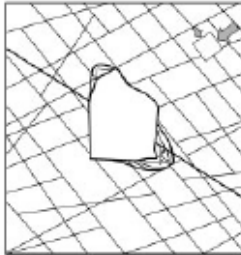

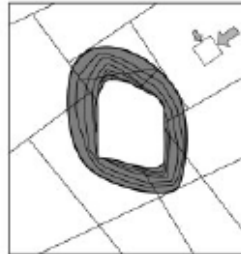
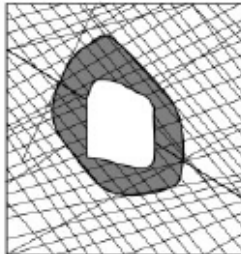
For practical purposes, the three previously mentioned zones are enough to describe the EDZ in brittle rock. Some suggest further dividing the  $EDZ_{SI}$  into three distinct zones (Perras and Diederichs, 2016). The first is the Highly Damaged Zone (HDZ), characterized by the interconnected macro-fractures that cause the unravelling of the rock near the excavation boundary (Perras and Diederichs, 2016). This HDZ is called the v-notch failure or spalling zone, where a complete detachment of the rock occurs (Martin, 1997). Further away from the excavation is the inner EDZ ( $EDZ_i$ ), characterized by connected damage in the form of fractures without unravelling of the rock mass. Lastly, before the EIZ comes the outer EDZ ( $EDZ_o$ ), where there is irreversible/plastic damage in the rock but the fractures are not interconnected (Perras and Diederichs, 2016). Figure 1-2 shows the general arrangement of these EDZ subdivisions for underground excavation with different construction methods. Each of these zones comes with a change in the hydraulic properties of the rock, which affects the transport of radionuclides into the rock mass (Bossart, 2002).



**Figure 1-2 Overview of EDZ nomenclature with a given stress regime for a) a tunnel excavated using the tunnel-boring machine method and b) a tunnel excavated using drill and blast method (after Siren et al. 2015).**

As one major concern for the design of DGR, the modelling, prediction, and understanding of the EDZ in brittle rock have been a subject of interest in the rock mechanics field for a long time. The interest in understanding EDZ started in the 60s when Hoek (1965) investigated the propagation of cracks and failure of brittle rock. When designing an underground excavation, one of the first steps is to determine the possible modes of failure that can be encountered (Kaiser et al., 2000). One of the most common ways of determining the type of failure expected is determining the rock mass quality, with either the Rock Mass Rating (RMR) or the Geological Strength Index (GSI), and the in situ stress conditions. These two parameters directly relate to the possible failure. The chart shown in Figure 1-3 shows the possible failure scenarios. DGRs are often planned to be excavated in non-jointed competent rock. They are also designed at great depth to create a geological barrier from the radionuclides to the surface and water tables (Ahn and Apted, 2010). Based on these design criteria, brittle rock failure is the most common failure expected in hard rock crystalline DGR.



	<b>Massive</b> RMR >75	<b>Moderately Fractured</b> 75>RMR>50	<b>Highly Fractured</b> 50>RMR
<b>Low in situ stress</b> $\sigma_1/\sigma_{UCS}<0.15$	 <p>Linear elastic response</p>	 <p>Falling or sliding of block and wedges</p>	 <p>Unravelling of block from the excavation surface</p>
<b>Intermediate in situ stress</b> $0.15<\sigma_1/\sigma_{UCS}<0.40$	 <p>Brittle failure adjacent to excavation boundary</p>	 <p>Localized brittle failure of intact rock and movement of blocks</p>	 <p>Localized brittle failure of intact rock and unravelling along discontinuities</p>
<b>High in situ stress</b> $\sigma_1/\sigma_{UCS}>0.40$	 <p>Brittle failure around the excavation</p>	 <p>Brittle failure of intact rock around the excavation and movement of blocks</p>	 <p>Squeezing and swelling rock. Elastic/plastic continuum</p>

**Figure 1-3 Tunnels modes of instability and possible types of failure as a function of the ratio between in situ stresses and unconfined compressive strength, and RMR. In red are the possible occurrences of spalling failure in brittle rock investigated in this study. (modified after Kaiser et al. 2000)**

It has been noted that principles that apply to the strength of other rock conditions with intermediate to low RMR or GSI do not apply to hard brittle rock (Martin, 1997). If traditional strength criteria, such as the Mohr-Coulomb strength envelope or the Hoek-Brown strength envelope are used, the strength of the rock near the excavation boundary where

confinement is low is overestimated (Kaiser et al., 2000). Therefore, different tools must be employed to better understand the EDZ behaviour in brittle rock masses. Diederichs (2007) proposed that for brittle rock, with high strength ratio ( $\sigma_{UCS}/\sigma_t$ ), at high GSI ratings, the normal GSI/Hoek-Brown approach is no longer valid to estimate the rock mass stress, and different techniques need to be employed to simulate these behaviours. Table 1-1 shows the criteria for when the GSI approach is valid and when other methods should be employed, as suggested by Diederichs (2007). Martin (1997) demonstrated this using the Mine-by Experiment (MBE) at the Underground Research Laboratory (URL) in Canada. Given the tunnel conditions and the rock's strength, Lac du Bonnet (LdB) granite, the conventional Hoek-Brown or Mohr-Coulomb strength envelopes predicted no failure. However, spalling failure was encountered (Martin et al., 1997). These observations have prompted the constant development of methods to simulate and predict brittle rock failure in underground excavations.

**Table 1-1 Selection of either the Hoek-Brown constitutive model or alternative brittle rock failure method given the GSI of the rock mass and the rock strength ratio ( $\sigma_{UCS}/\sigma_t$ ) (modified after Diederichs, 2007)**

Strength Ratio	GSI < 55	GSI = 55-65	GSI = 65-80	GSI > 80
$\sigma_{UCS}/\sigma_t < 9$	GSI	GSI	GSI	GSI
$\sigma_{UCS}/\sigma_t = 9-15$	GSI	GSI	GSI	Alternative/GSI
$\sigma_{UCS}/\sigma_t 15-20$	GSI	GSI/Alternative	Alternative/GSI	Alternative
$\sigma_{UCS}/\sigma_t > 20$	GSI	GSI/Alternative	Alternative	Alternative

A wide range of tools are used for brittle rock modelling around underground excavations. Some authors (Hamdi, 2015; Sanipour et al., 2022) have compiled lists of such methods and compared them. In general, they can be classified into four different groups. The first and simplest are the analytical and empirical methods. They are based on first principles and field observation to identify correlations between the stresses, the rock strength, and the potential behaviour of the EDZ. Due to their limitations, they serve as a first-level investigation for the design of DGR in brittle rock. The next category is the continuum numerical methods. They involve using continuum numerical software to attempt to replicate the behaviour and failure of brittle rock. While more complex than analytical and empirical methods, they are still an approximation of the process, as a continuum cannot truly replicate a fracture process

such as the failure of brittle rock. The third category is discontinuum numerical methods. These methods use discontinuum numerical software to recreate the failure of brittle rock. They are one level of complexity above continuum numerical methods as they allow for the simulation of the fracture process explicitly. The unravelling of the rock mass after failure is explicitly simulated using discontinuum tools. These methods are involved and computationally expensive. The final category is the hybrid continuum-discontinuum numerical method. As the name suggests, they are a combination of the two previous methods. They start as a continuum that is allowed to fracture following the principles of fracture mechanics. As a method to model brittle rock failure around excavations, they come the closest to explicitly simulating the mechanism presented in reality. However, they are hard to use and apply for the design and prediction of EDZ. The hybrid methods often involve the use of parameters that are not readily obtainable from laboratory testing, such as fracture energies. This thesis investigates the most prominent tools in each of these categories. It compiles and compares them according to the quality of their results and viability for the design of DGR in brittle rock.

## **1.2 OBJECTIVES AND METHODOLOGY**

The number of methods to model EDZ in hard brittle rock is extensive and continuously growing. Every method varies in complexity, implementation, and level of expertise of the user required for its successful application. The methods' capability to represent different characteristics of the EDZ is also different for each. Therefore, the use of a method must be carefully selected depending on the specificity, accuracy, and simplicity required. If an engineer requires a first-level investigation of possible brittle failure on a tunnel, they should select the method that can effectively produce this first-degree approximation. There are a few extensive compilations in the literature of all the methods that can effectively be used (Sanipour et al., 2022).

There is a benefit to creating a new list of methods that can then be compared on their advantages and disadvantages so that a rock mechanics engineer can decide the method best suited for their task at hand. This thesis was set to do that, generate a literature review of existing methods with varying complexity and compare each with one another. After reviewing the methods, a comparative table was made to summarize the advantages and

disadvantages of each. After the list was created, some selected methods were used and updated to create guidance on the use for future users. The two methods investigated were the Damage Initiation Spalling Limit (DISL) proposed by Diederichs (2007) and the Cohesion Weakening Frictional Strengthening (CWFS) method proposed by Hajiabdolmajid, et al. (2002). Both methods were used to replicate the field observations at the MBE as detailed by Martin, et al., (1997). This application was done to increase the understanding of these methods and assess their effectiveness and robustness. Both methods were subjected to sensitivity analysis to increase the understanding of strength parameter selection for the design of underground excavation in brittle rock. The CWFS method was applied to a case study of a diversion tunnel in western China where spalling was observed (Zhao, et al, 2017, Zhao, et al., 2022) to replicate the field observations. The last objective for this dissertation is the creation of a novel method for modelling brittle rock failure around underground excavations. This method uses the Itasca Constitutive Model for Advanced Strain Softening (IMASS) and the theory behind DISL and CWFS to create a new way of achieving EDZ modelling with continuum numerical models.

### **1.3 DOCUMENT OVERVIEW**

The document is divided into 5 different chapters:

Chapter 1: This chapter is the introduction to the topic, the objectives of the thesis, the methodology and the document overview

Chapter 2: In this section a literature review of current methods is of EDZ modelling conducted and a comparative table of such methods is prepared. This section was submitted as a separate report to SKB. This chapter aims to have an extensive list of methods for brittle rock failure modelling for SKB to decide on suitable modelling techniques.

Chapter 3: This chapter details the investigation of the CWFS and DISL method using *FLAC*. It is a journal paper submitted to the Computers and Geotechnics titled: "A Sensitivity Study and Comparative Robustness Evaluation of the CWFS and DISL Methods of Brittle Failure Continuum Modelling Around Underground Excavations" .

Chapter 4: This chapters details the application of the CWFS method to a hydropower diversion tunnel in Western China. This application was submitted and presented at the Itasca

Symposium 2024 and was titled: "Application of the CWFS method in FLAC2D to model brittle failure around the Qirehataer Diversion Tunnel".

Chapter 5: This sections details the implementation of a new method for EDZ modelling using the *IMASS* constitutive model by Itasca in *FLAC3D*. It details the motivation and background behind the method and its application to two case studies and several potential scenarios.

Chapter 6: The final chapter is the conclusion of the thesis, which summarizes the findings of all the investigations and gives suggestions for potential future work on the topic.

## **CHAPTER 2 - LITERATURE REVIEW**

Predicting and simulating the behaviour of brittle rock around excavations has been of interest to researchers since 1960 (Hoek, 1965). As such, there have been many proposed methods to define such behaviours, and methods are constantly being developed. All the methods can be categorized into one of four categories: empirical methods, continuum numerical modelling methods, discontinuum numerical modelling methods and hybrid Finite-Discrete numerical modelling methods. Analytical methods to estimate fracture propagation and depth of spalling in brittle rock near excavation boundary have also been proposed (Germanovich and Dyskin, 2000). However, due to their complexity and their limitations for their application to underground excavations, they will not be explored in this dissertation. Each subcategory has its advantages and disadvantages. Proposing a single superior method to predict and understand EDZ is not beneficial, as there is not a single best method proposed. Instead, each method has to be chosen based on the intended goal of the rock engineer. With this goal in mind, in this section, some of the most prominent methods are discussed so that the reader can get an idea of which suits their criteria the best. This list is also not comprehensive and can be appended in future works.

### **2.1 EMPIRICAL METHODS**

The simplest way to estimate the failure of rock around underground excavations and predict the extent of EDZ is by using empirical methods. This empirical method generally consists of a regression analysis according to field observations in similar scenarios. As such, their use is limited, yet these empirical methods serve as the first stage in determining the possible conditions that can be encountered in the field. Other more complex modelling methods also benefit from empirical predictions as estimators of the adequacy of the model. They serve as a first-order estimator to demonstrate the validity of other methods. Some of the main disadvantages of these empirical methods are that they work under a wide range of assumptions, such as the strength of the rock mass, the geometry of the excavation, the distribution of stresses, and the mechanisms that cause spalling. These empirical methods are also more adept at describing the extent of failure rather than providing a complete description of the EDZ.

### 2.1.1 Stress-induced failure prediction

The first approximation to predict the EDZ in brittle ground is to determine if there is a stress-induced failure for underground excavations. Kaiser et al. (2000) suggest that the first step when designing an underground excavation is to establish the possible types of failure that might be present in the field. The type of failure depends on the rock mass quality and the stress state. Kaiser et al. (2000) proposed a table that correlates the RMR (Rock Mass Rating) with the mining-induced stresses to find the instability mode. The table, modified from Kaiser et al. (2000), is shown in Figure 1-2 (Section 1.1). This table proposes that brittle failure occurs once the mining-induced stresses exceed  $0.4 \times \sigma_{UCS}$  and that brittle failure is more characteristic of highly competent brittle rock with  $RMR > 50$ .

While this table and method are very limited in use for detailed design of tunnels, they are an adequate first principles investigation for the field conditions. With the outcome of using this tool, an adequate investigation method can be selected according to the conditions suggested in the table. The circumstances shown in the table almost certainly need to be present for brittle rock failure in an underground excavation.

### 2.1.2 Depth of failure equation

One of the first empirical methods to determine the extent of failure was proposed by Martin et al. (1999) as an equation that relates the depth of failure around a tunnel to the  $\sigma_{UCS}$  of the intact rock mass and the in situ stresses in the field. The equation proposed by them is:

$$\frac{R_f}{a} = 0.49 (\pm 0.1) + 1.25 \frac{\sigma_{max}}{\sigma_{UCS}} \quad (2-1)$$

where  $R_f$  is the depth of failure measured from the center of the tunnel to the tip of the formed notch,  $a$  is the radius of the excavation, and  $\sigma_{max}$  is the maximum induced tangential elastic stress around a circular opening given by (Kirsh, 1898):

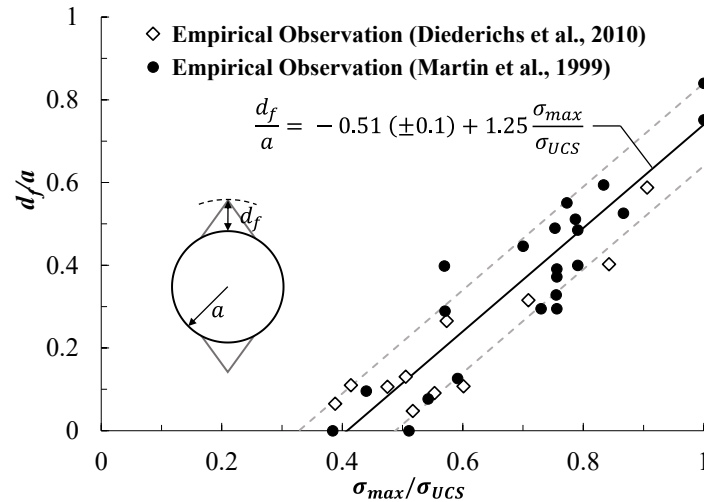
$$\sigma_{max} = 3\sigma_1 - \sigma_3 \quad (2-2)$$

Alternatively, the equation can be expressed as:

$$\frac{d_f}{a} = -0.51 (\pm 0.1) + 1.25 \frac{\sigma_{max}}{\sigma_{UCS}} \quad (2-3)$$

where  $d_f$  is the depth of failure measured from the original excavation boundary to the tip of the failure profile. This equation was obtained from a linear regression of multiple field

observations of tunnels in brittle rock that had failed (Martin et al. 1999). The field observations that were used as a basis for the regression are shown in Figure 2-1.



**Figure 2-1 Empirical observations of the depth of failure by Martin et al. (1999) and Diederichs et al. (2010) compared to the empirical prediction equation of  $d_f$  by Martin, et al. (1999)**

Figure 2-1 was first proposed by Martin, et al. (1999) to demonstrate the regression used to obtain Equation (2-3); it was later appended by Diederichs et al. (2010) to add more field observations. The tunnels used to obtain the plot correspond to multiple stress states, tunnel geometries, and geologies, all being in competent rock with little to no discontinuities where the leading cause of failure was stress. As such, the observation are a wide range of data that gives robustness to the regression and can generally be applied for forward prediction for brittle rock failure around underground excavations. According to these observations, failure starts occurring around a tunnel when the stresses are  $\approx 0.4 - 0.5 \sigma_{UCS}$ . This result aligns with the crack initiation threshold observed in core sample UCS testing by Martin and Chandler (1994). Given these observations, Diederichs et al. (2010) modified Equation (2-1) to be dependent on the crack initiation strength rather than the ultimate strength of the rock. The resulting equation is (Diederich et al., 2010):

$$\frac{R_f}{a} = 0.5 \left( \frac{\sigma_{max}}{\sigma_{ci}} + 1 \right) \quad (2-4)$$



where  $\sigma_{ci}$  is the crack initiation stress. What the modification suggests is that failure begins to occur once  $\sigma_{max} > \sigma_{ci}$ , which aligns with field observations (Martin et al., 1999). All the equations presented above also demonstrate that using the Hoek-Brown failure criteria for massive brittle rock highly overestimates its strength, yielding an inadequate prediction of the response of an underground excavation under these conditions.

While it is helpful to estimate the depth of failure around an excavation, this method is very limited to many other applications. The equation only yields the depth of failure. It does not indicate the shape of failure or the volume of rock that might fail. It also fails to describe any of the other zones of the excavation damage. The full EDZ profile cannot be derived using this equation.

### 2.1.3 Empirical equations of EDZ prediction

Equation (2-1), suggested by Martin et al. (1999), only describes the extent of the depth of failure (HDZ). Others have attempted to derive equations to demonstrate the EDZ and its different subdivisions better. Perras and Diederichs (2016) used numerical models and the observations by Diederichs et al. (2010) to give some guidance on the extent of the different EDZ subregions (HDZ, EDZ<sub>i</sub>, EDZ<sub>o</sub>). The equation is dependent on the stress ratio encountered and the rock type. The equation has the general form (Perras and Diederichs, 2016):

$$\frac{r}{a} = 1 + B \left( \frac{\sigma_{max}}{\sigma_{ci}} - 1 \right)^D \quad (2-5)$$

where  $r$  is the extent of the region of interest (HDZ, EDZ<sub>i</sub>, EDZ<sub>o</sub>) measured from the centre of the excavation, and  $B$  and  $D$  are rock type and stress-dependent constants. The  $B$  and  $D$  constants are selected given the following table according to the numerical investigations by Perras and Diederichs (2016):

**Table 2-1 EDZ characterization constant multipliers and correlation coefficients (modified after Perras and Diederichs, 2016)**

Rock Type	$K_{Hh}^*$	Zone	B	D	R <sup>2</sup>
Granite	1.5	EDZ <sub>o</sub>	0.62	0.58	0.81
		EDZ <sub>i</sub>	0.41	0.53	0.78
		HDZ	0.09	0.62	0.48
Granite	2	EDZ <sub>o</sub>	0.58	0.65	0.81
		EDZ <sub>i</sub>	0.36	0.62	0.64
		HDZ	0.11	0.85	0.45
Limestone	1.5	EDZ <sub>o</sub>	0.66	0.63	0.95
		EDZ <sub>i</sub>	0.43	0.58	0.93
		HDZ	0.18	0.34	0.42
Limestone	2	EDZ <sub>o</sub>	0.58	0.58	0.89
		EDZ <sub>i</sub>	0.36	0.49	0.75
		HDZ	0.12	0.33	0.12
Mudstone	1.5	EDZ <sub>o</sub>	0.71	0.59	0.93
		EDZ <sub>i</sub>	0.49	0.55	0.91
		HDZ	0.2	0.52	0.67
Mudstone	2	EDZ <sub>o</sub>	0.66	0.59	0.97
		EDZ <sub>i</sub>	0.39	0.59	0.93
		HDZ	0.15	0.68	0.75
All		EDZ <sub>o</sub>	0.61	0.59	0.87
		EDZ <sub>i</sub>	0.37	0.50	0.69
		HDZ	0.15	0.65	0.45

These guidelines are the result of regressions done on numerical modelling investigations (Detailed in Section 2.2.3.3). The regression analysis was done by conducting a numerical simulation using the rock's mean, maximum, and minimum strength obtained via laboratory testing (Perras and Diederichs, 2016). Thanks to its parametrization with  $\sigma_{max}/\sigma_{ci}$ , these predictions apply to a wide range of depths and in situ stresses. In general, the HDZ has a lower R<sup>2</sup> than the EDZ<sub>o</sub>, which suggests a lower degree of confidence for the HDZ. The authors suggest using this guideline as an initial estimation to determine the possible extent of EDZ and adjust the radius of the excavation accordingly.

The equation suggested for EDZ extent calculation is an adequate first step for EDZ approximation. This method is relatively simple, and no numerical models are needed to start the design. One of the shortcomings of this method is that it came from a theoretical and numerical investigation of possible scenarios and was, to a degree, corroborated by some empirical observations. However, the investigation does not have a physical experiment

counterpart to corroborate the suggestions. It also only provides the extent and not the shape of the zones. A complete profile cannot be developed using this method. Rock mechanics practitioners should use this method with caution as an initial investigation of possible field conditions rather than as a final approximation for design.

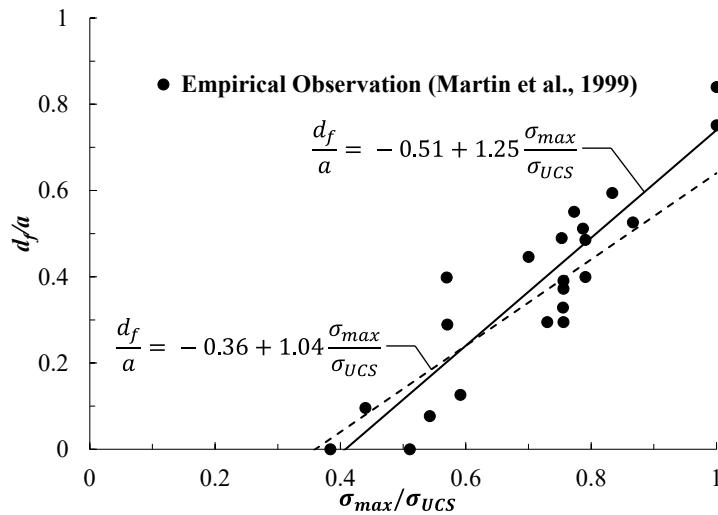
## **2.2 CONTINUUM NUMERICAL METHODS**

The next step towards better approximating tunnel EDZ behaviour is by using continuum numerical modelling tools. These methods represent the brittle rock surrounding an excavation using a continuum domain. To represent a rock mass (which is inherently discontinuous), they approximate its strength to an equivalent continuum according to the properties of intact rock and the scale effects of the system in question. This assumption is adequate in brittle rock, as one of its main characteristics is that the rock is massive and continuous. The discrepancy comes when continuum models encounter failure. In rock, failure occurs by the initiation of fractures or displacement along existing fractures (Igraffea, 1989). Due to their nature, continuum models cannot represent the creation of fractures or displacement along pre-existing ones. These methods deal with failure by assigning residual values to the continuum failing zones such that they approximate their physical counterparts by manipulating the continuum space. So, when using these methods, it is important to understand that they are only approximations of the underlying mechanisms that can help approximate the phenomenon of brittle rock failure but cannot fully explain it.

While the results from continuum numerical models for brittle rock failure might not replicate the actual conditions in the field, they are still helpful. A continuum model is computationally less expensive than discontinuum or hybrid methods. The use of these types of tools is also comparatively simple. Continuum methods can be used by rock mechanics practitioners who have experience in the field but are not at the leading edge of numerical model development. To model brittle rock using continuum models, the user does not need an extensive background in numerical models, just an understanding of rock mechanics and numerical models. Another reason to favour continuum numerical models is their commercial availability.

### 2.2.1 Hoek-Brown Brittle Parameters

One of the first attempts to model EDZ using continuum numerical models was developed by Martin (1995) and later expanded on by Martin et al. (1999). It was motivated by the field experiments at the URL. The method suggests modelling the excavation as an elastic material and calculating the factor of safety of the rock surrounding an excavation using the Hoek-Brown Brittle parameters. They recommend using an  $m = 0$  and  $s = 0.11$ . This set of parameters adequately predicts the stress-induced depth of failure. The Hoek-Brown brittle parameters are derived from the empirical observations by Martin et al. (1999) and the fact that crack initiation occurs at a stress of  $\approx 0.4 \times \sigma_{UCS}$  (Martin et al., 1999). The resulting depth of failure around a circular opening using these parameters can be simplified in terms of  $R_f/a$  and  $\sigma_{max}/\sigma_{UCS}$  similar to Equation (2-1). Then, both methods can be directly compared when using circular opening in a graphical representation, as seen in Figure 2-2 (Martin et al., 1999).



**Figure 2-2 Comparison of the empirical relationship between  $\sigma_{max}/\sigma_{UCS}$  and  $R_f/a$  and the predicted values using elastic numerical models and the Hoek-Brown brittle parameters (modified after Martin et al., 1999).**

Using the Hoek-Brown brittle parameter approach, Martin et al. (1999) tested different geometries and stress levels. They show that for the oval-shaped tunnels at the URL investigated by Read and Chandler (1997), the Hoek-Brown brittle parameter could predict that failure would occur and could generally approximate the size of the failure. In the same study, other tunnel geometries, such as horseshoe-shaped, were also successfully modelled

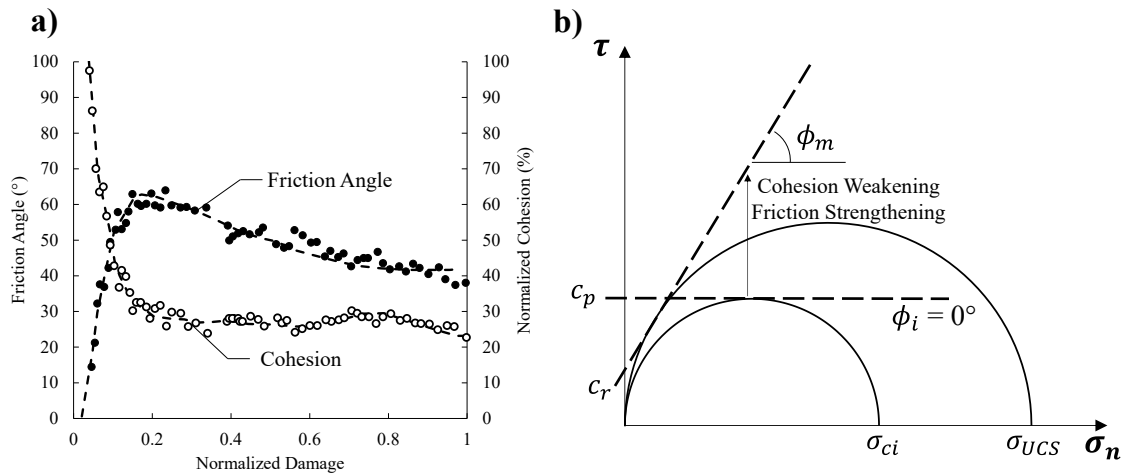
to predict the extent of failure. The same technique was later used by Martin and Maybee (2000) to investigate the failure of brittle rock pillars. In their investigation, they successfully correlated the predictions of hard-rock pillar stability using Hoek-Brown brittle parameters to empirical observations for pillar design.

Due to its use of elastic continuum numerical models and well-known engineering concepts such as the factor of safety, the Hoek-Brown brittle parameter method is the simplest of the numerical models. Yet, it adequately estimates the depth of failure, which can be used to support underground excavation design (Martin et al., 1999). It has also been used in different scenarios to a great degree of success (Martin et al., 1999; Kaiser et al., 2000; Martin and Maybee, 2000). To use this method, a rock mechanics engineer does not need a high level of understanding of numerical modelling to get an accurate and valuable prediction of the ground behaviour. It is also a quick method to implement and can be done using any continuum geotechnical numerical modelling software capable of elastic analysis, such as *RS2*, *FLAC*, *FLAC3D* or *Map3D*. As demonstrated in Figure 2-2, this technique also works for different stress regimes, approximating the depth of failure according to the in-situ stresses similar to the empirical equation developed by Martin et al. (1999). It was first suggested that this method be applied to 2D numerical methods. Since the process of brittle failure around a tunnel initiates near the face (Martin, 1997), the shape of failure cannot be accurately predicted with the Hoek-Brown brittle parameters. Therefore, it should only be used to determine the depth of failure. Another drawback of the method is its lack of representation of the EDZ.

### **2.2.2 Cohesion Weakening Friction Strengthening (CWFS)**

Martin and Chandler (1994) conducted experiments where they cyclically loaded an LdB granite sample under different confining conditions, from 0 to 15 MPa. They found that the rock loses cohesion and gains frictional strength as the sample is damaged. At low confinements, rock does not have permanent friction and cohesion. These strength components change as a function of damage and strain. By measuring damage and peak strength while cyclical loading, they were able to quantify these two mechanisms and the strain levels at which they occur. The results of their experiments are shown in Figure 2-3. They suggest that the onset of change in strength is at the  $\sigma_{ci}$  level, rather than at the  $\sigma_{UCS}$ ,

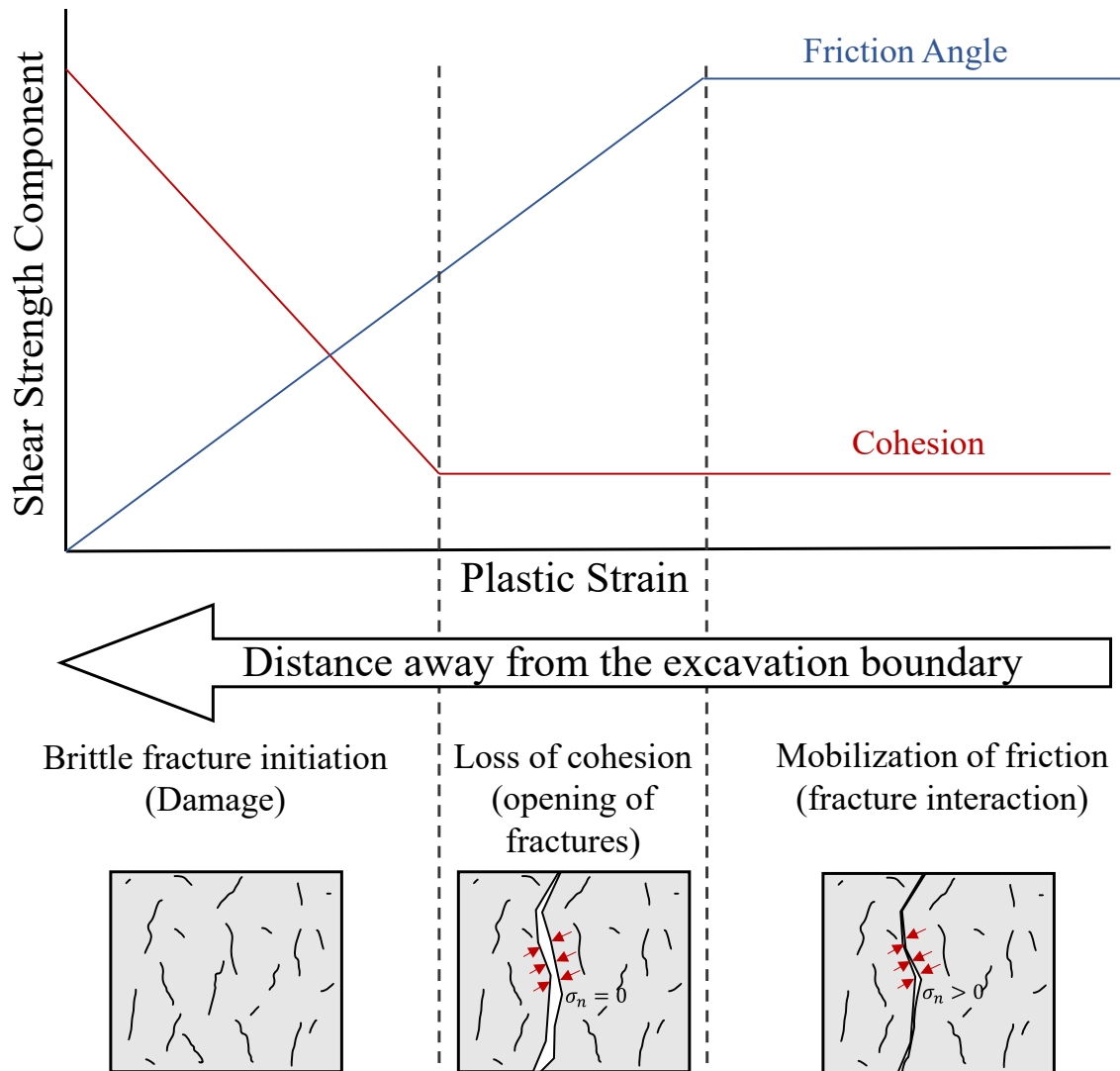
and that the maximum strength of a rock occurs after the cohesion and friction have reached their mobilized values. This mobilization is shown as Mohr circle plots in Figure 2-3b. Conventional Mohr-Coulomb failure criteria assume that failure occurs at a single shear plane. Brittle rock fails by two micromechanical behaviours before this final shear plane. It fails by the creation of initial microfractures, which leads to a loss of cohesion, and the development of such microfractures, which leads to the increase in friction (Hajiabdolmajid, 2001). Therefore, a dual failure behaviour is better suited for brittle rock, as seen in Figure 2-3b (Martin and Chandler, 1994).



**Figure 2-3 Results from the laboratory investigation of LdB granite under cyclic loading a) cohesion weakening friction strengthening of a UCS sample compared to normalized damage b) CWFS mechanism visualized with Mohr circle in shear-normal stress space (modified after Martin and Chandler, 1994).**

The results from those experiments prompted researchers to apply the same principles to failure around excavations in brittle rock (Hajiabdolmajid, 2001; Hajiabdolmajid et al., 2002; Hajiabdolmajid et al., 2003). Since an excavation boundary is a low confinement environment, the exact CWFS failure mechanism applies as in the laboratory test (Hajiabdolmajid, 2001). The CWFS process near excavation boundaries occurs due to the redistribution of stresses, creating a low confinement environment. Failure occurs first by the development of micro-cracks, yet to be interconnected, at the  $\sigma_{ci}$ . As loading increases, the microcracks develop and open, having no cohesion. Finally, with more stress, the fractures interconnect and mobilize, increasing the frictional strength between them (Corkum et al., 2012). This process occurs all near the excavation boundary, where, at equilibrium, there is

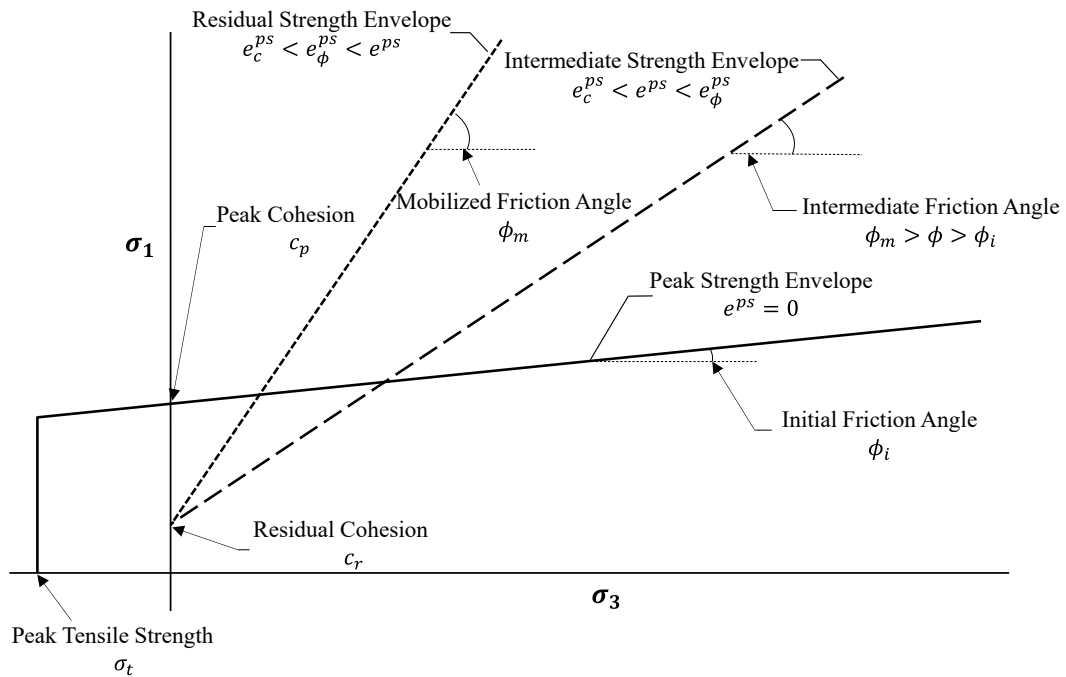
no cohesive strength, and the friction has fully developed. Farther from the boundary, fractures have separated enough to be cohesionless but have yet fully mobilized to increase friction. Only microfractures have started deeper into the rock mass, and the CWFS process has yet to develop. This relationship between the fracturing process and the depth into the rockmass is shown in Figure 2-4.



**Figure 2-4 Relationship between shear strength component mobilization and excavation boundary fracturing process with respect to fracturing interactions and evolution.**

Hajiabdolmajid et al. (2002) proposed that the brittle failure behaviour can be applied to continuum numerical models. As continuum models cannot explicitly simulate fracturing, they implemented the mobilization of strength parameters with respect to plastic strain. Using this idea, they developed the application of CWFS in *FLAC*. Failure around excavations in

brittle rock can be simulated using a continuum model by changing the strength of the rock after plasticity according to the ideas of CWFS. The parameters necessary for the application are the peak cohesion ( $c_p$ ), residual cohesion ( $c_r$ ), initial friction angle ( $\phi_i$ ), mobilized friction angle ( $\phi_m$ ), peak tensile strength ( $\sigma_t$ ), cohesion critical plastic strain ( $e_c^{ps}$ ), friction angle critical plastic strain ( $e_\phi^{ps}$ ), and dilation angle ( $\psi$ ) (Hajiabdolmajid, 2001). The critical plastic strain parameters numerically define the plastic strain at which each strength component has reached its residual value. The  $\psi$  determines the dilational behaviour of the rockmass after peak strength is reached. Applying these values to a numerical model gives three main failure envelopes. The peak failure envelope determined by the  $c_p$  and  $\phi_i$ , which has a low frictional component and high cohesion. The transitional failure envelope, which occurs at  $e_c^{ps}$ , in which the cohesion has reached  $c_r$ , but the  $\phi$  is not yet fully mobilized. The residual failure envelope at  $e_\phi^{ps}$ , which is the ultimate strength of rock. The theoretical three strength envelopes are shown in Figure 2-5.



**Figure 2-5** The three distinct CWFS theoretical failure envelopes showing the correlation between the strength parameters  $c$  and  $\phi$ , and the critical plastic strains  $e_c^{ps}$  and  $e_\phi^{ps}$  in  $\sigma_1 - \sigma_3$  space.

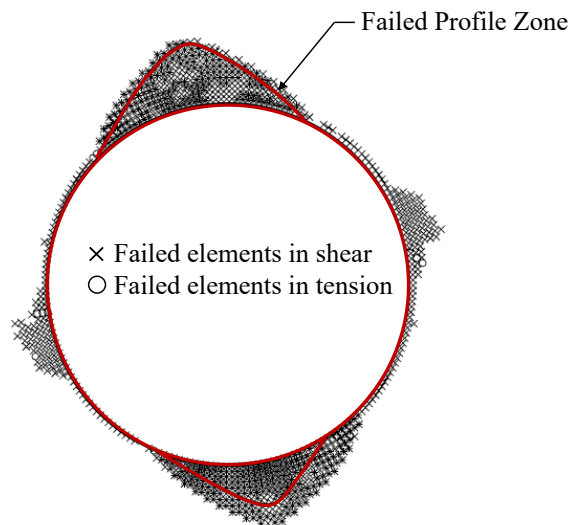


### 2.2.2.1 Application of the CWFS method

Hajiabdolmajid et al. (2002) applied this method to the MBE at the URL. After calibration, they suggested the strength parameters from Table 2-2. They used *FLAC* to model this case scenario. The results from their investigation compared to the field MBE failure observations are shown in Figure 2-6. Failure was monitored using failed elements in the model. They achieved an adequate match to the top v-notch observed at the MBE. Their models show failure tensile failure on the sides of the excavation. This failure was not visible in the field observations; however, acoustic emissions showed some failure around this area that did not present as unravelling of the rock (Martin and Kaiser, 1996). These results demonstrate the viability of the CWFS method in representing failure around underground excavations in brittle rock. Their investigation only focused on the failure profiles, and the authors reported no details about displacement and deformation.

**Table 2-2 Strength parameters to model the MBE at the URL using the CWFS method in FLAC (after Hajiabdolmajid et al., 2003)**

Parameter	Initial/Peak	Mobilized/Residual
Cohesion (MPa)	50	15
Friction Angle (°)	0	48
Dilation Angle (°)	30	30
Cohesion Critical Plastic Strain (%)		0.2
Friction angle Critical Plastic Strain (%)		0.5



**Figure 2-6 Results of the application of the CWFS method to simulate the MBE using the strength parameters from Table 2-2 (after Hajiabdolmajid et al., 2003)**

The CWFS method can estimate and predict failure around underground excavations in brittle rock. Since it is a continuum method, its application is relatively simple. Many commercially available software, like *FLAC*, *FLAC2D*, and *FLAC3D*, can be used to apply this approach. It cannot represent the failure due to its continuum nature; therefore, the strength parameters used and their evolution with strain are abstractions of actual mechanisms. Users must keep in mind the shortcomings of the continuum nature of the CWFS method. It is often used to analyze failure profiles rather than displacement. As an initial stage for underground design, the CWFS method is a viable tool. It also has the advantage of being simple to interpret. As such, this method has been extensively investigated in the literature, and multiple improvements and modifications have been made.

#### 2.2.2.2 Guidelines for input parameters selection for the CWFS method

Selecting input parameters for the CWFS method is one of its biggest challenges. The strength parameters are not simply obtained from laboratory experiments. To address this issue, Walton (2019) suggested an initial set of guidelines for the selection of input parameters. They developed these guidelines by looking at successful uses of the CWFS (and CWFS-like) method in literature and generating linear regression between the strength parameters and the rock mass characteristics of each case study. Fourteen different literature cases were used for the linear regression. With these cases, Walton (2019) created guidelines for all input strength and elastic parameters  $c_p$ ,  $c_r$ ,  $\phi_i$ ,  $\phi_m$ ,  $e_{crit}^{ps}$ ,  $e_{\phi}^{ps}$ , and  $\psi$ . The guidelines use the correlations found from literature, laboratory values of the rock of interest, and geological knowledge of the rock to suggest an initial value.

The  $c_p$  is dependent on the selection of  $\phi_i$  and is selected according to the following equation (Walton, 2019):

$$c_p = \frac{\sigma_{in-situ} \times (1 - \sin \phi_i)}{2 \times \cos \phi_i} \quad (2-6)$$

where  $\sigma_{in-situ}$  is the in-situ unconfined rock strength. Various authors have proposed this to be the laboratory  $\sigma_{ci}$  of the rock and is between 30 and 50% of the  $\sigma_{UCS}$  (Martin, 1997). It is best to determine  $\sigma_{ci}$  with laboratory tests; however, if unavailable, it can be estimated with (Walton, 2019):

$$\sigma_{in-situ} = 0.41 \times \sigma_{UCS} \quad (2-7)$$

The  $\phi_i$ , from the experiments of Martin and Chandler (1994), is suggested to be  $0^\circ$ . Diederichs (2007) suggested that it should follow the confinement-dependent crack initiation threshold, at around  $10^\circ$  to  $25^\circ$ . With linear regression of multiple literature uses of the CWFS, Walton (2019) suggested that the  $\phi_i$  ranges from  $0^\circ$  to  $20^\circ$ , where the higher the  $\sigma_{in-situ}$  the lower the  $\phi_i$ .

Due to its abstract nature,  $c_r$  is a complex value to estimate. As the CWFS method is used in continuum numerical models, the  $c_r$  is the cohesive strength of the rock bridges after fracturing. While the fractures themselves do not have any cohesion, the rock mass does. Via linear regression of literature values, Walton (2019) suggested that it can be estimated with:

$$c_r = -0.46 + 0.76 \times c_p \quad (2-8)$$

where the  $c_p$  must be in MPa. Significant calibration needs to be performed from this suggested value due to its uncertainty (Walton, 2019)

The  $\phi_m$  is suggested to be the friction angle of the "spalling limit" or the long-term strength of the rock mass (Diederichs, 2007). It is suggested that this spalling limit corresponds to a  $\sigma_1/\sigma_3$  of 10 to 20, which is an equivalent friction angle of  $55^\circ$  to  $65^\circ$ . The range suggested by the CWFS method in the literature is between  $45^\circ$  to  $65^\circ$ . The value can be more directly obtained by relating it to the Hoek-Brown  $m_i$  parameter from triaxial testing, the correlation is (Walton, 2019):

$$\phi_m = 20 + 1.33 \times m_i \quad (2-9)$$

The critical plastic strain has been argued to be a true material component (Martin and Chandler, 1994; Hajiabdolmajid et al., 2002); therefore, the property can be determined from laboratory experiments. These experiments consist of cyclic loading and strain monitoring of rock masses, which are hard to perform. Alternatively, Walton (2019) suggests that  $e_c^{ps}$  can vary from 0.1% to 0.3%. the  $e_\phi^{ps}$  is determined by the  $e_c^{ps}$  and  $\phi_i$  as follows (Walton, 2019):

$$e_\phi^{ps} = \begin{cases} e_c^{ps}, & \phi_i > 10^\circ \\ 2 \times e_c^{ps}, & \phi_i \leq 10^\circ \end{cases} \quad (2-10)$$

The dilation angle has often been suggested to be a constant parameter that must satisfy  $\psi < \phi$  (Walton, 2019). The suggested value, if a constant  $\psi$  is to be used, is given by (Walton, 2019):

$$\psi = \phi_m \times \left( \frac{\sigma_{in-situ}}{3\sigma_3 - \sigma_1} - 0.1 \right) \quad (2-11)$$

Alternatively, the constant dilation can be obtained from laboratory testing. While this constant dilation can still produce satisfactory results, there is increasing interest in representing dilation as a variable parameter that is a function of confining stress and shear strain. Walton (2019) details the modification of the dilation angle given these criteria.

The initial guidelines Walton (2019) suggested add significant value to the CWFS method. They ease the use of the CWFS method for design, particularly at the early stages of a project where limited information on the rock mass is known. With knowledge of the rock and some estimations, a rock mechanics designer can use these guidelines to get an initial idea of the brittle rock response of an excavation. These strength parameters can then be modified as more knowledge is gained throughout the project. The full details of the linear regression and guideline formulation can be found in Walton (2019).

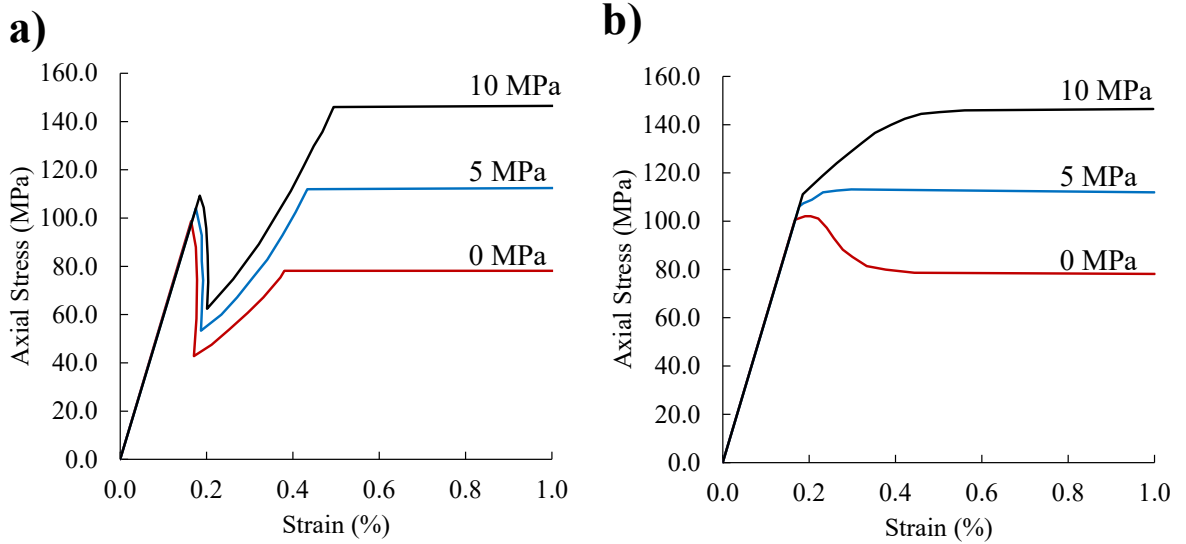
#### 2.2.2.3 Modification of the Critical Plastic Strain Parameters

When modelling a triaxial test using the strength values suggested by Hajiabdolmajid (2001) Hajiabdolmajid et al. (2002) and Hajiabdolmajid et al. (2003), an unrealistic behaviour arises (Renani and Martin, 2018). This behaviour occurs after the peak strength envelope is reached. At this point, the rock mass behaves in a brittle manner, losing strength. However, with an accumulation of plastic strain, the rock gains strength as friction increases. Figure 2-7a shows the results of the triaxial behaviour in *FLAC* as conducted by Renani and Martin (2018). The initial loss of strength accompanied by a strength increase is due to the non-simultaneous mobilization of strength with plastic strain. Since  $e_c^{ps} < e_\phi^{ps}$ , the rock loses its cohesive strength before gaining frictional strength (see Figure 2-5). To mitigate this problematic behaviour, Renani and Martin (2018) suggested two changes to the plastic behaviour of the CWFS. The first was to make the mobilization of strength parameters simultaneous by making  $e_c^{ps} = e_\phi^{ps}$ . The second is to make the mobilization of the strength parameters non-linear. They suggest modifying the linear relationship, shown in Figure 2-4, to exponential relationships given by (Renani and Martin, 2018):

$$c = c_r + (c_p - c_r) \left[ 2 - \frac{2}{1 + \exp\left(-5 \times \frac{e^{ps}}{e_c^{ps}}\right)} \right] \quad (2-12)$$

$$\phi = \phi_i + (\phi_m - \phi_i) \left[ \frac{2}{1 + \exp\left(-5 \times \frac{e^{ps}}{e_\phi^{ps}}\right)} - 1 \right] \quad (2-13)$$

where  $e^{ps}$  is the current plastic strain,  $c$  is the instantaneous cohesion,  $\phi$  is the instantaneous friction angle, and  $e_\phi^{ps} = e_c^{ps}$ . Using these two modifications, simulated triaxial test results more adequately represent the laboratory test, as seen in Figure 2-7b.



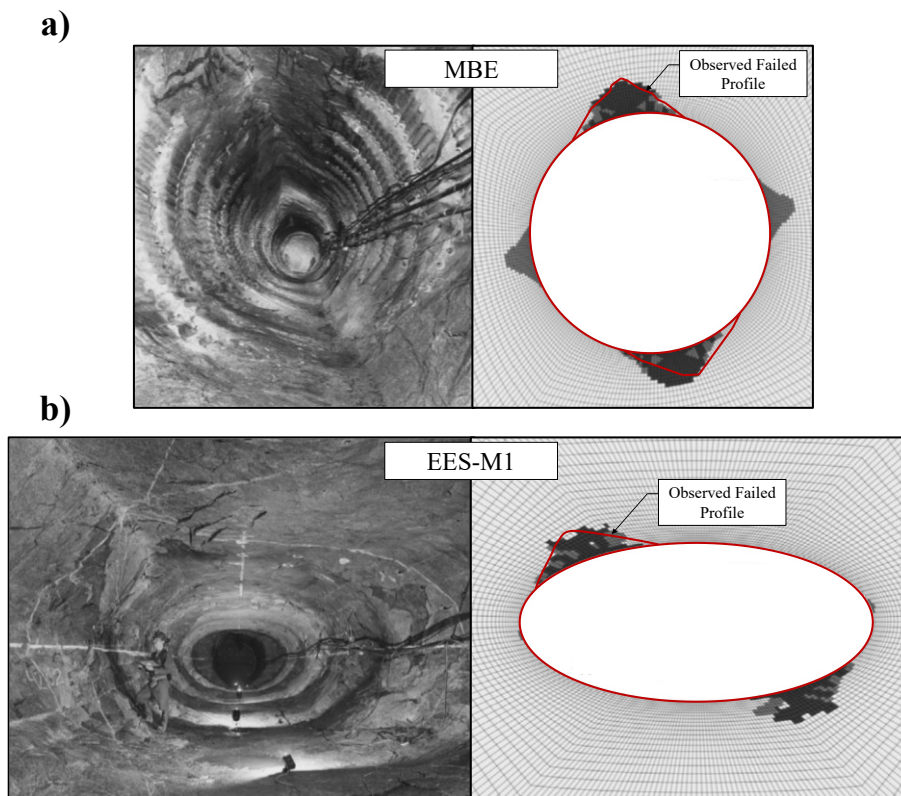
**Figure 2-7 Results of the simulated triaxial test on LdB granite for 0 MPa, 5 MPa, and 10 MPa using the CWFS method in FLAC with a) linear and non-simultaneous plastic strain relationship b) non-linear and simultaneous plastic strain relationship (modified after Renani and Martin, 2018).**

They later applied these modifications to the MBE at the URL. They perform a parametric sensitivity analysis on all the input parameters. After calibration, they found the best match to the field observations to be:  $c_i = 55$  MPa,  $c_r = 5.5$  MPa,  $\phi_i = 0^\circ$ ,  $\phi_m = 42^\circ$ , and  $e_c^{ps} = e_\phi^{ps} = 0.5\%$ . The results of this investigation are shown in Figure 2-8a. They also modelled other excavations at the URL, such as the EES-M1. The results of this tunnel also matched the field observations (Figure 2-8b). From their parametric study, they found that the  $c_p$  and

$c_r$  have the largest effect on the  $d_f$  while the  $\phi_i$  and  $\phi_m$  have the largest effect on the angle of failure (Renani and Martin, 2018). They also suggest some guidelines for the selection of the input strength parameters. The  $c_i$  can be estimated by:

$$c_i = \frac{\sigma_{UCS_{in-situ}}}{2} \left[ 0.3 + \frac{0.2}{1 + \exp(26 - 0.3 \times GSI)} \right] \quad (2-14)$$

where  $GSI > 75$ . They also suggest that  $c_r = 0.1 \times c_p$ . The  $\phi_i = 0$ , with  $\phi_m$  being dependent on the rock type:  $34^\circ$  for igneous rock;  $33^\circ$  for sedimentary rock; and  $29^\circ$  for metamorphic rock. Lastly, they suggest that  $e_c^{ps} = 0.5\%$  (Renani and Martin, 2018).



**Figure 2-8 Results of the simulation and calibration of the modified CWFS method for a) the MBE, showing the observed failed profile, and b) the EES-M1, showing the approximated observed failed profiles (modified after Renani and Martin, 2018).**

#### 2.2.2.4 Instantaneous Cohesion Weakening Friction Strengthening

An inherent mechanism from the CWFS method's development is that the strength parameter evolution is strain-dependent. Some continuum numerical modelling software, such as *RS2* (in earlier code versions), do not allow strain-dependent strength evolution. Elderboro (2009) proposed that the same principles of CWFS can be applied with "instantaneous" strength

change in *Phase2* (now *RS2*). They coined this method as the Instantaneous Cohesion-Softening Friction-Hardening model. The theory behind its development is the same as the CWFS method proposed by Hajiabdolmajid et al. (2002); however, the application of the method differs. Elderboro (2009) suggest that  $c_p$  is given by:

$$c_p = \frac{\sigma_{ci} \times (1 - \sin \phi_m)}{2 \times \cos \phi_m} \quad (2-15)$$

They also suggest that  $\phi_m = 10^\circ$ , as  $0^\circ$  results in an overestimation of  $d_f$  and angle of failure. They suggest that  $c_r$  can be estimated as (Elderboro, 2009):

$$c_r = 0.3 \times c_p \quad (2-16)$$

The  $\phi_m$  is equal to the measure's laboratory friction angle of the rock. Lastly, the  $\psi$  can be varied from  $0^\circ$  to  $20^\circ$  (Eldeboro, 2009). Of note is the lack of  $e_c^{ps}$  and  $e_\phi^{ps}$ , this is due to the instantaneous nature of the method. The interpretation of the results also differs from the CWFS method. Instead of monitoring failed zones, they suggest that the spalling depth of the tunnel should be measured according to shear strain. Where two shear bands meet is where there is assumed to be spalling, and the rock has unravelled (Elderboro, 2009)

Eldeboro (2009) applied this method to six different tunnels. These case studies range in geological setting, shape, buried depth, and stress regime. The failure profile was matched for three: two were overestimated, and the remaining one was underestimated. Looking at maximum shear strain was a more reliable method to determine where failure had occurred. Elderboro (2010) conducted a parametric study on the instantaneous CWFS method. They determined that the parameters with the most significant effect on the results are the  $\psi$  and  $c_p$ . The following most influential parameter is  $\phi_i$ . The residual parameters and tension have a minor influence on the results. Their study also showed that the method implemented in *Phase2* is sensitive to mesh density; however, this can be mitigated by using small enough element sizes near the excavation boundary (Elderboro, 2010).

The investigation by Elderboro (2009) and Elderboro (2010) demonstrates that the CWFS method is not only applicable to codes with strain-dependent softening/hardening capability. They showed that by using a different interpretation technique, maximum shear strain, the  $d_f$  and failure profile can be estimated. All the shortcomings of the CWFS method apply in this application. It does not represent the true mechanistic behaviour of the rock and does not

show the fracturing process and rock unravelling after failure. The main advantage of this instantaneous application is that the  $e_c^{ps}$  and  $e_\phi^{ps}$  values do not need to be estimated, facilitating the use of the method for rock engineering practitioners.

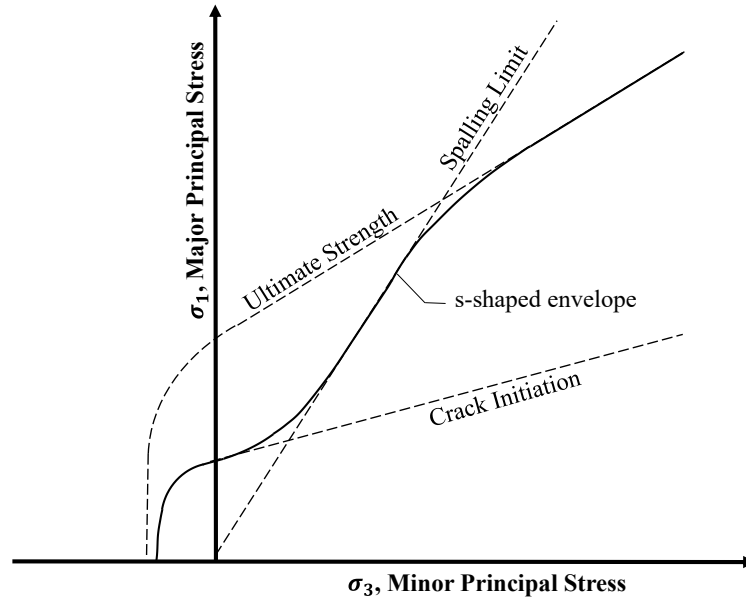
### 2.2.3 Damage Initiation Spalling Limit (DISL)

The Damage Initiation Spalling Limit (DISL) method was proposed by Diederichs (2007) to simulate brittle rock failure around underground excavations. The formulation and development of this method are not too dissimilar to that of CWFS. The idea of the method stems from the suggestion that two mechanisms drive failure around underground excavations. The first is the "Lower bound strength," or Damage Initiation, which is the strength of the rock at lower confinement and is dominated by the crack initiation under constant deviatoric stress. This crack initiation stress is given by (Martin, 1994):

$$\sigma_{ci} = A \times \sigma_{UCS} + \sigma_3 \quad (2-17)$$

where  $A$  varies from 0.3 to 0.5 for most nonporous-nonfoliated rocks. At low confinements, this is the strength at which cracks that are initiated can propagate, creating the characteristic spalling slabs. At higher confinements, failure is dominated by the "Upper bound strength" or crack interaction, characterized by the rock's long-term yield strength. The crack interaction strength can be determined by the stress at which the laboratory sample's stress-strain measurement deviates from linearity, often called crack damage stress,  $\sigma_{cd}$  (Martin and Chandler, 1994). The strength at this high confinement has a high  $\phi$  as there is direct interaction between fractures sliding from one another. A transitional curve exists between the crack initiation and the crack interaction, the spalling limit. This spalling limit is determined from the experiments by Hoek (1968) and the numerical modelling results of Diederichs (2007). Figure 2-9 shows these two dominant mechanisms and the transitional curve in  $\sigma_1 - \sigma_3$  space which create an s-shaped envelope.





**Figure 2-9 The DISL method theoretical s-shaped envelope in  $\sigma_1 - \sigma_3$  space showing the three defining strength envelopes: crack initiation strength, spalling limit strength, and ultimate strength (modified after Diederichs, 2007)**

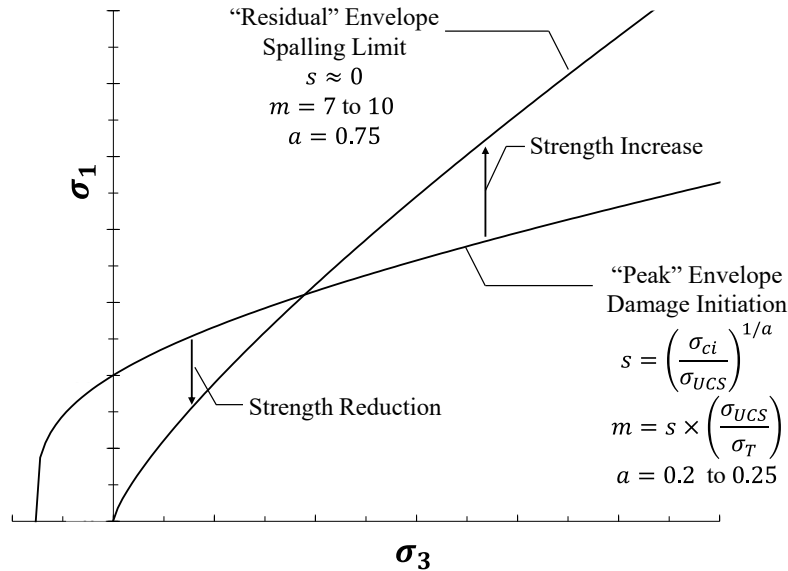
Diederichs (2007) applied the DISL method using the continuum software *Phase2* (now *RS2*). As the s-shaped envelope cannot be directly applied to the software, the method uses peak and residual Hoek-Brown failure envelopes. The peak envelope is determined by the strength of the crack initiation envelope (constant deviatoric stress). Diederichs (2007) suggests determining this envelope with:

$$s = \left( \frac{\sigma_{ci}}{\sigma_{UCS}} \right)^{\frac{1}{a}} \quad (2-18)$$

$$m = s \times \left( \frac{\sigma_{UCS}}{\sigma_T} \right) \quad (2-19)$$

where  $a$  can be 0.2 for a conservative simulation and 0.25 for the best-case scenario. They suggest obtaining  $\sigma_{ci}$  with acoustic emission from laboratory testing, and  $\sigma_T$  from laboratory tensile testing. The spalling limit/residual envelope can be determined by  $a = 0.75$  to ensure the curvature matches the long-term strength of laboratory samples. The slope of this spalling limit is given by  $\sigma_1/\sigma_3 = 7$  to 10, and  $s$  should approach 0 to simulate the lack of cohesion from the interaction of fractures (Diederichs, 2007). The damage initiation and spalling limit envelopes can be seen in Figure 2-10. Applying these peak and residual envelopes creates a bi-modal behaviour of the rock after plasticity. There is a strength reduction/softening at low

confinements, while at higher confinement, the rocks experience a strength increase/hardening. This dual behaviour is shown in Figure 2-10. A set of guidelines for obtaining these parameters from laboratory testing can be found in Diederich and Martin (2010).



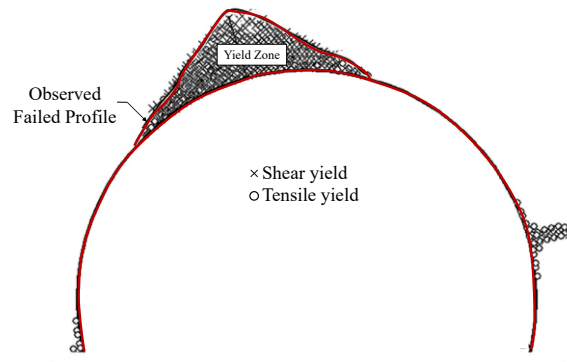
**Figure 2-10 "Peak" and "Residual" strength envelopes in  $\sigma_1 - \sigma_3$  space for the application of the DISL method in RS2, the zones of the strength increase, and strength decrease after plasticity, and the suggestions for input parameter selection (modified after Diederichs, 2007)**

### 2.2.3.1 Application of the DISL method

The DISL method was applied to the MBE at the URL by Diederichs (2007). They suggested using the values detailed in Table 2-3 for LdB granite. To determine the failure profile, they suggested looking at failed zones. The extent of failed zones is the prediction of HDZ for the DISL method. Their results closely match the observed failure profile at the top of the MBE, as shown in Figure 2-11. They also did a theoretical stress regime investigation in which they found that the DISL method can reproduce the empirical observation by Martin et al. (1999) of  $d_f$  at different stress levels. The DISL method has also been successfully implemented for brittle rock modelling around underground excavations by multiple other authors (Diederichs et al., 2010; Corkum et al., 2012; Perras et al., 2014; Dressel and Diederichs, 2022; Doroodian et al., 2022; Ramirez and Delonca, 2023).

**Table 2-3 Strength parameters to model the MBE at the URL using the DISL method in *Phase2* (after Diederichs, 2007)**

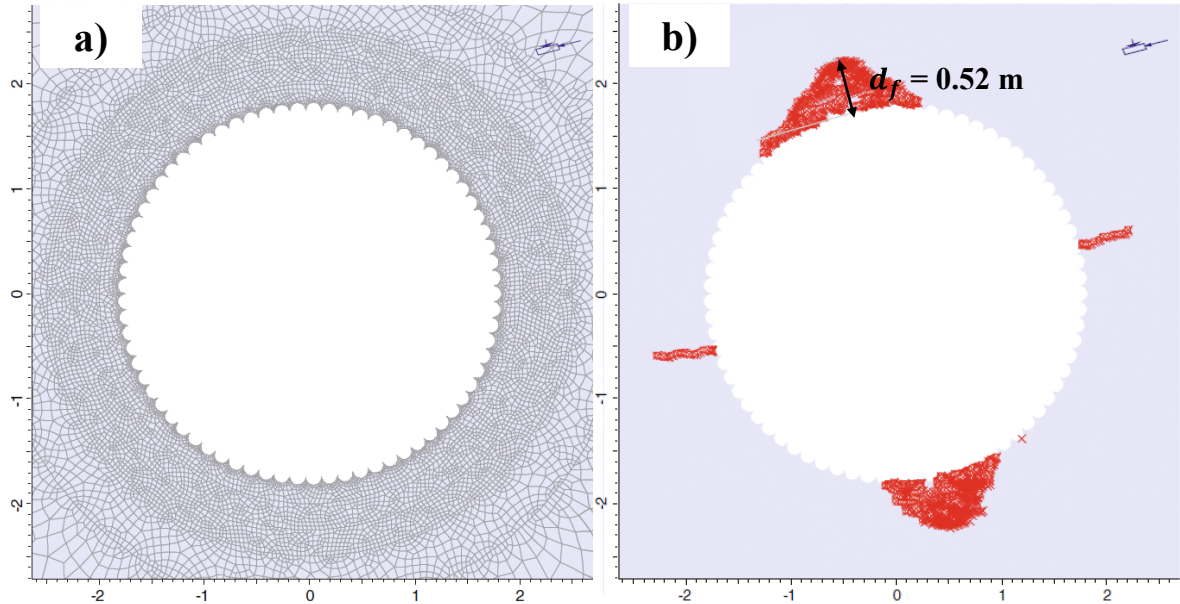
Parameter	Peak	Residual
$a$	0.25	0.75
$m$	1	7
$s$	0.033	0
$\sigma_{UCS}$ (MPa)	230	



**Figure 2-11 Application of the DISL method in *PHASE2* (now *RS2*) to the MBE at the URL showing the predicted failure profile for the top section of the tunnel (modified after Diederichs, 2007)**

### 2.2.3.2 Realistic "as-built" tunnel boundary DISL method

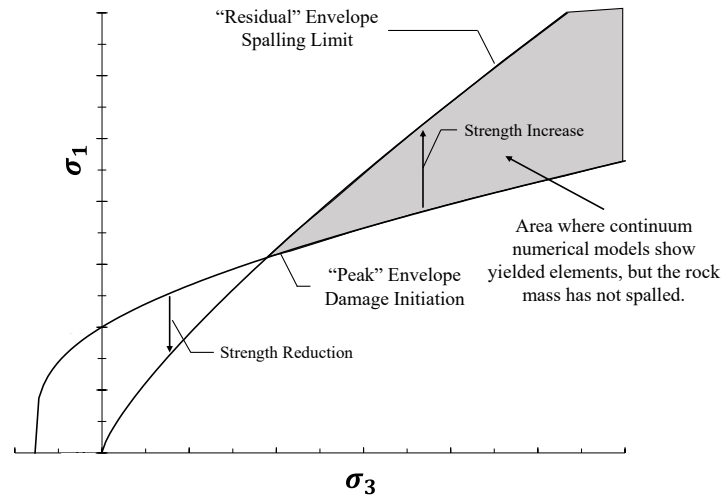
Cai and Kaiser (2014) proposed that the Damage Initiation strength Diederichs (2007) suggested is unrealistically low. They state that the actual Damage Initiation strength is not determined by the  $\sigma_{ci}$  but the  $\sigma_{cd}$  (crack damage). This entails that the selection of the unconfined strength increases from  $0.4 \times \sigma_{UCS}$  to  $0.8 \times \sigma_{UCS}$ . They suggest that this strength reduction is just "apparent" and a result of simulating the excavation as having a smooth boundary. They state that this redistributes the stresses differently from the field. They suggest that this apparent increase in strength can be mitigated if the numerical models are simulated with the as-built geometries. This geometry generates higher stress locations that require a higher strength to produce the same amount of failure. They tested this theory with the MBE as-built geometry, where they explicitly simulated the line drilling used to excavate the tunnel (Figure 2-12a). They found that applying the DISL method with the unconfined compressive strength of  $0.8 \times \sigma_{UCS}$  and actual field geometry accurately represent the v-notch formation in the field, as seen in Figure 2-12b.



**Figure 2-12 a) As-built geometry and discretization of the MBE tunnel applied in RS2 for the application of the DISL method. b) Result of the application of the DISL method with as-built geometry with input  $\sigma_{UCS} = 0.8 \times \sigma_{UCS}$  showing a  $d_f$  comparable to the field observations (modified after Cai and Kaiser, 2014).**

### 2.2.3.3 The DISL method for interpreting the EDZ

Perras and Diederichs (2016) suggested that the interpretation of the results of the DISL method should not only focus on yielded elements to determine the HDZ. They instead offer an alternative interpretation of the EDZ using the DISL method. They proposed that at certain stresses (shaded area in Figure 2-13) numerical models present yielded elements. At this stresses, spalling has not occurred, as seen in Figure 2-9, but the model points out yielded elements. As such they devised an alternative interpretation of the numerical modelling results to better categorize HDZ, EDZ, and EIZ.



**Figure 2-13 "Peak" and "Residual" strength envelopes in  $\sigma_1 - \sigma_3$  space for the application of the DISL method in *RS2* showing the "problematic" zone where continuum numerical models show yielded elements, but the rock is not part of the HDZ, suggesting the need for an alternative interpretation of the HDZ using this tool.**

Perras and Diederichs (2016) suggest that the results of the numerical models need to be interpreted differently to find the predicted HDZ. Furthermore, having an alternative interpretation also allows for the determination of different zones of the EDZ, such as the  $EDZ_i$  and  $EDZ_o$ . The guidelines to interpret the numerical results by the DISL method are:

1. HDZ to  $EDZ_i$  transition: the location where the rock mass is capable of holding confining stresses. Numerically, it should be found by looking at the distribution of  $\sigma_3$  and finding the boundary where  $\sigma_3$  increases from 0 or the value at the boundary. Near 0 confinement means the rock mass has unravelled, creating the spalling zone. These criteria deal with the "problematic" area suggested in Figure 2-13.
2.  $EDZ_i$  to  $EDZ_o$  transition: It is the point where tensile volumetric strain starts. This is the stress level of volumetric strain reversal defined by Martin and Chandler (1994).
3.  $EDZ_o$  to EIZ transition: This is determined by the yielded elements.

This methodology was applied to several hypothetical scenarios with different rock types to a reasonable degree of accuracy. This investigation was also used to determine the empirical equations from Section 2.1.3.

The DISL method for brittle rock failure modelling around underground excavations is a well-understood and thoroughly investigated tool. It was developed with a sound mechanistic

approach that can work in continuum numerical models. It has been shown to predict the HDZ adequately, and with the suggestions by Perras and Diederichs (2017), it can also determine the entire EDZ profile. However, the user requires deep knowledge and expertise in numerical modelling to do so effectively. This type of interpretation adds a certain level of subjectivity. Like all other continuum methods, this interpretation is an abstraction of the actual mechanical behaviour of the rock. It does not explicitly present failure and fracturing of the rock mass. Thanks to its theoretical background, the selection of input parameters is aided, making the method more straightforward to implement.

#### **2.2.4 FRACOD**

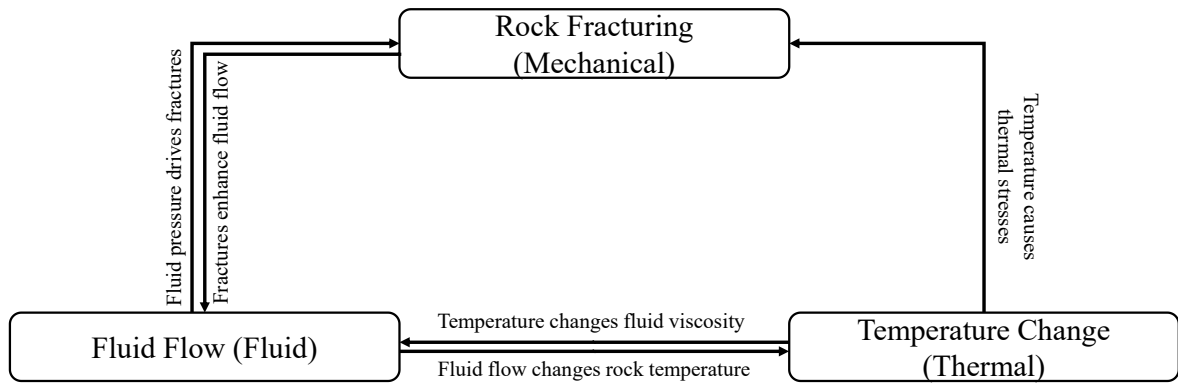
*FRACOD* is a commercially available continuum numerical modelling software developed to simulate fracture growth in rock accounting for mechanical, hydrological, and thermal conditions. It is a Boundary Element Method (BEM) with an incorporated fracture mechanics criterion that allows the simulation of the fracturing process. A BEM is based on the displacements in a finite line segment, which can either be the excavation boundary or a crack (Shen, 2014). The matrix of the model is assumed to be continuous and infinite (Shen, 2014). They suggested a method called the 'F-criterion' to implement fracture creation and propagation. This method is a modification of the Maximum Strain Energy Release Rate Criterion (G-Criterion). This original G-criterion suggests that a fracture is created or propagated if the strain energy release in a given direction exceeds a critical value  $G_c$ . Two fracture mechanisms comprise the total strain release  $G_c$ : mode I and mode II. Mode I is the fracture propagation in tension, and mode II is the fracture propagation in shear. One issue of the G-criterion for rock is that it does not distinguish between modes as long as the  $G_c$  is reached, a fracture would propagate. Shen (2014) proposed the F-criterion as they suggest that the G-criterion is invalid due to rock being much weaker in tension than in shear, meaning that mode I would dominate the crack creation. To address this issue, the F-criterion normalizes according to the  $G_c$  in each mode. The principles of this criterion are (Shen, 2014):

1. In any direction ( $\theta$ ) at a fracture tip, the  $F$  value can be calculated with:

$$F(\theta) = \frac{G_I(\theta)}{G_{Ic}} + \frac{G_{II}(\theta)}{G_{IIc}} \quad (2-20)$$

2. The direction of propagation is towards which  $F$  reaches its maximum.
3. When the maximum  $F$  reaches 1, the fracture tip propagates in the direction of  $\theta$ .

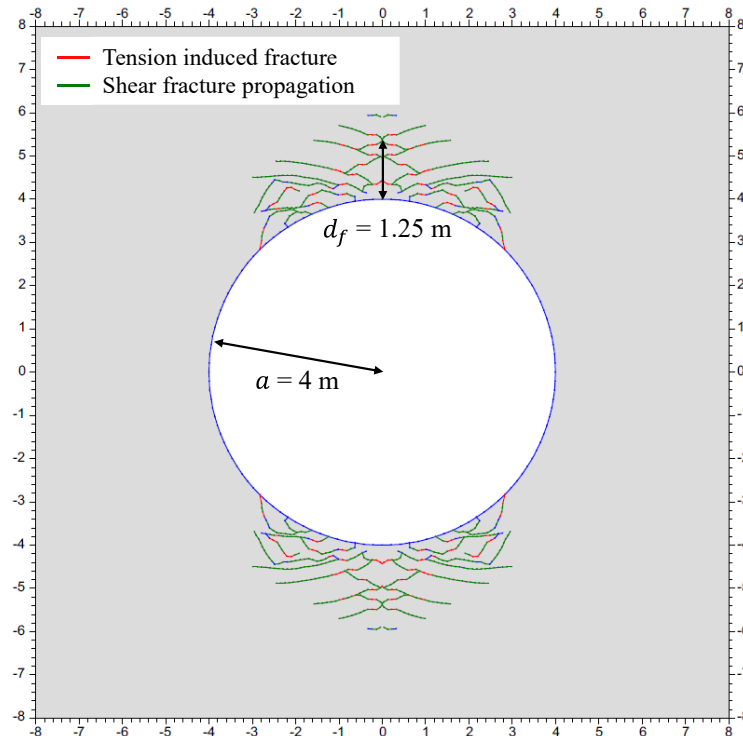
The normalization with  $F$  allows for a less biased fracture mechanism due to low tensile strength (Shen, 2014). Once fractures are created, the stiffness of the contacts is dominated by normal and shear stiffness ( $k_n$  and  $k_s$ ). New fracture strength is implemented after fracture creation and propagation. The new fracture strength is defined by the cohesion and friction angle. The strength of the rock matrix uses a Mohr-Coulomb strength envelope, and the stiffness is controlled by  $E$  and  $\nu$  (Shen, 2014). FRACOD is also fully coupled for hydrological and thermal behaviour (Shen, 2014), as shown in Figure 2-14. The reader is encouraged to read Shen (2014) for an in-depth explanation of the software.



**Figure 2-14 Mechanical-Thermal-Fluid coupled interactions for the *FRACOD* BEM software (modified after Shen, 2014)**

Since FRACOD is capable of propagating fractures around underground excavations, it is a great candidate to be able to model failure in brittle rock. Barton and Shen (2017) applied this method to some theoretical tunnels to demonstrate its capabilities. The theoretical scenario tested uses the rock mass strength from the Aspo diorite with a  $\sigma_H = 50$  MPa and  $\sigma_v = 25$  MPa, i.e.  $k = 2$ . The strength chosen is:  $c = 31$  MPa,  $\phi = 49^\circ$ ,  $\sigma_t = 14.8$  MPa. The  $G_{IC}$  is  $3.8 \text{ MPa/m}^{1/2}$  and  $G_{IIC}$  is  $4.7 \text{ MPa/m}^{1/2}$ . The results of this investigation gave positive insight into the mechanism of spalling using FRACOD. They obtained a depth of failure,  $d_f/a = 0.25$ , similar to the one suggested using Martin et al. (1999) equations (Barton and Shen, 2017). Figure 2-15 shows the results of the theoretical study after reaching equilibrium, the depth of failure, and the type of fractures. Other conclusions from the use of the model were:

- Fractures occurred at maximum tangential stress location, and fracture initiation occurred due to tensile strain in the radial direction at a direction subparallel to the excavation boundary.
- Propagation of the new fractures is predicted to be in shear at an angle from the tunnel wall.
- As the fractures propagate into the rock mass, new fractures are created parallel to the rock mass but deeper into the rock.



**Figure 2-15 Long-term equilibrium for a theoretical tunnel in Aspo diorite modelled with *FRACOD* demonstrating the type of fractures and the depth of failure simulated (modified after Barton and Shen, 2017).**

FRACOD has been used relatively successfully by SKB to simulate a real failure scenario (Rinne et al., 2004). They used the Aspo pillar stability experiment as a case study to model with FRACOD. This experiment involved the excavation of the pillars and the hydraulic loading of the walls to simulate backfill and the thermal loading by electric heating to simulate the effect of nuclear waste (Rinne et al., 2004). In their report, the authors give the input parameters used to simulate the strength of the rock but give no further insight into the acquisition of those parameters or if there was calibration. They tested different locations on the pillars. They also used a time-dependent scheme that accounted for the loading and



heating times of the pillars (Rinne et al., 2004). The results of the models could simulate the results from the Aspo experiment as well as successfully demonstrate the effect of heating and backfill of the excavation boundary (Rinne et al., 2004)

There are some clear advantages of using FACOD to simulate brittle rock failure around underground excavations, particularly for nuclear waste disposal applications. To the author's knowledge, it is the only continuum modelling software that allows for the creation of new fractures using fracture propagation energies. For EDZ modelling, this capability is crucial as it allows for a visualization of the extension of cracks concerning the depth of failure and crack development into the rock mass. This information can help to monitor the change in hydraulic conductivity of the rock mass and its long-term strength. It is also suitable for thermal and hydraulic loading with a robust coupling system. As conditions change in a DGR, the effect of thermal changes and fluid flow greatly impacts the stability of the deposition tunnels. While the method seems suitable for EDZ modelling, there are still some barriers to its use. There is no extensive investigation and validation for its use in excavation design in brittle rock. There are some examples of its use (Rinne et al., 2004; Shen, 2014; Barton and Shen, 2017), but none are overly conclusive. There are also no guidelines on using this software for brittle rock. The main parameter that might cause difficulty is critical fracture strain energy for both modes ( $G_{Ic}$  and  $G_{IIc}$ ). The determination of these parameters is a calibration task after observations. Furthermore, after fractures are created, the strength of such fractures needs to be defined, opening the method to more interpretation by the modeller.

### **2.2.5 2D Continuum-Based Voronoi Tessellated Models**

With the introduction of joint networks into continuum numerical models, it has been proposed that some, such as the Voronoi joint network, can be used to simulate the granular structure of brittle rock (Li and Bahrani, 2021a) and rock mass scale heterogeneities (Li and Bahrani, 2021b). Noting the good agreement from the laboratory simulation using Voronoi Tessellated Models (VTM), Sanipour et al. (2022) used a VTM to simulate brittle rock failure around underground excavations. To develop their method, they used the MBE at the URL as a case study and the software *RS2* (Rocsience, 2021). When utilizing Voronoi joint networks tessellated models in *RS2*, 16 strength and deformation properties are required to

calibrate, as summarized in Table 2-4. The calibration requires not only the strength and deformation of the blocks but of the joint elements as well (Sanipour et al., 2022).

**Table 2-4 Strength and deformation properties of VTM in RS2 (Sanipour et al. 2022)**

Properties	Block (i.e. mesh elements)	Block Boundaries (i.e. joint elements)
Peak Strength	Cohesion, $c_{pb}$ (MPa)	Cohesion, $c_{pbb}$ (MPa)
	Friction angle $\phi_{pb}$ ( $^{\circ}$ )	Friction angle $\phi_{pbb}$ ( $^{\circ}$ )
	Tensile strength, $\sigma_{tpb}$ (MPa)	Tensile strength, $\sigma_{tpbb}$ (MPa)
Residual Strength	Cohesion, $c_{rb}$ (MPa)	Cohesion, $c_{rbb}$ (MPa)
	Friction angle $\phi_{rb}$ ( $^{\circ}$ )	Friction angle $\phi_{rbb}$ ( $^{\circ}$ )
	Tensile strength, $\sigma_{trb}$ (MPa)	Tensile strength, $\sigma_{trbb}$ (MPa)
Deformation	Young's modulus, $E_b$ (GPa)	Normal Stiffness, $k_n$
	Poisson's ratio $\nu_b$	Shear Stiffness, $k_s$

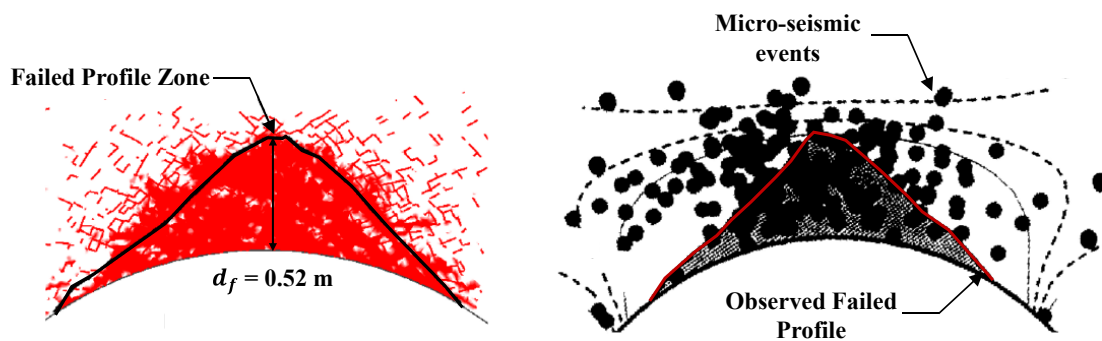
The method was first developed by calibrating the micro-properties to the UCS of an LdB sample, its Young's modulus, and its laboratory tensile strength. As there are 16 different micro-properties to calibrate, assumptions were made to avoid the non-uniqueness of the solution and aid in the calibration procedure. The list of assumptions for the calibration of the sample specimens is as follows (Sanipour et al., 2022):

- The Poisson's ratio of the blocks is taken from the laboratory test of the LdB granite.
- The  $E_b$  is the weighted average of Young's modulus of the minerals in LdB granite.
- The peak and residual friction angle for blocks and block boundaries is measured from the lab experiments of LdB granite.
- The peak tensile strength of the block boundaries is the same as the measured LdB granite.
- All residual tension and cohesion of the boundaries are assumed to be approximately 0.
- The joint stiffness ratio  $k_n/k_s$  is kept at 2.5.

The parameters are calibrated using these assumptions and an iterative process using a direct tensile test, a Brazilian test and a UCS test (Sanipour et al., 2022). Then, the properties found are applied using the same VTM scale to the MBE at the URL. The authors point out that at the tunnel scale, they are not trying to simulate individual grains with the VTM but to represent the general behaviour of grains and their boundaries. As found by previous research

(Martin, 1997; Hajiabdolmajid, 2002; Diederichs, 2007), when the strength of the VTM rock mass is calibrated to the laboratory's ultimate strength, no failure is simulated around the tunnel.

As no failure was found with the laboratory strength of the rock, Sanipour et al. (2022) calibrated the VTM to match the s-shape failure envelope suggested by Diederichs (2007), shown in Figure 2-9. Instead of directly modelling a complex tri-linear behaviour, they suggest using an equivalent Hoek-Brown failure envelope, as explained by Bewick et al. (2019). The same assumptions as before are used to calibrate. The process consists of first calibrating the UCS to the crack initiation stress of the LdB and matching the deformation found in laboratory tests. Then, confined compression tests are adjusted to match the confined strength of the equivalent Hoek-Brown by adjusting  $c_{rb}$  and  $\phi_{pb}$ . The results of the models are positive as both the depth and shape of failure were successfully modelled. Figure 2-16 shows the results compared to the MBE failure profile and the acoustic emissions (Sanipour et al. 2022). The model shows two types of failure: block failure and joint failure. The authors propose that the block failure presents spalling, and block boundary failure represents damage to the rock mass.



**Figure 2-16 Results of the simulation of the v-notch and EDZ at the MBE tunnel using the VTM method in RS2 compared to the field observations of failure and micro-seismic event measurements (modified from Sanipour et al., 2022)**

The VTM method presents the depth of failure, and, as seen in Figure 2-16, a representation of the EDZ is obtained (Sanipour et al., 2022). This representation of the EDZ is a characteristic that cannot often be simulated using continuum modelling methods. This can help determine the change in the hydrogeological characteristics of the rock mass after excavation. As a method to do back analysis on field observations, it can help to understand

the process of spalling further while still using simple 2D continuum-based numerical models. Its main drawbacks are its lack of use, significant calibration procedure, and extensive laboratory test results required for the input parameters. The process involves a lot of calibration, which is to be done on a sample with the same grain geometry as will be used in the excavation. Lastly, the assumptions require in-depth knowledge obtained from the physical experiments, such as  $E$  of each grain type and  $\phi_r$  of the laboratory sample.

### **2.3 DISCONTINUUM NUMERICAL METHODS**

Discontinuum numerical models and the Distinct-Element Method (DEM) were first introduced by Cundall (1971) as means to represent fractured and blocky rock. These types of methods generally allow for the displacement, rotation, and detachment of discrete bodies (Potyondy and Cundall, 2004). These bodies can interact with each other, meaning new contacts can be created, and forces are transmitted from their movements. It has been suggested to be effective in modelling granular materials such as rock masses (Cundal and Strack, 1979). This ability of the particles to detach makes it an excellent tool to model the EDZ. With its properties, mechanisms like the spalling process of the micro-fracturing away from the excavation can be explicitly modelled. This can help with understanding and designing DGRs. These methods improve upon the continuum approaches by allowing for more direct and less abstract representations of the EDZ. However, in DEM models, fractures can only occur at predefined fracture locations and cannot create new fractures, leaving room for improvement in the case of EDZ simulations.

#### **2.3.1 Bonded Tetrahedral Block Model Method**

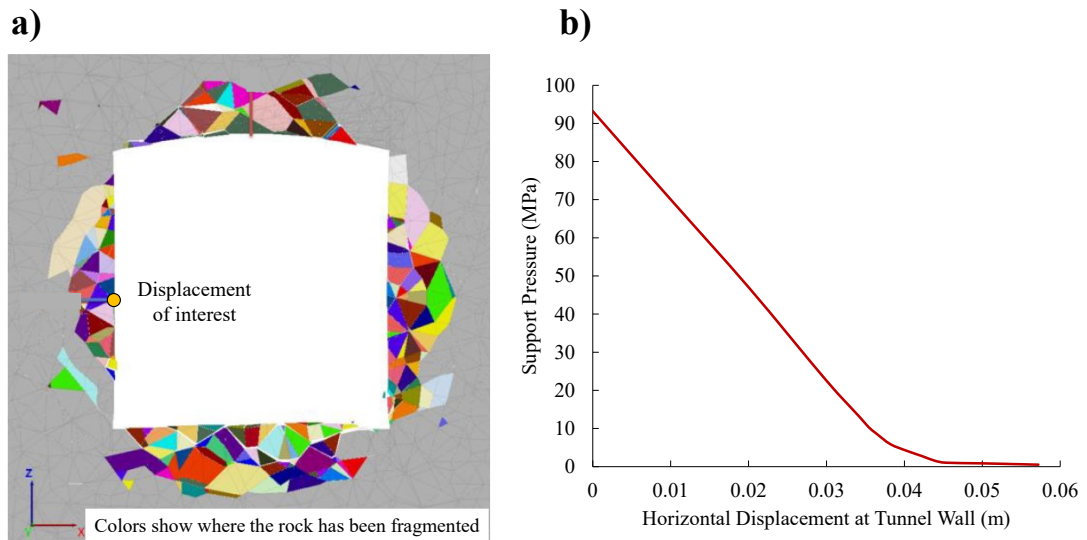
Garza-Cruz et al. (2014) suggested that a critical aspect of underground excavation design in brittle rock is the dilation of the rock. They state that for support design, the central mechanism that needs to be predicted is the displacement, similar to the suggestions by Kaiser et al. (2000). To determine dilation and displacement better, they propose a method using *3DEC* in which the rock mass is modelled as a series of tetrahedral bonded blocks. The use of tetrahedral is ideal as it simulates the initial zero porosity state of the rock mass. The tetrahedral blocks also create a heavily interlocked array that resists rotation even after bonds

are broken. These behaviours are crucial for rock mass performance at low confinement (Garza-Cruz et al., 2014).

The method proposed works under the principle that the strength and stability of underground excavation in brittle rocks is dominated by the creation and propagation of tensile fractures on the rockmass. Therefore, the strength of the rockmass is determined by the tensile and cohesive strength of the contacts. Garza-Cruz et al. (2014) suggested giving the tensile strength a random distribution found from laboratory testing. The cohesive strength is then set to 2.5 times the tensile strength following the  $\sigma_{UCS}/\sigma_t$  of 10-20 suggested by Diederichs (2007). The residual  $\sigma_t$  and  $\sigma_{UCS}$  are set to 0. The friction angle is set to the measured value by a triaxial test, with the peak being the same as the residual. The blocks are assumed to be elastic with  $E$  as measured from the unconfined compressive strength testing (Garza-Cruz et al., 2014).

They apply this method to a theoretical scenario. To investigate displacement, they applied the method to a 2.5D tunnel using the strength reduction method to simulate the effect of "supports" on the face. They used an arched back tunnel with a stress regime of  $\sigma_v = 31$  MPa,  $\sigma_H = 93$  MPa,  $\sigma_h = 50$  MPa, which suggests a high-stress scenario. The tunnel is excavated parallel to the  $\sigma_h$ . For detailed information on the rock mass's strength parameters, refer to Garza-Cruz et al. (2014). Figure 2-17a shows the spalling results with no support pressure. The Ground Reaction Curve (GRC) is shown in Figure 2-17b. This investigation signals two critical aspects of this method. The spalling depth is predicted by the fragmentation of the rock mass, i.e. the fracturing of the bonds. This  $d_f$  predicted is close to the expected  $d_f$  from the empirical observations by Martin et al. (1999). The GRC shows a very important mechanisms of this method; most of the deformation occurs after the support pressure decreases to less than 1 MPa (Garza-Cruz et al., 2014). Deformation is also heavily concentrated in the area immediately near the excavation, as the displacements are negligible 1 m away from the tunnel boundary. These two findings are key for effectively designing support systems in underground excavations in brittle rock (Garza-Cruz et al., 2014). The same method suggested by Garza-Cruz et al. (2014) was applied by Sinha and Walton (2021) for a granite pillar. Using the probabilistic tensile distribution, they replicated the failure

behaviour of a pillar in brittle rock. They could observe the failure as it spalls from the pillar boundary, creating the characteristic 'hourglass' shape (Sinha and Walton, 2021).



**Figure 2-17 a) Spalling results for a tunnel using the tetrahedral block model method in 3DEC (modified after Garza-Cruz et al., 2014) b) Displacement of the tunnel's left wall with respect of change in support pressure (modified after Garza-Cruz et al., 2014).**

The tetrahedral block model proposed by Garza-Cruz et al. (2014) is an excellent tool for modelling excavations in brittle rock where displacement is the main focus of the investigation. This method demonstrates not only the behaviours of spalling but also the bulking associated with it. When it comes to support design, this method, in conjunction with the support suggestions by Kaiser et al. (2000), allows for a level of precision that is seldom seen with other methods. When applying it, engineers must exercise care in selecting strength parameters, particularly the range of tensile strength expected in the field. This method has also been proven in multiple diverse situations, like the cave mine application (Garza-Cruz et al., 2014), pillar strength (Sinha and Walton, 2021), and laboratory samples (Sinha and Walton, 2020). The original authors do not give a detailed description of the strength selection or the calibration procedure. The tetrahedral block method is also computationally expensive as it is a DEM model.

### 2.3.2 The tetrahedral and Voronoi grain-based model method

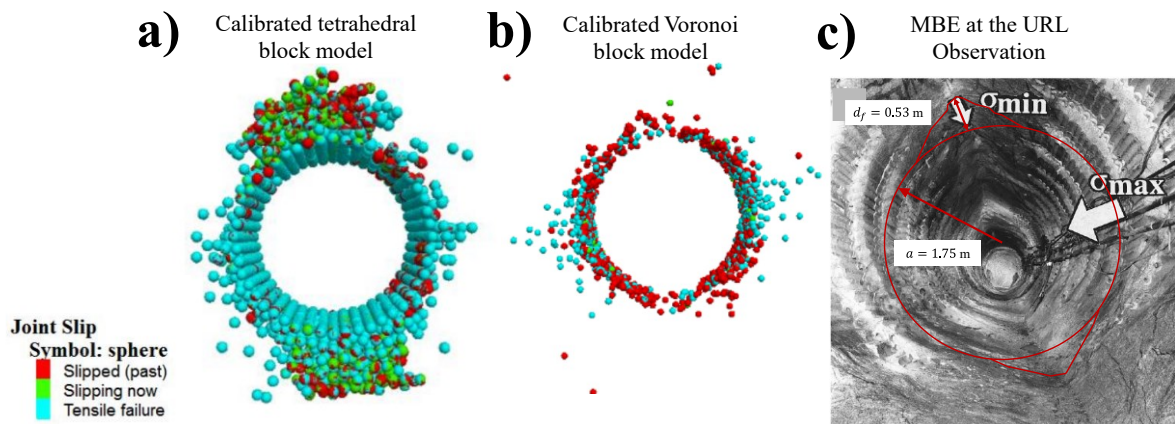
Azocar (2016) proposed to model excavation in brittle rock using tetrahedral or Voronoi blocks that simulate the grains near the excavation boundary using 3DEC. This method was

developed after the findings by Ghazvinian et al. (2014), where it was suggested that crystalline rock can be represented as a series of Voronoi blocks. The first step is to create a Voronoi or tetrahedral network to represent the excavation. Due to computational constraints, the blocks cannot be grain-sized and should be scaled up to achieve computational efficiency. The blocks are set to elastic, with the contacts as plastic. The contact strength follows a formulation similar to that of Hajiabdolmajid et al. (2002) for continuum models. Since it is a DEM method, the  $c_r$ ,  $\sigma_t$ , and  $\phi_i$  of the contacts are set to 0, representing the frictionless initial and cohesionless final states (Ghazvinian et al., 2014). The strength of the contact is calibrated to the macroproperties of the rock of interest using UCS, triaxial, and Brazilian tests. Azocar (2016) found that when applying to the excavation scale, the cohesion of the contacts needs to be reduced by 10 to 20%. They also found a significant difference between the results using tetrahedral or Voronoi blocks. They suggested that the tetrahedral method is more accurate for blocks with larger scales than Voronoi blocks. They suggest that if small enough blocks were used, the Voronoi blocks would be the most adequate, but the scale is impractical (Azocar, 2016).

Azocar (2014) applied the method to the MBE at the URL. As suggested by the method, they initially calibrated to the laboratory strength of the LdB with a UCS test, triaxial test, and a Brazilian test. They looked to match the crack damage strength. From this investigation, they obtained the parameters for Table 2-5. This strength is used in two different models for the MBE, one with tetrahedral blocks and one with Voronoi blocks. The results with the calibrated strength and the tetrahedral blocks yielded little to no failure around the excavation. Therefore, they performed a sensitivity analysis on strength parameters. To match the result of the MBE, a reduction of 14% to the  $c_p$  was needed in the case of the tetrahedral blocks. With this reduction, a match to the spalling failure at the MBE was found. The issue was the opposite for the Voronoi block model, as a sizeable tensile failure was found, and the contact tensile strength had to be doubled to match the MBE observations. The bond failure obtained from both models is shown in Figure 2-18.

**Table 2-5 Parameter selection for the strength of LdB granite using Voronoi and Tetrahedral Blocks for the grain-based model method (modified after Azocar, 2014)**

	Voronoi Block Model	Tetrahedral Block Model
Blocks Young's Modulus		100 GPa
Blocks Poisson's Ratio		0.29
Density		2700 kg/m <sup>3</sup>
Contact Peak Cohesion	80 MPa	130 MPa
Contact Tensile Strength	60 MPa	15 MPa
Contact Normal Stiffness	$9 \times 10^{13}$ Pa/m	$19 \times 10^{13}$ Pa/m
Contact Shear Stiffness	$1.8 \times 10^{13}$ Pa/m	$8 \times 10^{13}$ Pa/m
Contact Initial Friction Angle	0°	0°
Contact Mobilized Friction Angle	20°	20°



**Figure 2-18 Results of the simulation of the MBE at the URL in 3DEC with a) Tetrahedral grain-based block model (modified after Azocar, 2014) b) Voronoi grain-based block model (modified after Azocar, 2014) c) compared to the field observations of the field observation (modified after Martin, 1997)**

The tetrahedral and Voronoi block method in 3DEC can be applied to design by following the methodologies proposed by Ghazvinian et al. (2014) and Azocar (2016). This technique to represent brittle rock has been extensively investigated and can reproduce the results of laboratory experiments. When applying to the excavation scale, the user must be cautious about downscaling strength parameters. If the scaling is done correctly, the spalling zone can be determined, and insight into the EDZ can be obtained. This method can be reassessed with the newest version of 3DEC (V 9.0), which is computationally faster (Itasca, 2024). This could allow the Voronoi blocks to be significantly smaller, reducing the effects of scaling parameters from calibration to application.



### 2.3.3 The bonded-particle model method

Potyondy and Cundall (2004) suggested that rock can be represented by an array of cemented granular particles where the cement and the grains can break. They developed the bonded-particle model (BPM) for rock to prove this. The advantage of this representation of rock is that it does not idealize rock behaviour the way a continuum model does; instead, it represents it as a series of structural units that interact at contact points. The formulation of this method works under the following assumptions:

1. Particles are circular/spherical rigid bodies with finite mass.
2. Particles can be rotated and translated independently from each other.
3. Particle interactions are limited to the contact, and since they are spherical, contact only occurs between two particles.
4. Particles are allowed to overlap in small regions compared to the particle size.
5. Bonds of finite stiffness can exist between particles. They can carry load and break.
6. Force-displacement laws at each contact create the interaction between particles.

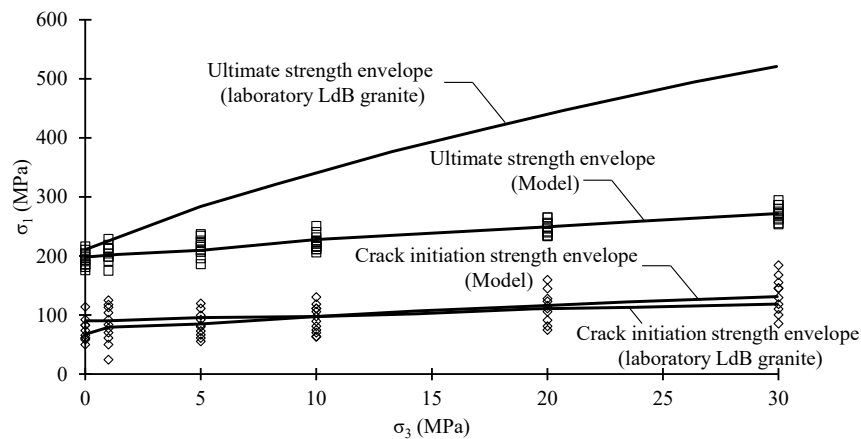
Further explanation of the implementation of such assumptions in *PFC2D* and *PFC3D* can be found in Potyondy and Cundall (2004). The cement bond is simulated as a parallel bond between particles. These parallel bonds resist the shear force, normal force, and the bending moment between two particles. To fully characterize the rock strength using these models, 10 parameters are required, 4 of which characterize the particles and 6 for the bonds. The parameters for the particles are:  $E_c$  (Young's modulus),  $k_n$  (normal stiffness)  $k_s$  (shear stiffness), and  $\mu$  (grain to grain contact friction coefficient). The parameters for the bond are:  $\bar{\lambda}$  (multiplier to set the bonds radii),  $\bar{E}_c$  (bond's Young's modulus),  $\bar{k}_n$  (bond's normal stiffness),  $\bar{k}_s$  (bond's shear stiffness),  $\bar{\sigma}_c$  (bond's tensile strength), and  $\bar{\tau}_c$  (bond's shear strength). A bond is broken once the shear or tensile strength is reached by the stresses in the bonds (Potyondy and Cundall, 2004).

Potyondy and Cundall (2004) simulated the MBE at the URL. First, they suggest selecting microproperties to match what is expected for the LdB granite. The microproperties are not outcomes of laboratory tests, so they make some assumptions. The  $E_c$  is assumed the same as the lab experiments. The strength of the bonds (both shear and tensile) is set to be normally distributed throughout the sample, with the mean being the  $\sigma_{UCS}$  and the standard

deviation to be such that the  $\sigma_{ci}$  is one standard deviation from the mean. The  $k_n$  and  $k_s$  are selected to match the Poisson's ratio from the lab. For further explanation of the assumptions, refer to Potyondy and Cundall (2004). Using these microproperties, biaxial and Brazilian tests were simulated. This simulated test aims to calibrate the microproperties to match the macroproperties of LdB. They found that the microproperties could be matched to the  $\sigma_{UCS}$  and to the crack initiation strength envelope. However, the friction angle of the ultimate strength envelope, the cohesion and the tensile strength were not matched (Potyondy and Cundall, 2004). Table 2-6 details the results of the macroproperties obtained from the LdB granite and the PFC2D and PFC3D BPM investigations. Figure 2-19 shows the strength envelopes after calibration.

**Table 2-6 Parameters for LdB granite from laboratory experiments and bonded block particle method in PFC2D and PFC3D (modified after Potyondy and Cundall, 2004)**

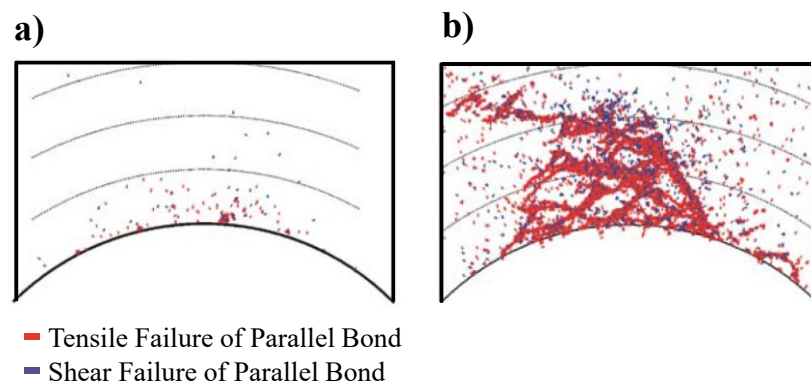
Property	LdB granite	<i>PFC2D</i> model	<i>PFC3D</i> model
$E$ (GPa)	$69 \pm 5.8$	$70.9 \pm 0.9$	$69.2 \pm 0.8$
$\nu$	$0.26 \pm 0.004$	$0.237 \pm 0.011$	$0.256 \pm 0.014$
$\sigma_{UCS}$ (MPa)	$200 \pm 22$	$199.1 \pm 13.0$	$198.8 \pm 7.2$
$\sigma_{ci}$ (MPa)	$90 + \sigma_3$	$71.8 \pm 21.8$ ( $\sigma_3 = 0.1$ )	$86.6 \pm 11.0$ ( $\sigma_3 = 0.1$ )
$\phi$ (°)	59	$29.5 \pm 4.8$	$32.1 \pm 2.4$
$c$ (MPa)	30	$58.5 \pm 8.5$	$55.1 \pm 4.2$
$\sigma_t$ (MPa)	$9.3 \pm 1.3$	$44.7 \pm 3.3$	$27.8 \pm 3.8$



**Figure 2-19 Crack initiation strength envelopes and Ultimate strength envelopes for LdB granite for laboratory tests and PFC simulations with the bonded-block particle method (modified after Potyondy and Cundall, 2004)**

Since the  $\sigma_{ci}$  strength envelope was accurately matched, they applied the calibrated material to the MBE at the URL scenario. To save on computational cost, the model is run as

a coupled *PFC-FLAC* model, where the expected failure location was simulated with the DEM and the rest is an elastic *FLAC* model (Potyondy and Cundall, 2004). When using the calibrated strength of the LdB granite, no failure was observed in the notch area (Figure 2-20a). To match closer to the MBE field observations, the bonds' strength was reduced by a factor of 0.5. The results of the strength reduction factor changes can be seen in Figure 2-20b. The failure mechanism resembles the field observations where the fractures propagate parallel to the excavation boundary and thin sheets of rock. The authors also point out the effect of the particle size selection even at the same damage factors. With small particle sizes, more failure is encountered. The results also show the failure of bonds not interconnected to the spalling area. With this observation, further analysis of all the zones of the EDZ can be made, including the potential change in the hydrological conditions of the rock.



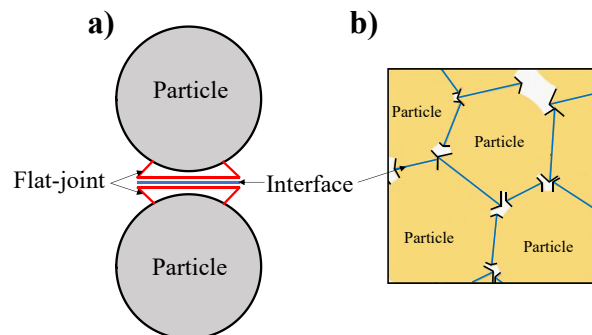
**Figure 2-20 Modelling results of the MBE tunnel using the bonded-block model method using PFC with a) original bond strength and b) reduced bond strength by a factor of 0.5 (modified after Potyondy and Cundall, 2004)**

The BPM method for EDZ modelling can replicate the field observations from the MBE at the URL. It also explicitly represents the spalling mechanisms by allowing the rock to break and fracture at the bond locations. Potyondy and Cundall (2004) provided a methodology that could be replicated, including the initial selection of micromechanical parameters and the calibration of the micromechanical behaviour of the rock. Theoretically, if enough laboratory data is acquired, the BPM model can be calibrated for initial strength estimates for underground excavation brittle failure. However, the bond strength has to be reduced by 50% to match the results. This adds uncertainty to the design, as there is no accurate indication of an adequate strength reduction factor. The BPM method can be better

applied for the back analysis of field observations where the strength reduction factor is calibrated to match the observations.

### 2.3.4 The flat-jointed material method

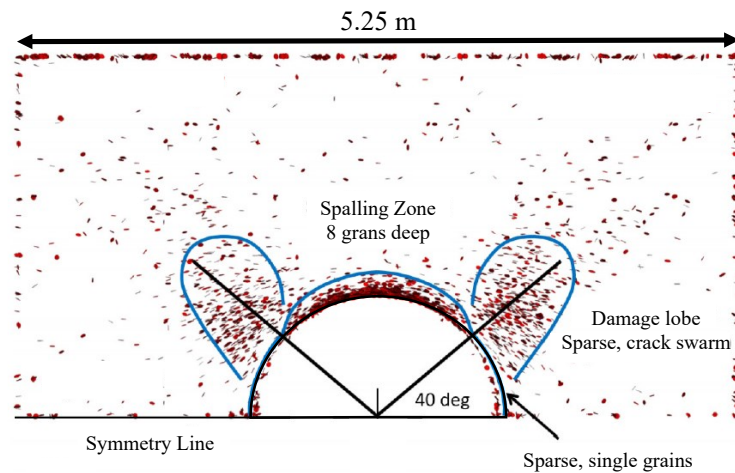
To improve on the BPM method, a new material model was proposed and introduced in *PFC2D* and *PFC3D* (Potyondy, 2015). This new material model is the flat-jointed material. This material model creates bonds between rigid particles that have a finite size (Itasca, 2019). The bond between particles is a flat interface which interacts along the interface of the connecting flat-joints. Figure 2-21a shows the representation of flat-jointed bonds in *PFC2D*. This material model allows for the simulation of angular and interlocked grains, which are more similar to the microstructure of crystalline rock (Potyondy, 2015). Figure 2-21b represents this crystalline structure using the flat-jointed material model in *PFC2D*. Another difference from the BPM is that rather than having bonds disappear once they break, the flat-jointed model allows for a residual strength of the bond (Itasca, 2019). The micromechanical parameters are very similar to the BPM; however, instead of having a shear strength, the bond strength is determined by cohesion and friction, with corresponding residual strength components. All other elastic and particle parameters remain as in BPM (Itasca, 2019). This type of structure can help accurately represent brittle failure in underground excavations.



**Figure 2-21 Theory of the arrangement of particles and bonds for the flat-joint method for a) two particles b) crystalline arrangement of particles in *PFC2D* (modified after Potyondy, 2015).**

Potyondy and Mas Ivars (2020) suggested that this material model can simulate brittle failure around underground excavations. Similarly to the BPM, they calibrated the micromechanical parameters to match the macromechanical behaviour of the laboratory

tests. They made use of the Aspo Diorite granite for their investigation. They were able to match the  $E$ ,  $\sigma_{UCS}$ ,  $\sigma_t$ , and the strength at 7 MPa confinement. However, the crack initiation stress, crack damage stress, and Poisson's ratio were not matched. They used the properties to simulate failure to conditions similar to the Aspo Pillar Stability Experiment. They successfully presented a spalling zone that corresponds to the expected borehole damage. They also show zones with sparse damage, but failure is not interconnected (Potyondy and Mas Ivars, 2020). This is an initial indication of the method's ability to categorize the entire EDZ. Figure 2-22 shows the cracks obtained from an excavation.



**Figure 2-22 Simulation results of the Aspo experiment with the flat-jointed material method showing the spalling zone and the EDZ (modified after Potyondy and Mas Ivars, 2020).**

The flat-jointed method is relatively recent and has not been explored fully. It shows a good indication that it can present spalling in brittle rock. While there are no detailed guidelines on calibrating the model's micromechanical properties, the process suggested is similar to the one detailed by Potyondy and Cundall (2004). If the model is correctly calibrated, it can simulate not only the  $d_f$  but it can also characterize the entire EDZ profile. This method requires more investigation and application to other case scenarios before it can be confidently used for design.

## 2.4 HYBRID FINITE-DISCRETE NUMERICAL METHODS

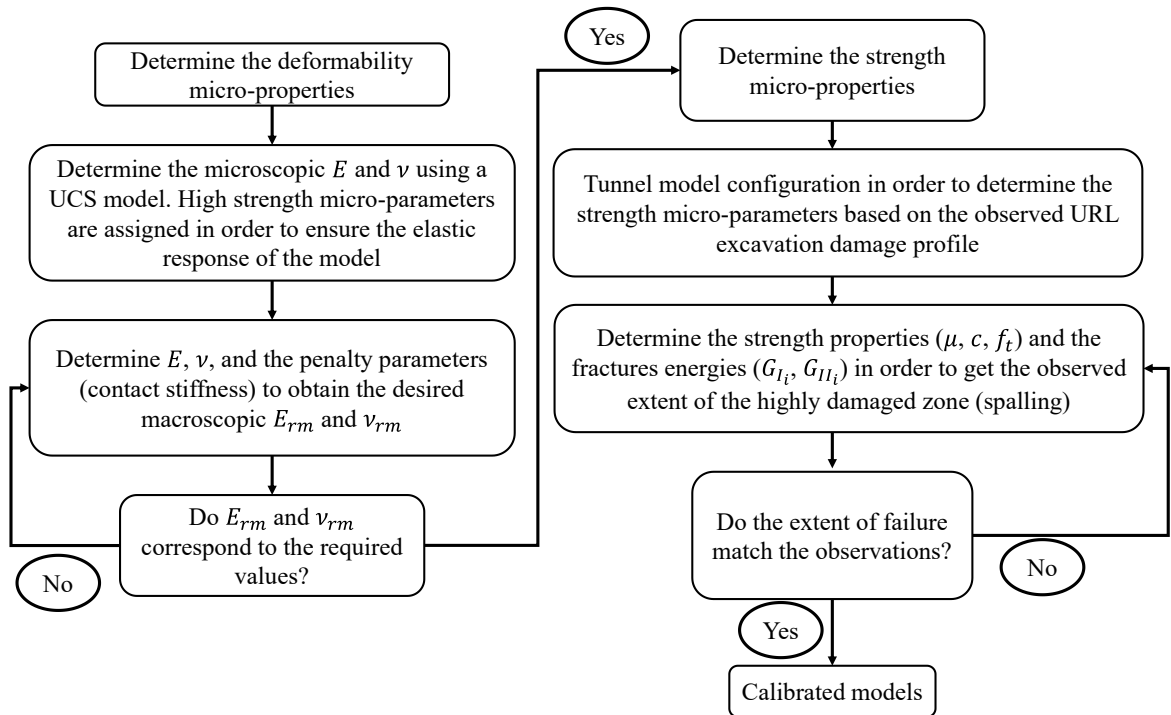
One of the main issues with simulating the failure of brittle rock around underground excavations is being able to reproduce the mechanism of fracturing of a continuum material

such as rock. Both continuum and discontinuum numerical modelling approaches have problems that prevent them from fully capturing the mechanisms of spalling. Continuum numerical models cannot explicitly simulate this process as the continuum cannot fracture, while discontinuum numerical models can only reproduce fracturing along predetermined discontinuities (Lisjak and Grasselli, 2014). To solve these two issues, the combined Finite-Discrete Element Method (FDEM) was devised (Munjiza, 2004). This type of numerical model starts with a continuum to which the equations of motion are applied (Lisjak and Grasselli, 2014). Discontinuities are allowed to occur in this continuum field if the forces exceed a fracture criterion. The fracture criterion specifics are code-dependent; however, they generally follow the fracture modes and associated fracture energies in compressive fields as proposed by Griffiths crack theories (Atkinson, 1987). Once discontinuities have formed, the models can deal with the new discrete bodies by introducing contact interaction between them (Lisjak and Grasselli, 2014). Some of the most prominent commercially available software for FDEM are IRAZU by Geomechanica (Gemoechanica, 2017) and ELFEN by Rockfield Software (Rockfield Software, 2024). For further detail on the models, the reader is encouraged to read Lisjak and Grasselli (2014), Tatone and Grasselli (2015), and Munjuza (2004).

#### **2.4.1 Mechanical Analysis and Interpretation of EDZ using IRAZU**

Thanks to its capacity to generate fractures in a continuum method, FDEM models have been used to simulate brittle failure of rock around underground excavations. Vazaios et al. (2017) proposed and explained one method to do so. They used the FDEM software IRAZU to simulate the failure observed at the MBE URL. To model brittle failure around underground excavations, they start by calibrating a UCS model to match the expected strength and elastic response of a sample of the rock of interest. The parameters to calibrate are the penalties (contact stiffnesses), friction coefficient, cohesion, tensile strength, and fracture energies (Mode I and Mode II). The same values are applied to the tunnel scale once calibrated to the desired strength and elastic properties. A key factor is to use a mesh small enough to avoid any mesh dependence for the fracture pattern. In turn, this means that the fractures are somewhat geometry dependent, and can only occur at element boundaries. The mesh must also be consistent between the sample test and the field simulation. Before excavating the

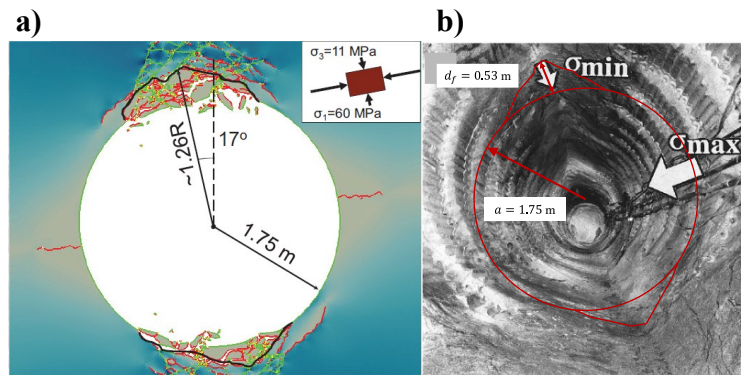
tunnel in the model, the stresses are input into the model as a continuum (FDEM), as no fractures are expected to occur prior to excavation. The tunnel is excavated, and the model is run until the excavation reaches static condition (Vazaios et al., 2017). The strength parameters must be further calibrated to achieve the fracturing encountered in the field. For the MBE at the URL case scenario, Vazaios et al. (2017) calibrated the uniaxial strength of the sample to the  $\sigma_{ci}$  of LdB granite. This calibration to the crack initiation is consistent with other methods found in the literature (Martin, 1997; Hajiabdolmajid et al., 2002; Diederichs, 2007). The tunnel excavation process is repeated until a good match is found with the field observations. The process detailed by Vazaios et al. (2017) is demonstrated using the flow chart from Figure 2-23.



**Figure 2-23 Methodology for the calibration of micro-mechanical properties for excavations in brittle rock modelling in IRAZU (modified after Vazaios et al., 2017)**

This hybrid methodology achieves, in the case study, a good match to field observations. Furthermore, the mechanisms of failure and extent of the HDZ are demonstrated in a way that other methods fail to do. Thanks to the capabilities of FDEM to create new fractures in the continuum matrix, the extent of failure outside of the HDZ is shown. The EDZ is visualized using this method. The extent of the EDZ and the density of the fractures within are direct results of this method. The study by Vazaios et al. (2017) matches the URL HDZ

and the acoustic emissions measured during this experiment. The results can be seen in Figure 2-24. While positive results are highlighted from this method, there are some issues, particularly regarding its use in the design and forward predictions of EDZ. The methodology proposed by Vazaios et al. (2017) requires the calibration of the mechanical properties of the model to match field observations. There are no guidelines for calibrating the mechanical properties if no spalling is observed. They suggest that the  $\sigma_{ci}$  is a good indicator of the ultimate strength of the rock in situ. Further, the calibration of the stiffness and strength of the material involves approximately 10 different parameters, increasing the non-uniqueness of the solution. This method also requires a deep understanding of fracture mechanics, particularly fracture energies and stiffness.



**Figure 2-24 a) Results of the modelling of the MBE at the URL using *IRAZU* after micromechanical calibration (modified after Vazaios et al., 2017) compared to b) fields observations of v-notch formation at the MBE (modified after Martin, 1997)**

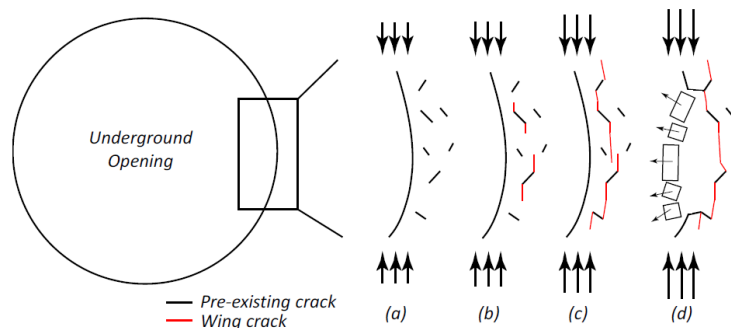
#### 2.4.2 Spalling Depth Prediction Using *ELFEN* Hybrid Code.

The FDEM software *ELFEN* by Rockfield (2024) was introduced as a method to model fracture initiation and propagation in solids following the proposed numerical techniques by Munjiza et al. (1995). It has been developed to investigate the failure mechanism of rock from its combined compressive and tensile response. It works by having a continuum domain governed by a Mohr-Coulomb strength envelope with fracture mechanics implementation (Klerck et al. 2004). The intact rock is simulated as a continuum with certain strength parameters and a crack criterion  $G_f$ . If the crack criterion is met, a crack is created, changing the model to a DEM (Cai and Kaiser, 2004). The main upside of this software compared to other FDEMs is that fractures are allowed to propagate seamlessly throughout the continuum mesh. Fractures can cut through existing mesh elements thanks to an intra-element fracturing

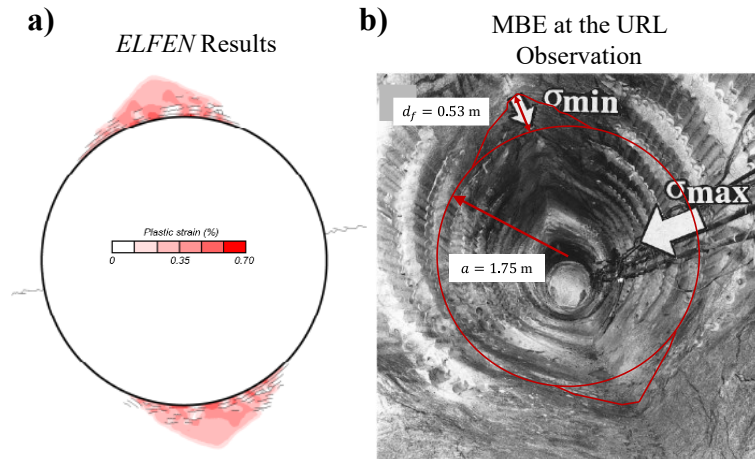


algorithm (Klerck et al. 2004). Thanks to these unique capabilities, it is optimal for EDZ modelling.

The modelling software *ELFEN* has been used to model spalling in underground excavations. It was applied by Hamdi et al. (2017) to simulate the V-notch failure at the MBE. They did so by applying the laboratory strength of LdB granite but having initial fractures around the underground excavation to simulate the heterogeneity of the rock. The justification for this is that spalling occurs from the propagation of defects and microfractures (Hamdi et al., 2017). The initiation of the spalling phenomenon due to these microcracks/defects is shown in Figure 2-25. The model is implemented by creating a Gaussian-distributed set of initial fractures using a DFN algorithm. The fractures themselves are on average 10 cm long with random orientation with no cohesion and  $\phi$  of  $25^\circ$ . The strength of the rock mass is assumed to be the laboratory strength ( $\sigma_{UCS} \approx 213$  MPa). The results showed good agreement with the stress initiation threshold. Failure started to occur at 105 MPa in the tangential direction of the excavation (Hamdi et al., 2017). The depth of plastic deformation of the continuum reached a similar depth as the failure in the MBE. However, the fracture propagation did not reach the expected  $d_f$  (Hamdi et al., 2017). The results of the *ELFEN* models after static equilibrium was reached are shown in Figure 2-26a.



**Figure 2-25 Initiation of spalling near an excavation due to fracture interaction of pre-existing defects in the rock mass (after Hamdi et al., 2017)**



**Figure 2-26 a) Results of the MBE modelling using calibrated values in *ELFEN* showing plastic strain and fracturing (modified after Hamdi et al., 2017) compared to b) fields observations of v-notch formation at the MBE (modified after Martin, 1997)**

By looking at the plastic strain of the continuum the  $d_f$  of the MBE was adequately estimated. *ELFEN* appears to be suitable for the design of *underground* excavations in brittle rock. Unlike other methods, the *ELFEN* method described by Hamdi et al. (2017) does not require a reduction of the strength of the rock to fit the crack initiation. The introduction of a DFN simulation heterogeneity in the rock achieves the reduction of the strength. Another issue is that the spalling depth was not achieved with the fracture propagation of the model, which is what would be expected from the field observations. Lastly, the method suggested only explores the HDZ and cannot predict the behaviour of the entirety of the EDZ. The investigation has only been done once; with further refinement, it might be able to serve as a better tool with more accurate results.

### **2.4.3 Imperial College Geomechanics Toolkit Finite Element-Based Discrete Fracture Growth**

Saceanu et al. (2022) proposed a hybrid Finite-Discrete element method to simulate the generation and evolution of EDZ. This method uses the Imperial College Geomechanics Toolkit to create a numerical modelling environment that is not constrained by the mesh size and fracture propagation and can occur freely through the continuum. It uses fracture mechanics concepts to determine if the fracture energy was exceeded, then a fracture is created, and a meshing algorithm that re-meshes the continuum once a fracture has been created. For details on the fracturing extension, discretization, and remeshing of the

continuum, the reader is encouraged to read Saceanu et al. (2022). An initial set of disks with a given size or size distribution needs to be introduced to the model. These initial disks are where the fractures can initiate and propagate. As such, the disk quantity and size must be calibrated to use the method.

Spalling forms in this method once the propagated fractures intersect the excavation boundary. The buckling mechanism after failure is not explicitly simulated, and the detached pieces are ignored after the complete intersection of the fracture. The propagation of fractures affects the  $E$  of the rock mass, with a minimum of 10 Pa for entirely loose rock. This degradation is given by Mazar's (1984) damage model, which decreases  $E$  by (Saceanu et al., 2022):

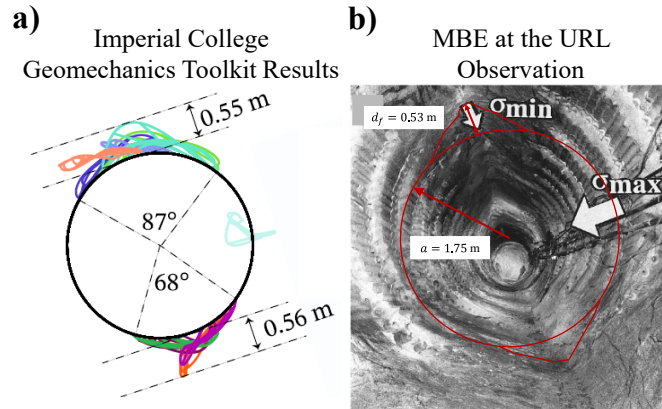
$$\tilde{E} = E(1 - d) \quad (2-21)$$

where  $\tilde{E}$  is the damaged Young's modulus,  $E$  is the Young's modulus, and  $d$  is the damage variable given by:

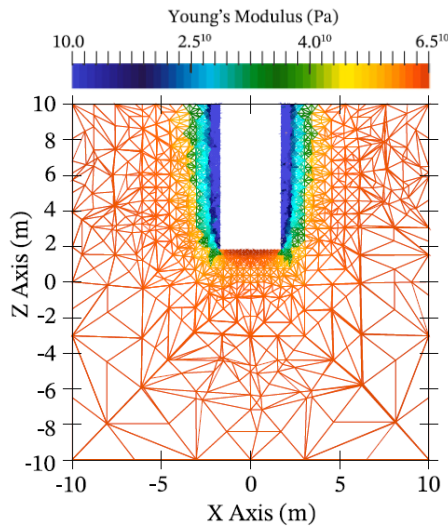
$$d = \alpha_t d_t + \alpha_c d_c \quad (2-22)$$

where the  $\alpha_t$  and  $\alpha_c$  account for the tensile and compressive states. These values are dependent on Mazar's damage material parameters  $A_t$ ,  $B_t$ ,  $A_c$ , and  $B_c$  which are material-dependent. These material parameters need to be calibrated for the EDZ simulation. Fracture growth is dependent on the critical stress intensity factor for Mode I fractures ( $K_{IC}$ ). It is the energy required in the continuum to propagate the generated fracture. The Mazar's damage parameters and the  $K_{IC}$  are the parameters required for the strength and evolution of fractures. The parameters necessary for the strength of the rock mass are the density, Young's modulus, Poisson's ratio,  $\sigma_{UCS}$ , and  $\sigma_t$  (Saceanu et al., 2022).

Saceanu et al. (2022) used the MBE at the URL to validate the method. By calibrating the material parameters and the initial number of disks, they obtained a match to the spalling depth. Figure 2-27 shows the results for the MBE URL using the Imperial College Geomechanics Toolkit after calibration. They also demonstrated the loss of  $E$  due to the propagation of fractures and the damage generated in the rock mass. Figure 2-28 shows the change in  $E$  once the fractures produce spalling. Once the method was validated it was then used to predict failure for the deposition tunnels at the DGR proposed in Forsmark, Sweden (Saceanu et al., 2022).



**Figure 2-27 a) Results of the MBE modelling using calibrated values with the Imperial College Geomechanics Toolkit method showing fractures that have developed into a v-notch (modified after Saceanu et al., 2022) compared to b) fields observations of v-notch formation at the MBE (modified after Martin, 1997)**



**Figure 2-28 Change in Young's modulus due to fracture formation near an excavation in the Imperial College Geomechanics Toolkit (modified after Saceanu et al., 2022)**

During the investigation into the deposition tunnels, Saceanu et al. (2022) looked at the relationship between fracture propagation and different possible scenarios. Some of the hypotheticals of interest were the direction of the principal stresses with respect to the deposition tunnel, the distance between deposition tunnels, the initial amount of disks, and the geometry of the deposition tunnel. This application shows the potential of spalling at the Forsmark site and advises on the possible effect of the fractures on the transportation of radionuclides into the rock mass (Saceanu et al., 2022).

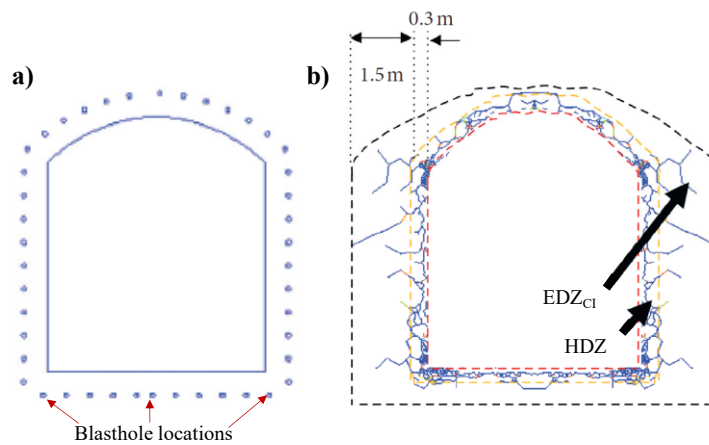
The Imperial College Geomechanics Toolkit was successfully used to simulate the failure of brittle rock around the MBE at the URL and for the possible configurations at Forsmark. The process of spalling can be realistically modelled using this hybrid approach. A great benefit over other methods is twofold. In the first place, it is an explicit simulation of the fracturing process and spalling. The second one is that it re-meshes the continuum as new fractures are produced, making it mesh size-independent. There is no guidance on using the method or the appropriate strength and fracture parameters. Mazar's damage parameters are rock-type dependent and can be found in the literature. Yet their use and physical meaning are abstract concepts that might hinder the use of this method. The initial amount of disk is another factor that needs to be calibrated and might cause differences in the results. While the method is independent of mesh size, it trades it for dependence on the amount of initial disks, their sizes, and distributions. More investigation on parameter sensitivity and selection is still needed to effectively use the Imperial College Geomechanics Toolkit method.

#### **2.4.4 Blast-Induced EDZ Modelling Method with FDEM**

An et al. (2020) developed a method to predict the EDZ formation around underground excavations that accounts for the damage generated by blasting. They use a hybrid FDEM, which allows the continuum to fracture along the mesh boundaries if the fracture criteria are met. This fracture criterion is similar to others in that it accounts for energy and two different fracturing modes. Mode I involves tensile fracturing and is dominated by the tensile fracture energy  $G_{fI}$ . Mode II is the shear fracturing or sliding controlled by the shear fracture energy  $G_{fII}$ . The generated fractures can only occur along mesh boundaries, and there is no intra-mesh fracturing. Due to the nature of blasting, the models are explicit, accounting for the time steps required to transmit the blasting energy. Fully coupled interactions between the gas fluid flow, the thermal changes, and the mechanical strength of the rock are also modelled using this method. An in-depth explanation of the coupling can be found in An et al. (2020).

The authors of this method detail the calibration process for its effective use (An et al., 2020). The required parameters to use this method are  $E$ ,  $\nu$ ,  $\rho$ ,  $\sigma_t$ ,  $\sigma_{UCS}$ ,  $\phi$ , the surface friction coefficient ( $\mu$ ) (the friction of the generated fractures), and the fracture energies  $G_{fI}$  and  $G_{fII}$ . They applied their method to a top-heading tunnel in Aspo Diorite. The rock mass strength and the fracture energies were calibrated using UCS and Brazilian tests simulated in the

model. First the  $\sigma_{UCS}$  of the laboratory, the specimen was matched by simulating a UCS test. They were mainly concerned about matching the strength of the rock and the fracture initiation and pattern. Then, a Brazilian test was performed to match the laboratory observation. With this investigation, they calibrated  $\sigma_t$  and the  $G_{fI}$ . Once calibrated to the desired strength, the rock mass parameters were applied to the tunnel. They modelled it by simulating only the line blasting, not accounting for the entire blast. Their results showed a good representation of the HDZ and the entire EDZ. Figure 2-29 shows the line drilling and the blasthole locations and the final EDZ characterization after equilibrium is reached.



**Figure 2-29 a) Blasthole location to simulate line blasting for the use of the blast-induced EDZ modelling method b) results of the implementation of the blast-induced EDZ modelling method showing the HDZ location and depth and the EDZ<sub>C1</sub> location and depth (modified after An et al., 2020).**

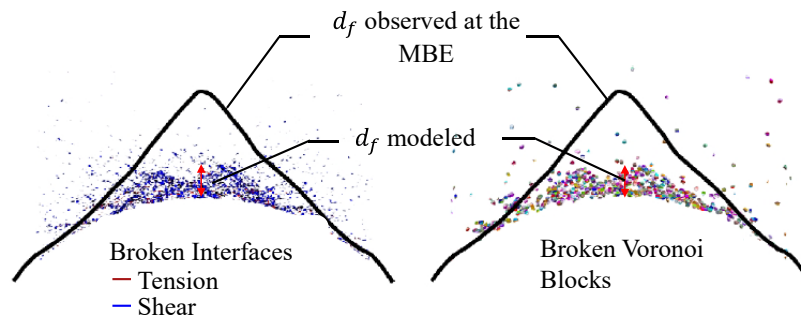
The method proposed by An et al. (2020) serves as a tool seldom investigated in literature. Blasting significantly affects the EDZ, and it is a common construction method in tunnelling (Hoek, 2002); however, it is often neglected in the investigation. The blasting-induced EDZ method gives a reasonable methodology and results that engineers can follow if blasting damage is a concern. The method also allows for the interpretation and estimation of the outer zones of the EDZ and not only the HDZ or spalling. Knowing the extent of the fractures can help estimate the radionuclide transports in the DGR. It allows for an initial estimation of the long-term strength of the rock. The process detailed by An et al. (2020) is repeatable and can be calibrated if sufficient laboratory data is available. The designer only needs access to UCS and Brazilian tests for the rock of interest to use it. The main issue of the method is its lack of accessibility. As described by the authors, the method is not commercially available

and would have to be programmed by the user if needed. This substantially increases its level of entry for rock practitioners. Another setback is its lack of use and validation.

#### **2.4.5 Subspring Network Breakable Voronoi Model**

This method is based on the Lattice/Discrete Element Model proposed by Rasmussen (2021) and Rasmussen (2022). The Subspring Network contact model with rigid, Breakable, Voronoi-shaped model (SNBV) was developed by Potyondy and Fu (2024). It is a hybrid method developed within *PFC3D*, to model brittle failure of rock in both the laboratory and field scale. The model was developed applying two different mechanisms. The first is the Lattice-like subspring networks which determine the behaviour of the bonds. It is a scheme similar to the bonded block method where the contact surface is defined by a set of springs that can break. The second part of the model is the capability of the Voronoi blocks to break. This behaviour is done by giving each block a failure threshold (Hoek-Brown in this case), and if the threshold is met, the block breaks into two new blocks. The microproperties required to describe the behaviour of the model are divided into four: deformability, microcrack fabric, interface strength, and grain strength. In total 17 different elastic and strength parameters are required for this method. For a detailed explanation, the reader should read Potyondy and Fu (2024) and Potyondy and Pruvance (2024).

This method was first applied to laboratory-scale rock (Potyondy and Pruvance, 2024). The characteristic stages of the unconfined compressive test proposed by Martin and Chandler (1994) were represented by this method. The stress-strain curves demonstrated the non-linearity at initial loading due to crack closure and the volumetric strain reversal at the crack damage stress (Potyondy and Fu, 2024). They also obtained the characteristic transition from brittle to perfectly plastic behaviour with increasing confining stress (Potyondy and Pruvance, 2024). They calibrated the microparameters to pink LdB granite to match the  $\sigma_{UCS}$ ,  $\sigma_{CI}$ ,  $\sigma_t$ , and  $E$ . Then they applied these calibrated parameters to the MBE at the URL. However, with their calibrated microparameters the strength depth of failure was underestimated (Figure 2-30). This method is quite novel and still needs to be refined to determine if it can adequately predict EDZ formation and behaviour.



**Figure 2-30 SNBV results for modelling the MBE in LdB granite after micromechanical properties calibration to laboratory experiments showing the broken interfaces (left) and broken Voronoi blocks (right) compared to the observer failure at the MBE (modified after Potyondy and Fu, 2024)**

## 2.5 SUMMARY

The methods to simulate brittle rock around underground excavations can be divided into four different general categories: empirical methods, continuum numerical modelling methods, discontinuum numerical modelling methods, and hybrid finite-discrete numerical modelling methods. Each of these categories has its advantages and disadvantages. There is no single superior method to predict EDZ behaviour. The method selection depends on the user's intended purpose and the level of detail they aim to achieve in their investigation. Each method's interpretation and calibration-level also vary substantially; therefore, different knowledge and expertise are required to use each method effectively. A simple summary of each method and its capabilities is shown in Table 2-7. It contains the method name, methods category, and software used for development. For a more in-depth summary of the method, the table shows the number of input strength parameters the original authors suggested for effective use. It also shows how effective each method is in determining HDZ and EDZ<sub>SI</sub> and how they define these zones.



**Table 2-7 Summary of methods to simulate EDZ around underground excavation in brittle rock.**

Approach	Method Category	Software used for development	Strength parameters required	HDZ	HDZ interpretation	$d_f$	Shape of failure	EDZ <sub>SI</sub>	EDZ <sub>SI</sub> interpretation	References
Depth of failure Equation	Empirical	NA	1	Yes	Equation	Yes	No	No	NA	Martin et al (1999), Diederichs et al (2010)
Empirical equations of EDZ prediction	Empirical	<i>Phase2/RS2</i>	3	Yes	Equation	Yes	No	Yes	Equation	Perras and Diederichs (2016)
Hoek-Brown Brittle Parameters	Continuum	<i>Phase2/RS2</i>	3	Yes	Factor of Safety	Yes	No	No	NA	Martin (1995)
Cohesion Weakening Friction Strengthening (CWFS)	Continuum	<i>FLAC</i>	7	Yes	Failed Elements	Yes	Yes	No	NA	Martin et al. (1999) Hajiabdolmajid (2001), Hajiabdolmajid et al. (2002) Hajiabdolmajid et al. (2003), Walton (2019)
CWFS with modified critical strain parameters	Continuum	<i>FLAC</i>	6	Yes	Failed Elements Maximum Shear Strain	Yes	Yes	No	NA	Renani and Martin (2018) Eldelboro (2009) Eldelboro (2010)
Instantaneous CWFS Damage Initiation	Continuum	<i>Phase2/RS2</i>	5	Yes	Failed Elements	Yes	Yes	No	NA	Eldelboro (2010)
Spalling Limit (DISL) As-built geometry	Continuum	<i>Phase2/RS2</i>	7	Yes	Failed Elements	Yes	Yes	No	NA	Diederichs (2007)
DISL EDZ interpretation with DISL	Continuum	<i>Phase2/RS2</i>	7	Yes	Confining Stress	Yes	No	Yes	Failed Elements	Cai and Kaiser (2014) Perras and Diederichs (2016) Rinne et al (2004), Shen (2014)
FRACOD 2D Continuum-Based Voronoi Tessellated Models	Continuum	<i>FRACOD</i>	5	Yes	Fracture Interaction	Yes	Yes	Yes	Fracture Initiation	Barton and Shen (2017)
Bonded Tetrahedral Block Model	Discontinuum	<i>RS2</i>	16	Yes	Failed Elements/Blocks Block	Yes	Yes	Yes	Joint Failure	Sanipour (2022)
Tetrahedral Grain-Based Model	Discontinuum	<i>3DEC</i>	9	Yes	Detachment Bonded Block Failure	Yes	No	Yes	Bond Failure	Garza-Cruz et al. (2014)
Voronoi Grain-Based Model	Discontinuum	<i>3DEC</i>	9	Yes	Failure	Yes	Yes	No	NA	Azocar (2014)
Bonded-Particle Model	Discontinuum	<i>3DEC</i>	9	No	NA	No	No	No	NA	Azocar (2014)
					Parallel Bond Failure	No	No	No	Low-Density Parallel Bond Failure	Potyondy and Cundall (2004)
		<i>PFC2D/PFC3D</i>	7	Yes		Yes	Yes	Yes		

Flat Jointed Material Model	Discontinuum	<i>PFC2D/PFC3D</i>	9	Yes	Flat-Joint Failure	Yes	Yes	Yes	Low-Density Flat-Joint Failure	Potyondy (2015) Potyondy and Mas Ivars (2020)
EDZ Interpretation with IRAZU	Hybrid		7	Yes	Rock Detachment	Yes	Yes	Yes	Fracture Initiation	Vazaios et al. (2017)
Spalling Depth Prediction with ELFEN	Finite/Discrete	<i>ELFEN</i>	9	Yes	Plastic Strain Fracture	Yes	Yes	No	NA	Hamdi et al. (2017)
Imperial College Geomechanics Toolkit	Hybrid	Imperial College Geomechanics Toolkit	10	Yes	Interaction with Excavation Boundary	Yes	Yes	No	NA	Saceanu et al. (2022)
Blast-Induced EDZ Model	Finite/Discrete	Open Source <i>Y2D</i>	9	Yes	Fracture Interaction	Yes	No	Yes	Fracture Initiation	An et al. (2020)
Subspring Network Breakable Voronoi Model	Hybrid		17	Yes	Bond and block breakage	No	No	No	NA	Potyondy and Fu (2024) Potyondy and Pruvance (2024)

It has been shown that many different methods are proposed to simulate brittle failure around underground excavations and EDZ characterization. The list provided in this chapter is not comprehensive, and methods are constantly being developed, proposed and updated. However, the methods shown here are extensive and can help rock mechanics engineers as a starting point for selecting an adequate method. The reader is encouraged to read the references to get the details for each particular method.

# **CHAPTER 3 - A SENSITIVITY STUDY AND ROBUSTNESS EVALUATION OF THE CWFS AND DISL APPROACHES FOR BRITTLE FAILURE CONTINUUM MODELLING AROUND UNDERGROUND EXCAVATIONS**

L.F. Gomez, A.G. Corkum, N. Bahrani, D. Mas Ivars

Manuscript submitted to the Rock Mechanics Rock Engineering Journal. Status: Pending

## **3.1 ABSTRACT**

The numerical modelling of tunnels in brittle rock is a challenging endeavour for rock mechanics engineers. Multiple methods have been developed to aid in the design of underground excavations that are prone to brittle failure. The most useful of these, for rock mechanics practitioners, are the ones that adequately represent the ground reaction and can be interpreted without being an expert or a frontrunner in numerical modelling. With these goals in mind, continuum numerical models stand out amongst other methods. Two approaches that make use of continuum numerical modelling are the Cohesion Weakening Friction Strengthening (CWFS) and the Damage Initiation Spalling Limit (DISL). Both have been developed to deal with the same issue of brittle rock failure in tunnelling. To test their robustness, a sensitivity analysis of the strength parameters was conducted. Then, they were applied to multiple fictitious stress scenarios to test their capability of reproducing empirical observations of depth of failure. The present investigation shows that the CWFS approach is a robust approach for modelling brittle failure around tunnels that can be easily applied and interpreted by rock mechanics practitioners. The sensitivity analysis on the CWFS gave a full understanding of the practical impact of input parameter selection. The DISL approach has been shown to require a fundamental understanding of numerical modelling for its effective interpretation.

Keywords: Brittle failure, tunnelling, continuum modelling, CWFS, DISL, FLAC.

### 3.2 INTRODUCTION

Spent nuclear fuel is often planned to be stored in Deep Geological Repositories (DGR) which are commonly designed to be built in competent rock with high strength and low permeability. There is a special interest in ensuring failure or damage of the rock is well understood to avoid the transport of nocive radionuclides into the environment (Ahn and Apted, 2010). As nuclear power becomes more common, the need for the construction of a DGR increases. Therefore, understanding and predicting the failure around tunnels in massive brittle rock is crucial for this purpose. Numerical modelling is frequently used for these predictions in rock mechanics, a successful numerical model balances the lack of data and the understanding of the underlying mechanisms to come up with a solution that is interpretable and useful for design (Starfield and Cundall, 1988). This holds to the modelling of brittle rock failure around underground excavations. Several approaches have been proposed to simulate these brittle failure scenarios. Some of them require a deep understanding of numerical models for both use and design interpretation. Such tools are more adequate for rock engineering modelling specialists who are at the leading edge of knowledge development in rock mechanics. This leaves the need for a tool to investigate brittle failure that rock engineering practitioners who have competence in rock mechanics and numerical modelling, if not cutting-edge expertise in numerical modelling. This type of approach can help not as a final design criteria, but as a means for field engineers to practically interpret results and act accordingly as construction progresses.

Assessing the behaviour of brittle rock in underground excavation has been an area of interest for many researchers. Theories on how to deal with such conditions have been developed since at least the middle of the last century (Hoek, 1965). Martin (1997) proposed that the behaviour of brittle failure is characterized by the loss of cohesion due to stresses generating new cracks in the rock. That theory was developed from experiments conducted by Martin and Chandler (1994). The first attempts to apply this theory to model brittle rock failure around excavations were made by Martin (1997) who proposed the Hoek-Brown brittle parameter approach. Further developments, stemming from the same loss of cohesion theory, were conducted by Hajiabdolmajid et al. (2002) and Diederichs (2007). The Cohesion Weakening Friction Strengthening (CWFS) approach was proposed by Hajiabdolmajid et al. (2002), it strain-softening principles to characterize the loss of cohesion. The Damage

Initiation Spalling Limit (DISL) introduced by Diederichs (2007) was developed to achieve similar goals to the CWFS but with a different implementation. Both make use of continuum-based numerical models to simulate the behaviour of brittle rock and its loss of cohesion at failure. While both approaches attempt to model the same phenomena, and their underlying mechanistic principles are similar, they have some intrinsic differences. Since their development, multiple authors have proposed partial guidelines for the use and interpretation of such approaches. For the CWFS approach, Walton (2019) developed a set of guidelines to determine input parameters. Perras and Diederichs (2016) investigated the interpretation of the results when using the DISL approach. Yet, there is no extensive investigation, to the authors' knowledge, into the sensitivity of all input parameters for each approach and the effect each has on the results.

The goal of this research was twofold. The first was to assess the robustness and sensitivity of the two most prevalent continuum-based numerical modelling methods, CWFS and DISL. For this study, robustness is the capability of the approach to produce numerically stable, accurate, valid and useful results that are readily interpretable for non-numerical modelling experts in the field of rock mechanics. The second goal is to determine the effect of parameter selection on the results. It builds on the initial guidelines proposed by Walton (2019) to systematically evaluate the CWFS approach. The present investigation addresses the gaps in those guidelines by demonstrating the effects of the selection of input parameters with respect to the modelling results and failure profile. The study comprised of a parametric SA of all input parameters for both approaches to gain a deeper understanding of the effects on the results and the ease of interpreting such results not previously studied in the literature. A sensitivity study on the stress regime was also conducted to determine the capabilities of each approach to reproduce the empirical results given by Martin et al. (1999). To perform both investigations, it is desirable to implement in a commercially available and validated continuum numerical modelling software. Among the options, FLAC was identified as appropriate due to its wide use in the field, its capabilities, and its validation. FLAC was selected to facilitate the repeatability and programmability of the approaches thanks to the scripting language FISH. The post-processing and interpretation are also greatly simplified due to these capabilities. At the end of this study, the understanding of the CWFS and DISL approaches using FLAC is such that the reader can decide on the approach that best suits

their expertise and their purpose for the simulation of brittle rock failure around underground excavations.

### **3.3 BACKGROUND**

Before looking at the usefulness of the CWFS and DISL, their working principles and their application in *FLAC* need to be understood. Both approaches work by applying similar underlying rock mechanics principles and are derived from the same set of ideas of loss of cohesion and increase in friction as rock fails. Yet, their implementation is different, partly due to the nature of the software capabilities they were developed in, and should be understood before attempting to apply them to brittle rock analysis. The following sections explain the need for the development of such approaches, how they work, how they can be applied using *FLAC*, and a case study to which both approaches can be used to simulate.

#### **3.3.1 Brittle Failure Around Underground Openings**

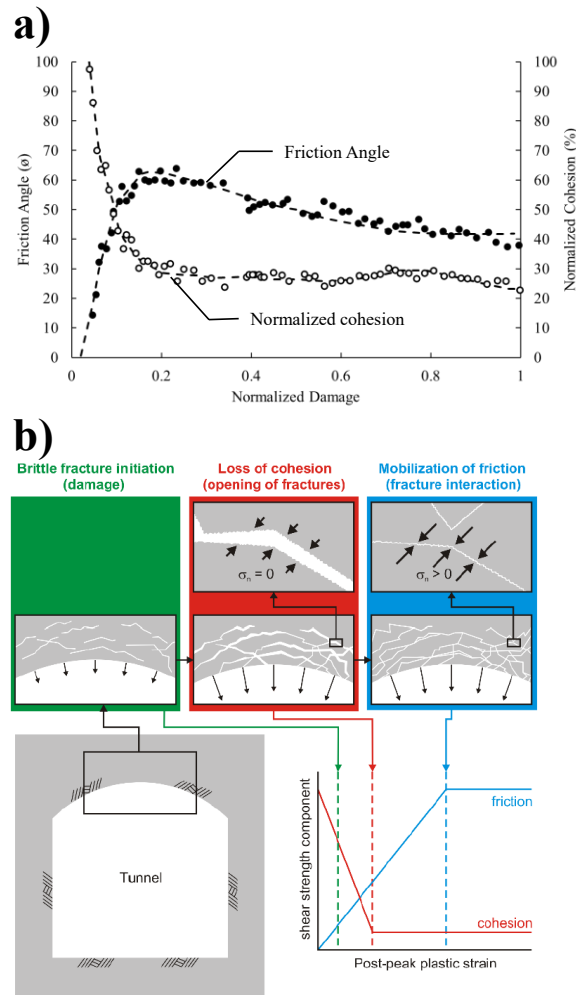
Brittle rock failure is particularly hard to address, as the mechanisms of failure are yet to be fully understood. Failure criteria, such as the Hoek-Brown, are used for jointed rock masses and should not be applied directly to massive brittle rock (Martin, 1997). It is based on the Geological Strength Index (GSI) and is characterized by a curved failure envelope. The GSI is a tool to rate and categorize rock masses based on the conditions of the joints, and the interlocking of the blocks generated, used to qualify a rock mass that allows for the estimation of its strength and deformation properties (Hoek, 2002). While useful in jointed and altered rock masses, massive brittle rock is fundamentally different in its mechanical response. With a high GSI, greater than 75, the Hoek-Brown failure criterion is not valid as it overestimates the strength of brittle rock under low confinement (Martin et al., 1999, Diederichs, 2007, Hoek and Brown, 2018). To mitigate this shortcoming, different techniques need to be used to accurately predict the failure of brittle rock in underground excavations.

When using continuum methods for brittle rock failure modelling, two approaches stand out above the rest, these are the CWFS and the DISL approaches. Both have been extensively studied in the literature (Hajiabdolmajid et al., 2002, Hajiabdolmajid et al. 2003, Diederichs, 2007, Perras and Diederichs, 2016, Dressel and Diederichs, 2021) and have been proposed as viable ways of predicting failure in highly stressed brittle rocks. While in essence they are

trying to model the same scenarios, and their working principles are to a degree the same, their application is different.

The CWFS approach, developed by Hajiabdolmajid et al. (2002) was developed based on laboratory experiments conducted by Martin and Chandler (1994) in which the loss of cohesion and increase in friction were observed as a rock specimen was cyclically loaded and unloaded at different confinement levels. The results from their experiments are shown in Figure 3-1a. The CWFS approach makes use of the Mohr-Coulomb criterion, meaning the rock mass strength is defined by cohesion and friction angle. The approach stems from the fact that intact rock is a purely cohesive material. However, this cohesion is not a permanent characteristic of the rock. As it gets plastically strained the cohesion is gradually reduced to a residual value. Conversely, intact brittle rock has no true pre-peak frictional component. Yet, as it gets strained past its peak strength, the frictional component increases. Intact rock at low confinement levels fails due to tension from the presence of grain-scale heterogeneities such as grain shape, grain contact properties, and microcracks (Lan et al. 2010). The propagation and initiation of such cracks are only cohesive and have no shear component, i.e. friction plays no part. However, once these cracks have propagated, the post-peak strength, failure, and mobilization are due to the friction between such cracks (Hoek and Martin, 2014). Furthermore, the mobilization of cohesion and friction are not simultaneous. Friction reaches its residual value at a larger plastic strain than cohesion. The amount of plastic strain required to reach the residual values is called the critical plastic strain. Cohesion and friction change linearly, in the numerical models, from the onset of plastic strain up to the critical plastic strain (Hajiabdolmajid et al., 2002), as seen in Figure 3-1b. With triaxial testing of rock samples and diverse loading conditions, the degradation of cohesion and increase in friction can be visualized (Martin, 1997). Some have suggested that the transition from peak values to residual should not be linear, but rather a gradual asymptotic change, as seen from the lab experiments by Martin and Chandler (1994) in which the degradation of cohesion and increase in friction are gradual and smooth (Renani and Martin, 2018).





**Figure 3-1 a) Loss of cohesion and increase in friction angle as a function of normalized damage from the experiments conducted by Martin and Chandler (1994) b) Conceptual representation of cohesion and friction mobilization as functions of rock damage and post-peak plastic strain around an underground excavation (Corkum et al., 2012)**

There are multiple implications from this theory when applied to underground excavations. Near the boundary, the tangential compressive stresses are high while the radial stresses are low to non-existent. This creates a low confinement environment in which the strength is at first dominated by the cohesive component. As it starts to fail, open fractures form with a lower frictional component. Once the stress redistributes, and the strain increases, frictional interactions within the fractures dominate the strength (Corkum et al. 2012). This process is illustrated in Figure 3-1b. After excavating near the tunnel boundary, the strength of the rock mass is purely frictional as it is plastically strained to its upper bound. Further

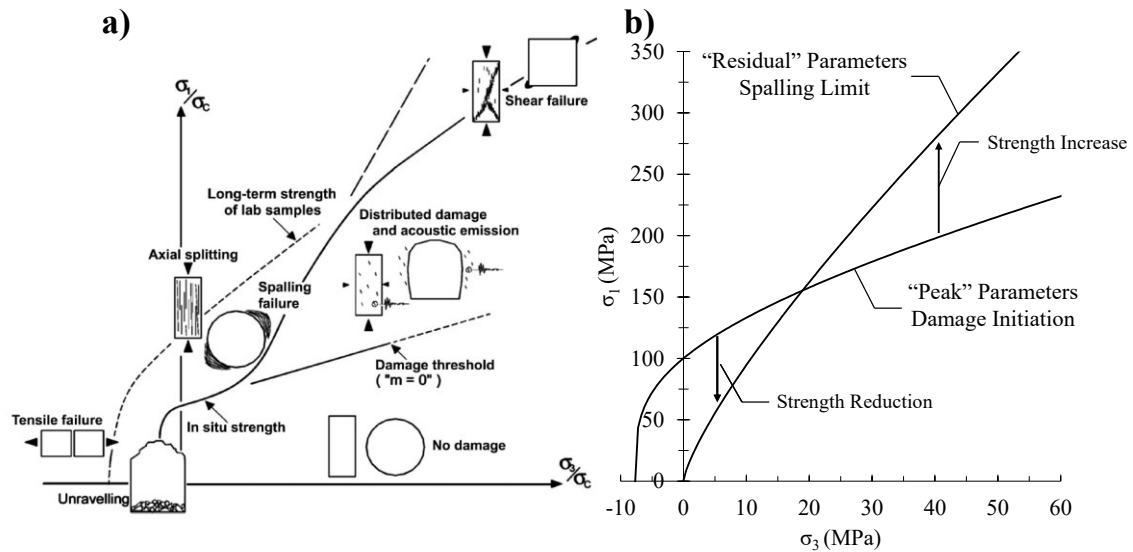
from the tunnel boundary (i.e., increased confinement), the rock mass transitions to being dominated more by cohesion.

Another approach to represent brittle rock failure around tunnels was developed by Diederichs (2007), referred to as the Damage Initiation Spalling Limit (DISL). The theory is similar to that of the CWFS approach. At low confinement, the strength of the rock is controlled by the tension generated from the microcracks and grain-scale heterogeneities. This lower bound confinement can range up to 0.4 to 0.6 times the  $\sigma_{UCS}$  of the rock (Hoek and Martin, 2014). At high confinement, the rock mass is characterized by the long-term strength of the rock, which is the crack damage threshold in a laboratory setting, usually 0.6 to 0.8 times the  $\sigma_{UCS}$  (Hoek and Martin, 2014). At this confinement, the failure is dominated by shear fractures. The development of the DISL approach also stems from the observations of cohesion loss and friction mobilization in Lac du Bonnet (LdB) granite by Martin and Chandler (1994). The theoretical representation of a failure envelope with these characteristics is shown in Figure 3-2a. To apply this s-shaped strength envelope to continuum-based numerical models, it can be simplified to two separate envelopes, peak and residual (Fig 2b). DISL makes use of the Hoek-Brown failure criterion (Hoek and Brown, 2018). The damage initiation parameters can be calculated with (Perras and Diederichs, 2016):

$$s_p = \left( \frac{\sigma_{ci}}{\sigma_{UCS}} \right)^{\frac{1}{a_p}} \quad (3-1)$$

$$m_p = s_p \left( \frac{\sigma_{UCS}}{T} \right) \quad (3-2)$$

Where the subscript  $p$  denotes “peak”, and  $a_p$  is 0.25,  $\sigma_{ci}$  is the crack initiation stress,  $\sigma_{UCS}$  is the unconfined compressive strength, and  $T$  is the tensile strength. The residual  $s$  ( $s_r$ ) is as close to zero as possible to simulate a complete loss of cohesion (0.0001 is used by the authors), the residual  $m$  ( $m_r$ ) can vary from 6 to 12 and the residual  $a$  ( $a_r$ ) is 0.75 (Perras and Diederichs, 2016). This results in the strength envelope when applied to continuum models having two distinct envelopes, one for the damage initiation, and the other representing the residual strength for the spalling limit, as shown in Figure 3-2b.



**Figure 3-2 a) DISL theoretical Bi-Linear Strength Envelope (Diederichs, 2007) b) Application of the theoretical DISL strength envelope with initial (Damage Initiation) and residual (Spalling Limit) strength for continuum numerical models.**

Just like in the case of the CWFS approach, the selection of strength parameters in the DISL approach has meaningful implications when it comes to underground excavation modelling and design. Near the boundary, where low confinement is present, the strength is defined by the damage initiation threshold. While further away from the excavation boundary, the strength is characterized by the spalling limit. A continuum numerical method software can be used with a constitutive model that can represent this peak and residual curves in order to predict the failure zone surrounding an excavation.

While both approaches are useful for representing failure around underground excavations, they are techniques to manipulate continuum numerical models to represent a mechanism that is not continuum-based in nature. The CWFS and DISL approaches cannot explicitly simulate what occurs when the rock around an excavation fails. When using continuum-based numerical models, there is no explicit simulation of fracture propagation, material separation, and material detachment. This type of model cannot capture these behaviours. Caution must be exercised when using these approaches in that the results are an approximation and need to be interpreted with the true mechanisms in mind.

### 3.3.2 CWFS and DISL Implementation in FLAC

The selection of modelling software to be used for the analysis of the approaches is key for a successful investigation. The CWFS approach was first introduced using Itasca's software *FLAC* (Hajiabdolmajid et al., 2002). While the DISL approach was first developed using Rocscience's *PHASE2* (now *RS2*) (Diederichs, 2007). This gives one source for discrepancies between the approaches as both software codes work differently. *RS2* is a finite element approach with implicit solutions and *FLAC* is an explicit finite difference numerical program (Rocscience, 2022, Itasca, 2015). To be able to implement CWFS, the software needs to be able to apply strain-dependent rock parameters, making *FLAC* a viable software. *FLAC* also processes the ability of scripting, which aids in the systematic change of input strength and stress parameters. A detailed comparison of the software is beyond the scope of this study, others have investigated the difference in selection for different applications (Cai, 2008).

The selection of constitutive models within *FLAC* is important for the modelling of brittle rock failure when using numerical modelling software. For the CWFS approach, the main characteristics required are that the constitutive model has the Mohr-Coulomb failure criterion and that the strength parameters can change with plastic shear strain ( $e^{ps}$ ). A suitable constitutive model in this scenario is the *Strain-Hardening/Softening Model*. Its main feature is that the residual strength parameters are a function of the plastic strain. It allows for the increase or decrease of parameters as the strain evolves. The total plastic strain is a function of plastic strain in the principal and minimum stress directions according to (Itasca, 2015):

$$\Delta e^{ps} = \left\{ \frac{1}{2} (\Delta e_1^{ps} - \Delta e_m^{ps})^2 + \frac{1}{2} (\Delta e_m^{ps})^2 + \frac{1}{2} (\Delta e_3^{ps} - \Delta e_m^{ps})^2 \right\}^{\frac{1}{2}} \quad (3-3)$$

where:

$$\Delta e_m^{ps} = \frac{1}{3} (\Delta e_1^{ps} + \Delta e_3^{ps}) \quad (3-4)$$

and  $\Delta e_j^{ps}, j = 1, 3$  are the principal plastic shear strain increments (Itasca, 2015). Other parameters required for this constitutive model are peak cohesion ( $c_p$ ), residual cohesion ( $c_r$ ), initial (or peak) friction angle ( $\phi_i$ ), mobilized (or residual) friction angle ( $\phi_m$ ), critical strain

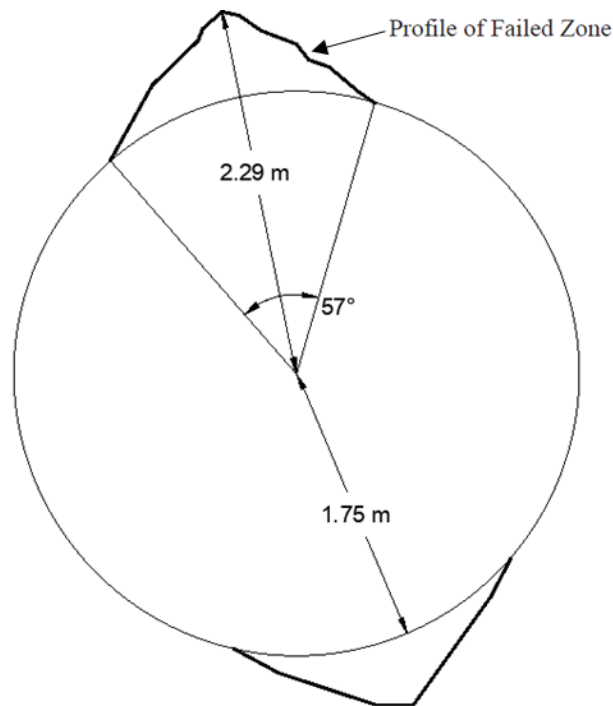
( $e^{ps}$ ), dilation angle ( $\psi$ ), tensile strength ( $T$ ), modulus of elasticity ( $E$ ), Poisson's ratio ( $\nu$ ), and density ( $\rho$ ). Hajiabdolmajid et al. (2002) made use of this constitutive model for their study.

The DISL approach was first introduced using the Generalized Hoek-Brown constitutive model from *Phase2* (Diederichs, 2007). The implementation was done by setting a peak failure envelope matching the crack initiation threshold proposed by Martin et al. (1999), and a residual failure envelope equivalent to the spalling limit (Diederichs, 2007). Due to the nature of the version of *Phase2* used, the transition from peak to post-peak failure envelope was instantaneous and independent of practical strain. A similar constitutive model, which allows for a peak and post-peak failure envelope, exists in *FLAC* called the modified Hoek-Brown constitutive model. To be able to use this constitutive model in *FLAC*, the transition from peak to post-peak needs to be a function of shear plastic strain. Therefore, a critical plastic strain is needed to implement the DISL approach. This involves the selection of an extra parameter that was not implemented by the original authors (Diederichs, 2007) in *Phase2*.

### **3.3.3 The Mine-by Experiment tunnel at the Underground Research Laboratory**

To directly compare the two approaches, a common case study was analyzed. Both approaches have been used multiple times in the literature to model the Mine-by Experiment (MBE) tunnel at the Underground Research Laboratory (URL) (Hajiabdolmajid et al., 2002, Hajiabdolmajid et al., 2003, Diederichs, 2007, Cai and Kaiser, 2014, Xu et al., 2022). The MBE was an experiment conducted in Manitoba, Canada, to observe the brittle failure of rock mass in a high stress field. The rock in the tunnel is mainly LdB granite, a highly competent crystalline rock. The construction was done in a massive batholith dated to the Late Kenoran age ( $2680 \pm 80$  Ma). The tunnel was excavated approximately 420 m below the ground surface at the 420 level. At this level, there were no joints or discontinuities found. The excavation approach was by careful line drilling and without the use of explosives to avoid any adverse effects caused by blasting damage. The tunnel was 3.5 m in diameter and was excavated in 1 m advances for a total length of 46 m (Martin et al. 1997). The tunnel was driven parallel to the intermediate stress to maximize the effect of stress redistribution on the boundary. Construction took place between 1983 and 1989. Great care was taken to

document the ground behaviour as the excavation was occurring. The in situ stress regime was well documented, Table 3-1 is a summary of the state of in-situ stresses as measured using multiple stress measurement techniques. The laboratory strength of the rock was also carefully studied. It was determined to have the Hoek-Brown intact properties shown in Table 3-2. After excavation advanced, spalling was observed. A v-notch failure profile was seen due to spalling around the excavation boundary (Martin and Kaiser, 1996) as shown in Figure 3-3.



**Figure 3-3 Simplified MBE failure profile for the 420L (chainage unknown) after full development of the v-notch. The measures of failure were obtained by digitizing the original profile found in the literature (after Martin et al., 1997)**

**Table 3-1 The in-situ state of stress at the 420 L of the URL (Martin and Kaiser, 1996)**

Stress	Magnitude (MPa)	Trend (°)	Plunge(°)
$\sigma_1$	60	145	11
$\sigma_2$	45	54	8
$\sigma_3$	11	290	77

**Table 3-2 LdB intact rock properties using Hoek-Brown failure criterion (Martin and Kaiser, 1996)**

<b>Property</b>	<b>Value</b>
Density (kg/m <sup>3</sup> )	2,630
$\sigma_{UCS}$ (MPa)	213
$m$	30.8
$s$	1
$E$ (GPa)	65
$\nu$	0.25

A v-shaped notch failure occurred in both the roof/back and the floor of the tunnel. The difference between the back and the floor of the tunnel can be explained by multiple phenomena. The tunnel was not driven perfectly parallel to  $\sigma_2$  which gives a different stress redistribution and stress path between the top and the bottom (Read et al., 1998). The tunnel floor was mainly granodiorite at the profile of interest (Figure 3-3) (Martin, 1997). The granodiorite has, on average, a larger  $\sigma_{UCS}$ , and a larger  $\sigma_{ci}$  than LdB granite (Martin, 1997). Lastly, the muck from the excavation provided minor extra confinement to the floor, not allowing it to fail in the same “unsupported” manner as the roof (Martin, 1997). The difference between notch sizes has been attributed to one or a combination of these reasons.

Using the parameters from Table 3-2 in a continuum plastic Hoek-Brown numerical model severely overestimates the strength of the rock around the tunnel and gives an unrealistic sense of confidence (Martin, 1997, Hajiabdolmajid et al., 2003). Therefore, the CWFS or DISL approaches must be applied to represent the failure profile accurately. For the simulation of the MBE using CWFS, implemented in *FLAC*, Hajiabdolmajid et al. (2003) suggested the values detailed in Table 3-3. They obtained these values from the investigation done by Martin and Chandler (1994) and the calibration of the model to achieve the expected profile.

**Table 3-3 LdB CWFS Material Properties (after Hajiabdolmajid et al. 2002)**

<b>Parameter</b>	<b>Peak/Initial</b>	<b>Residual/Mobilized</b>
Cohesion (MPa)	50	15
Friction Angle (°)	0	48
Tensile Strength (MPa)	10	0
Dilation Angle (°)		30
Cohesion Critical Strain		0.002
Friction Critical Strain		0.005

Diederichs (2007) suggests the strength parameters shown in Table 3-4 to implement the DISL approach for the simulation of the MBE using *RS2*. They used Equation (3-1) and Equation (3-2) using the data from the LdB granite to obtain the most adequate profiles. Their investigation was done using *RS2*, therefore no  $e_{crit}^{ps}$  was needed by the software for the residual parameters.

**Table 3-4 LdB DISL Material Properties (after Diederichs, 2007)**

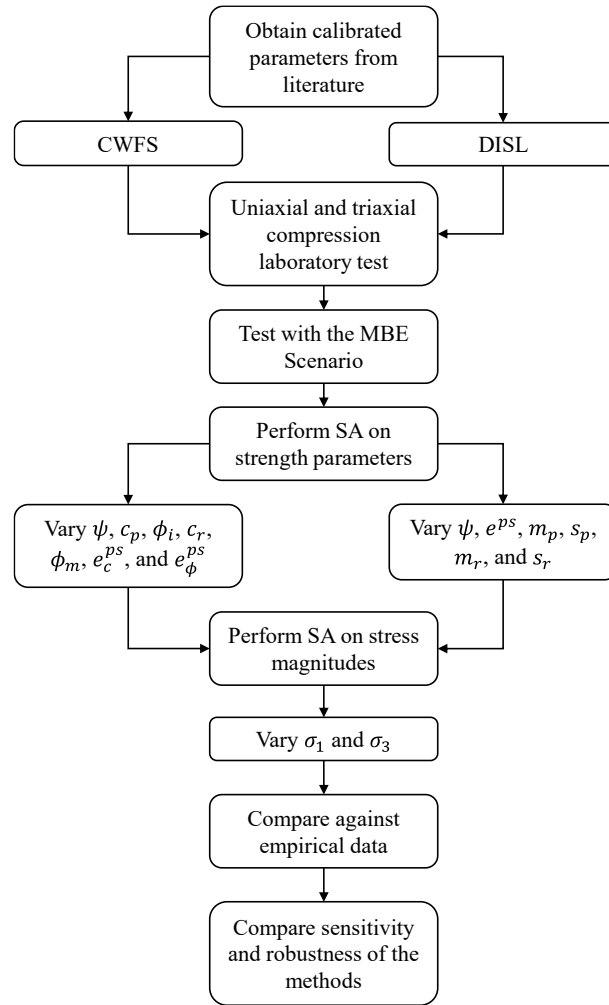
Parameter	Peak	Residual
$m$	1	6
$s$	0.033	0.00001
$a$	0.25	0.75
Dilation Angle (°)		0
$\sigma_{UCS}$ (MPa)		235

### 3.4 OVERVIEW OF THE RESEARCH METHODOLOGY

Assessing the effectiveness of excavation performance prediction using both approaches requires a detailed and objective process. This study aims to determine how viable the use of the CWFS and DISL approaches are for use by rock engineering practitioners. The goal is to propose which approach achieves results that coincide the best with the field observations and remain interpretable without excessive complexity and subjective judgement. The understanding of the approach will also be improved as the input parameters of each will be analyzed separately. In this study, the process began by understanding the behaviour of both approaches of interest in simulated laboratory experiments. The triaxial and unconfined tests were performed using numerical models to understand the underlying working principles for both approaches. Then each was tested on a case study (the MBE tunnel) using the literature values as a benchmark. The values proposed by Hajiabdolmajid et al. (2002) for the CWFS approach and Diederichs (2007) for the DISL approach were used for the initial investigation. The sensitivity of the strength parameters was used as a test of robustness and adequacy for design. The robustness of each approach is determined by its capability of producing numerically stable, accurate and valid results for a wide range of conditions that are also readily interpretable. A parametric SA of each parameter was done to better characterize their effect on the failure profiles generated by the numerical models. Lastly, by performing an in



situ stress magnitude sensitivity analysis the approaches are analyzed in diverse scenarios. With this, both approaches were tested to multiple fictitious scenarios to determine their validity under a wider range of case studies. A general flowchart of the research process for this investigation is shown in Figure 3-4.



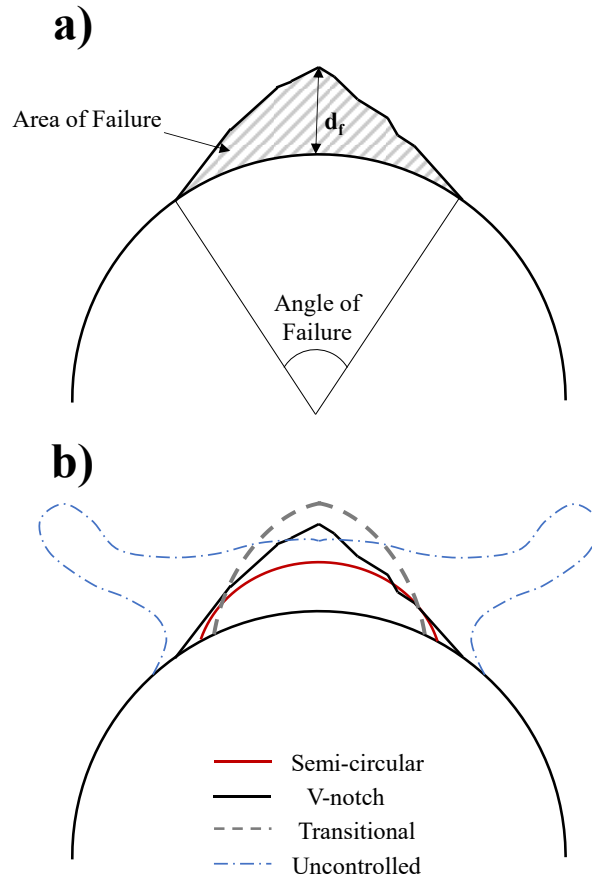
**Figure 3-4 General methodology for the comparison of sensitivity and robustness of CWFS and DISL using the URL MBE as a case study.**

To compare the results of the numerical models to the field observation of the MBE, an objective method of quantifying the failure profile was needed. For this study, failure is analyzed according to the yield state of the zones in *FLAC*. Zones that are in active or past failure states are considered to be failed. For the strain-softening constitutive model, failure can assume any of four states, yielded in tension past or active, yielded in shear past or active. For the Hoek-Brown constitutive model, there are multiple failure states, they occur with the

combination of failure in shear and tension and whether this is in the present or past. It is important to note that Perras and Diederichs (2016) explained that in the DISL approach failure of a zone (mesh element) does not necessarily represent the failure and unravelling of the rock mass when applying this approach in *RS2*. They stated other numerical considerations need to be asserted to define the depth of failure with this approach and provide guidance in their study.

While all results can be presented graphically and overlaid onto the actual failure profile, this would be a laborious and unclear representation. Therefore, quantifying failure characteristics numerically is a desirable alternative. A single number, e.g., depth of failure ( $d_f$ ), is typically not enough to describe the entire failure profile. Therefore, five different measures are proposed to characterize the failure profiles in this study.

The first measure of failure is similar to the convention proposed by Martin (1997) for the  $d_f$ , which is given from the edge of the excavation boundary to the tip of the formed failed notch. It can also be expressed as a ratio between the  $d_f$  and the tunnel radius ( $a$ ). The next measure is the angle of failure which is measured from the start of the notch to the end along the tunnel boundary. It is the angle of the arch generated between the start of failure and the end of failure measured from the centre of the excavation as an apex point. The area of failure is also a parameter of interest, it helps to indicate the cross-sectional area of rock that may potentially unravel. The area was measured by looking at the model zones that failed and summing the individual areas. This introduces a mesh size dependency for its measurement, i.e., precision is affected by zone resolution. These previously mentioned measures can be visualized in Figure 3-5a. The last measure is the shape of failure which can be “v-notch” shaped, “semicircular”, and “transitional” between both as seen in Figure 3-5b. The shape is a somewhat subjective measure. Figure 3-3, in Section 3.3.3, shows the values of the observed failed profile. The observations by Martin (1997) for the MBE at the URL are categorized using these measures of failure in Table 3-5.



**Figure 3-5 Graphical demonstration of the measures of failure for the roof of an underground excavation a)  $d_f$ , angle of failure, and area of failure b) shape of failure classification and uncontrolled failure example**

**Table 3-5 MBE measures of failure characterization from the field observation of the 420L (chainage unknown) from observations by Martin and Kaiser (1996)**

Measure	Value
Controlled	Yes
$d_f$	0.54 m
Angle of Failure	57°
Area of Failure	0.46 m <sup>2</sup>
Shape of Failure	v-notch

An alternative outcome of the numerical models is that none of the previous measures of failure can be quantified. Therefore the last measure of failure is devised, which is termed “controlled” or “uncontrolled”. This controlled or uncontrolled categorization does not imply failure of the tunnel per se, rather it demonstrates the failure/yielding of the continuum model elements/zones. It is a numerical outcome of the model from redistribution of stresses. A

model that shows an uncontrolled yielding reaction does not invalidate the results, yet it does complicate simulation interpretation and performance assessment. This type of result makes the interpretation more challenging requiring specialized skills in numerical modelling to do so. An example of the failed profile categorized as uncontrolled is shown in Figure 3-5b, the uncontrolled failure categorization can take many other shapes. A goal of this study is to generate an interpretable result, the rest of the measures of failure for an uncontrolled profile will be given an "NA" value.

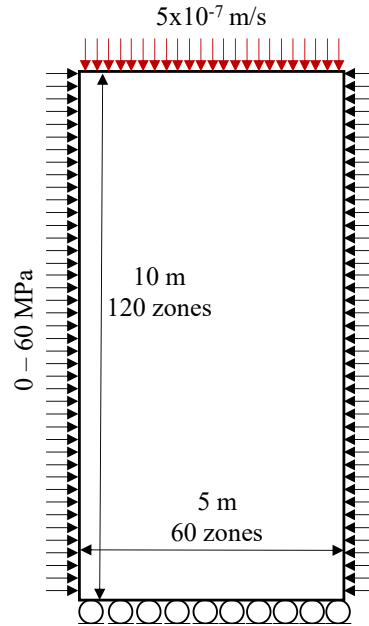
### **3.5 UNCONFINED AND CONFINED COMPRESSION TEST SIMULATIONS**

The CWFS and DISL approaches can be understood in isolation by their behaviour under unconfined and confined compressive tests to understand their reaction to increasing stress, particularly for post-yield plastic deformation. The triaxial test showed how, after the onset of yielding was reached, the strength of the rock mass was affected in different ways: at some confinements, there was a strength increase and at others, there was a strength decrease. It also served as a check of the theoretical strength envelope with the results from the simulated tests. It demonstrated the behaviour of the continuum numerical method under the desired condition and was not a direct comparison to the actual LdB granite laboratory tests conducted by Martin and Chandler (1994).

#### **3.5.1 Methodology for Laboratory Testing Simulations**

The simulation of these tests was done using *FLAC* with the constitutive models mentioned in Section 3.2.2. The samples for this test were 10 m in height by 5 m in width (the effects of gravity are disregarded). The meshing of the model was fine and uniform, with square zones. The sample was divided into 120 zones vertically by 60 zones horizontally. As *FLAC* is an explicit FDM, the compressive load was applied as a velocity in the negative *y* direction at the top of the specimen, with the bottom being fixed in the *y* direction (roller boundary). The velocity was slow enough such that the stresses were evenly propagated throughout the numerical specimen as the model steps forward in time. The selected velocity for these samples was  $5.0 \times 10^{-7}$  m/s. For the triaxial tests, the stresses were initiated in all directions, the model was run to equilibrium, and then the compressive loading velocity was applied. The setup of the test is shown in Figure 3-6. For the LdB granite the real test was conducted

up to a confinement of 60 MPa (Martin, 1997), therefore in this study the same threshold was used.



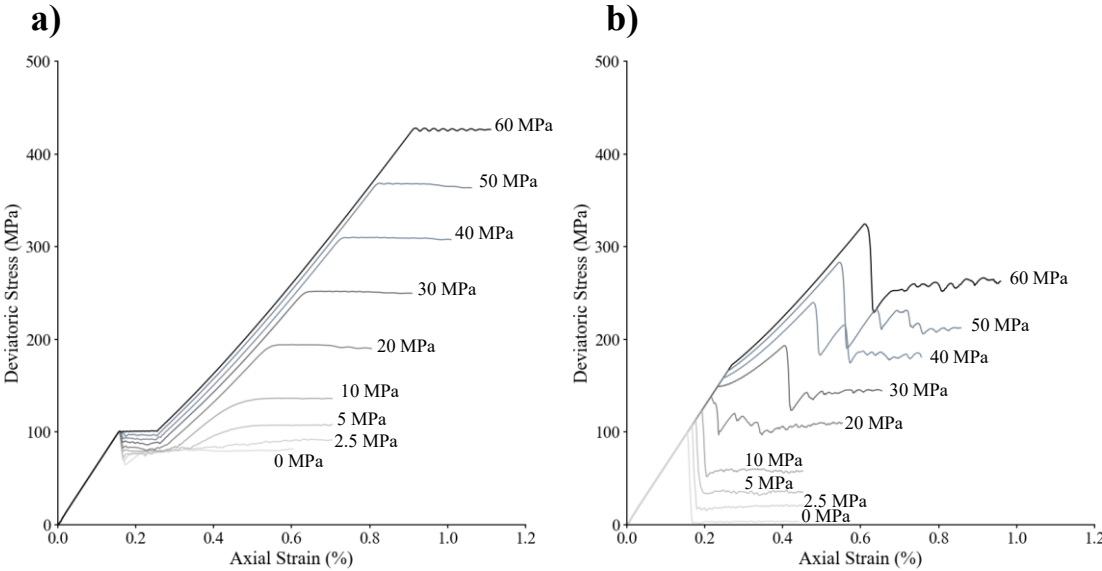
**Figure 3-6 Model setup and geometry for unconfined and triaxial test using *FLAC*.**

The strain of the sample was measured by querying the zones for the vertical ( $y$  direction) strain of each zone along a horizontal line in the middle of the specimen. The values were taken at every timestep and averaged to obtain an axial strain history. To measure the axial stress, the zones in the middle of the specimen were queried for vertical stress and then averaged. Finally, the ultimate stress at every confining stress was taken to compare with the theoretical strength envelopes.

### 3.5.2 Results for Laboratory Testing Simulations

The values used for the strength parameters for the CWFS models are shown in Table 3-3. The results are visualized first by looking at the stress-strain curves for all the triaxial tests conducted, as shown in Figure 3-7a. The mobilization of  $c$  and  $\phi$  is clearly visualized in this Figure 3-7. At an axial strain of 0.2%, the strain softening behaviour starts to take place. For the tests from 0 to 5 MPa of confinement, the specimens experienced strength reduction after the onset of mobilization, and at higher confinements, the strength is increased (strain hardening). The behaviour of these tests is not a reflection of a real triaxial test on LdB, they are a demonstration of the CWFS model behaviour. The deviation from the true triaxial test

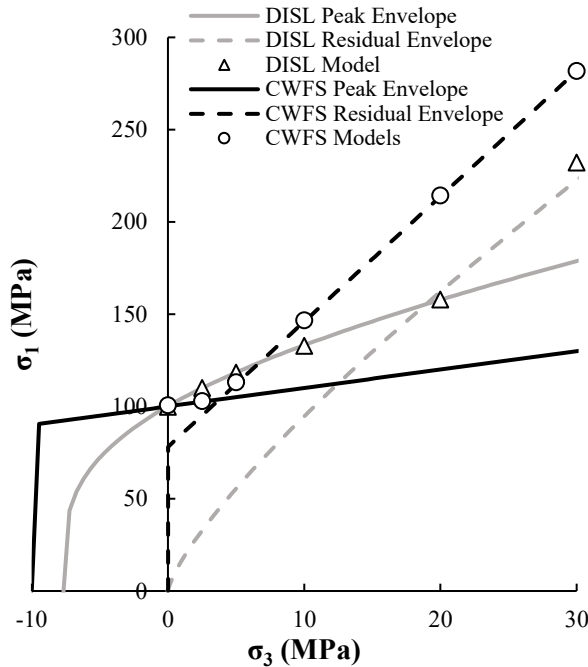
has been noted and addressed by Renani and Martin (2018). They suggested using a non-linear relationship between  $e^{ps}$  and the strength parameters to better match the stress-strain curves. There are other continuum modelling techniques for simulating unconfined and triaxial tests of the LdB granite that better replicate the behaviour of the rock (Sanipour, et al. 2022). Figure 3-7b demonstrates the same set of tests but for the DISL parameters shown in Table 3-4. The tests showed that at low confinement, after peak strength was reached there was an immediate loss in the strength corresponding to an  $s$  decrease to almost 0. This behaviour was brittle, which is similar to the observations by Martin (1997). At higher confinements, the strength increased at the onset of plastic yielding. The ultimate strength of this highly confined test was dominated by the  $m_r$  value.



**Figure 3-7 Simulated triaxial test results in deviatoric stress and axial strain space using FLAC for the LdB granite according to a) CWFS suggested parameters and b) DISL suggested parameters.**

The results of these tests can alternatively be visualized by plotting the peak strengths from the investigation against the theoretical peak and residual strength envelopes for both the CWFS and the DISL approaches. Figure 3-8 is the plot of the theoretical envelopes and the results of the simulations. Both intended behaviours are replicated using the triaxial test, therefore the behaviour of the numerical models with the parameters indicated should behave as expected. It supported the position that *FLAC* can be used to simulate these types of complex behaviours. The  $\sigma_{UCS}$  value for both of the approaches was relatively similar at

around 112 MPa. Their confined strength on the other hand was different. At low confinement (<5 MPa), DISL has greater peak strength. At higher confinements (> 5 MPa), the peak strength of the CWFS values is higher. The difference in strength increased with increasing confinement. At a confining pressure of 20 MPa, the strength of the CWFS envelope was over 50 MPa larger than the DISL one. These two approaches are proposed to work at low confinement situations (near excavation boundary), for such ranges both approaches have similar strength. Presenting a wide range of  $\sigma_3$  gives insight to the modelling mechanisms of the CWFS and DISL approaches.



**Figure 3-8 Peak strength for the triaxial test simulation using CWFS and DISL parameters from literature compared to the theoretical peak and residual envelopes (determined from input parameters) of each approach**

### 3.6 REPRODUCTION OF THE MBE AT THE URL BENCHMARK MODELLING CASES

Both the CWFS and DISL approaches were originally proposed with a calibrated set of values by the respective authors (Hajiabdolmajid et al., 2002, Diederichs, 2007) for the MBE at the URL. For the CWFS approach, *FLAC* was also used, but it has been updated numerous times since it was first implemented. For the DISL approach, the calibration was done using *Phase2*. Due to these two reasons, it was necessary to investigate the results of each initial calibration if implemented with the current version of *FLAC*.

### 3.6.1 Methodology for the Benchmark Modelling Cases

As an initial modelling benchmark, the strength parameters provided in the literature that applied these approaches to the URL scenario were used to simulate the same scenario with the current version of *FLAC* (v 8.10.484). The *Strain-Softening constitutive model* was used for the reproduction of these results. The values for this section are detailed in Table 3-4. As this approach was already implemented by the original authors in *FLAC*, no further modifications are needed. In theory, as these values were calibrated by the original authors, a similar profile is expected.

Diederichs (2007) suggested that the MBE can be better simulated in *Phase2* with the parameters shown in Table 3-4. To implement it in *FLAC* the constitutive model used was the *Modified Hoek-Brown constitutive model* as detailed in Section 3.2.2. This constitutive model requires a critical strain parameter. Diederichs (2007) used *Phase2* which does not utilize this parameter because mobilization from peak to residual parameters is “instantaneous”; therefore, the critical strain should be a relatively low value. Obtaining a suitable  $e_{crit}^{ps}$  for the DISL approach requires some interpretation of the mechanism of the approach and the original development using *RS2*. This issue has been rarely discussed in the literature; therefore, providing a definite value is complicated. Lorig and Varona (2013) came up with a set of guidelines for critical strain calculation. They suggest critical strain can be estimated as a function of the GSI by:

$$e_{crit}^{ps} = \frac{12.5 - 0.125 * GSI}{100} \quad (3-5)$$

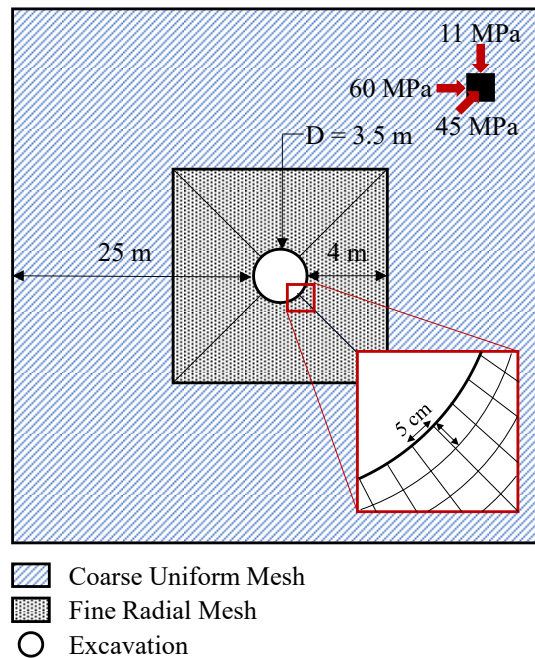
The relationship between GSI and critical strain is linear. Using a GSI of 100 gives a  $e^{ps}$  of zero, which is not possible in *FLAC*. Yet, using a GSI of 99 the  $e^{ps}$  resulting in 0.125%. This is also in the same order of magnitude as the  $e_c^{ps}$  and  $e_\phi^{ps}$  values used for the CWFS approach. The use of Equation (3-5) has many assumptions built into it. Mainly it was developed for strength weakening Hoek-Brown rock mass, rather than more complicated behaviours like DISL, and it was developed for rock slopes. Lorig and Varona (2013) also point out the need to scale the values depending on the zone size if shear bands are found within the model. The equation suggests that  $e_{crit}^{ps}$  is a function of *GSI*; therefore, it can only



truly be applied to jointed rock mass. Using this equation is only a starting point in determining a suitable critical strain value for the implementation of DISL in *FLAC*.

### 3.6.2 MBE *FLAC* Model Setup

To replicate the results from the literature, the model geometry for the MBE tunnel was set up in *FLAC*. The setup was a simple circular opening, with a diameter of 3.5 m as in the MBE case. The outer boundary of the model was 25 m from the centre of the excavation in all directions, which was far enough to not influence stress redistribution. The boundary was fixed in all directions. The mesh was divided into two distinct zones. The inner zone, which was 4 m away from the center of the excavation in every direction, had a finer radial mesh with zone sizes of 5 cm  $\times$  5 cm. This finer inner mesh consisted of over 6500 individual zones. The rest of the model had a coarser mesh with square zones with 10 cm per side to decrease computational time. A simplified graphical representation of the model setup is shown in Figure 3-9. The stress regime was introduced horizontally and vertically to simplify the model and ease of results presentation, i.e.  $\sigma_v = \sigma_3 = 11$  MPa,  $\sigma_H = \sigma_1 = 60$  MPa, and  $\sigma_h = 45$  MPa. The change of stress orientation did not have a detrimental effect as gravity is neglected for this analysis.

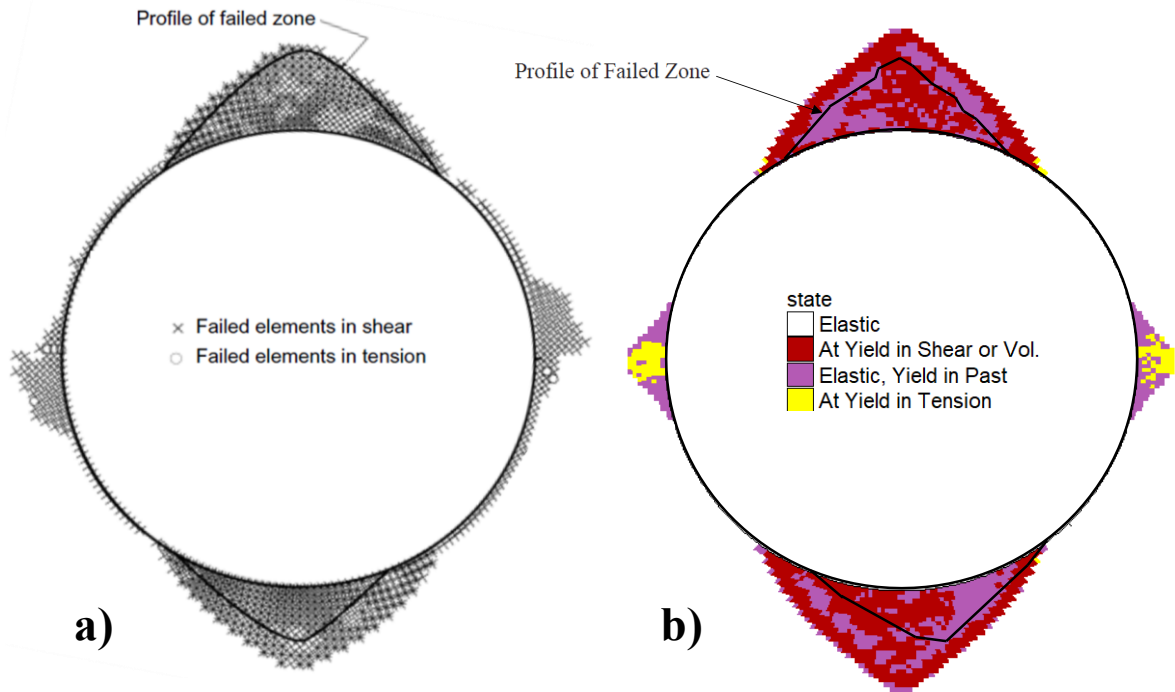


**Figure 3-9 Model setup and simplified geometry for the URL MBE using *FLAC* with rotated stress orientations for simplicity showing the different zone densities.**

An internal pressure reduction method was used to limit the dynamic loading effect of the excavation. The internal pressure was applied with *FLAC*'s built-in internal-applied-relax vector stresses scheme around the excavation. There were 20 steps of stress relaxation. The first stage had an internal pressure ( $P_i$ ) equal to the initial stress on the model ( $P_o$ ), i.e.  $P_i/P_o = 1$ . Every relaxation step afterward decreased the ratio by 5%. In the last step, there was no applied  $P_i$  ( $P_i/P_o = 0$ ). This last step simulated the ultimate equilibrium state of the tunnel far away from the tunnel face at which the failure state of zones was used to determine the failure profile. A state of pseudo-static equilibrium was judged on the basis that the unbalanced forces reached an acceptable minimum value (Itasca, 2015).

### 3.6.3 CWFS Results

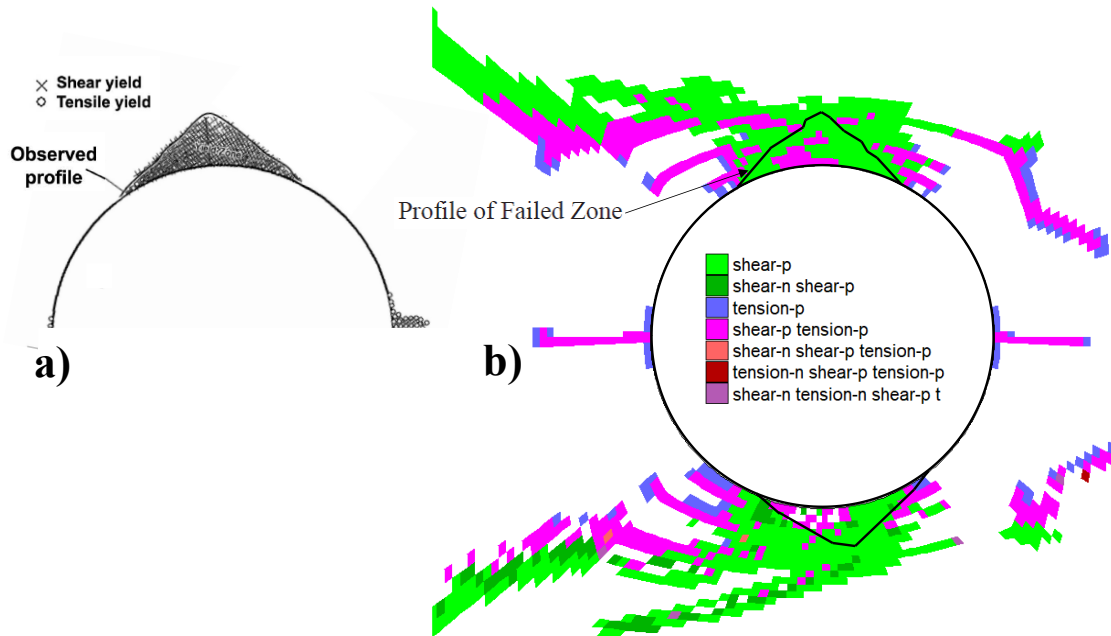
Hajiabdolmajid et al. (2002), suggested using the values from Table 3-4 to simulate the MBE using CWFS in *FLAC*. They obtained the profile shown in Figure 3-10a using these values. The profile approximated the actual failure on the roof of the excavation, the sides of the excavation have a slight overprediction of failure. While there was no observable failure on the side of the excavation, monitoring indicated that there were some acoustic emissions on the walls (Martin, 1997). Hajiabdolmajid, et al. (2002) reported results that are fairly similar to the actual profile, with the current *FLAC* version a slightly different result is achieved, as shown in Figure 3-10b which is the direct application of the Table 3-3 parameters with the current version of *FLAC* (*FLAC 8.1*). The results from this study slightly overpredicted the failure observed at the MBE. The difference might be attributed to the difference in zone size, as the zone size used by Hajiabdolmajid et al. (2002) is not known to the authors.



**Figure 3-10 FLAC results for the CWFS approach showing failure profile with vertical and horizontal stress orientations for a) Hajiabdolmajid, et al. (2002) results rotated to align v-notch with vertical and horizontal axis b) results of the present investigation.**

### 3.6.4 DISL Results

To implement the DISL approach, Diederichs (2007) suggested the strength parameters from Table 3-4. Using these values, a close approximation was made as shown in Figure 3-11a by the original author. The study uses two different dilation factors for the roof and floor of the excavation. With these values, the resulting profile is presented in Figure 3-8b. It shows an uncontrolled zone failure. The result might raise concern that the critical strain value is too low to accurately represent the failure profile. However, a value higher than that would indicate a lower GSI than the one in situ based on Equation (3-5). Furthermore, the same values from Table 3-4 and similar mesh density and type were used with the current version of *RS2* and gave similar uncontrolled failure as seen in *FLAC*. This gives further confidence in the selection of critical strain.



**Figure 3-11 Results for the DISL approach failure profile with vertical and horizontal principal stresses for a) the top half of the profile reported by Diederichs (2007) obtained using *RS2* and b) *FLAC* results of the present investigation.**

In this investigation, the failure profile is taken from the yielded zones from the numerical model results produced directly from *FLAC*. Perras and Diederichs (2016) stated that this is an erroneous interpretation of failure profiles using the DISL approach. Instead, they suggest that rather than yielded zones, the failure profile is categorized by “the first point where  $\sigma_3$  increases from the value at the excavation surface” (Perras and Diederichs 2016). This statement implies that failure is considered to be where the numerical model shows failure zones where there are low confinement levels. This interpretation of failure, although valid, requires some judgement and a fundamental understanding of numerical models.

### 3.7 SENSITIVITY ANALYSIS OF STRENGTH PARAMETERS

To understand how a parameter affects the results of each approach, a sensitivity analysis was conducted. The effects of parameters can be better visualized if they are varied independently. For each variation, a new failure profile can be produced and compared to the benchmark. The process is done first for the CWFS approach and then the DISL approach. Both SA studies were done independently of each other; yet attempting to keep some similarities between both. The model formulation using *FLAC* is the same as that detailed in the previous section.

### 3.7.1 Strength Parameters Sensitivity Analysis Methodology

To understand the sensitivity and robustness of both techniques, a SA was conducted. To be able to use each approach for design, every parameter must first be looked at individually. By isolating each parameter a sense of their effect was evaluated. The implementation of sensitivity analysis in this paper was done by varying one of the parameters individually while keeping the rest at the benchmark value given in the previous section. For example, if the parameter of interest was the residual cohesion, this was changed to a different value while keeping the rest as listed in Table 3-3. All parameters were assumed to be independent, except for tensile strength which is correlated to other parameters (such as peak and residual cohesion). The main goal was to understand the impact of individual parameters on modelling results, rather than their combined effect.

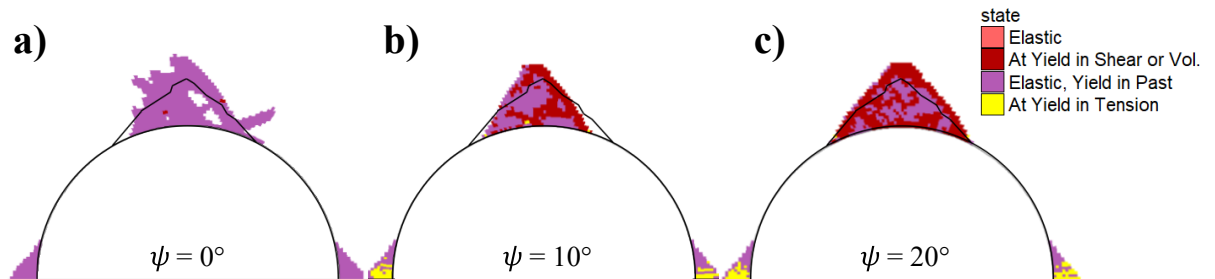
The parameters varied for the CWFS approach were peak cohesion ( $c_p$ ), residual cohesion ( $c_r$ ), initial friction angle ( $\phi_i$ ), mobilized friction angle ( $\phi_m$ ), tensile strength ( $\sigma_t$ ), dilation angle ( $\psi$ ), cohesion critical strain ( $e_c^{ps}$ ), and friction angle critical strain ( $e_\phi^{ps}$ ). The tensile strength and peak cohesion were varied simultaneously as they are typically considered to be correlated parameters (Hoek and Brown, 2018). The ratio  $\sigma_t/\sigma_{UCS} = 0.12$  is kept constant when the peak cohesion was changed. The selection of appropriate initial and variation ranges for these parameters is given by Walton (2019) based on case studies and theoretical analysis.

For the DISL approach, the parameters varied were  $m_p$ ,  $m_r$ ,  $s_p$ ,  $s_r$ ,  $\psi$ , and  $e_{crit}^{ps}$ . While there is no direct guidance in the literature to vary these parameters, the methodology used was similar to that of the CWFS approach. The parameters were varied within a reasonable range that might be used for design. The main criterion followed was that the failure envelope should remain as proposed by Diederichs (2007) where at low confinement there was strength reduction and at high confinement, there was strength increase.

### 3.7.2 CWFS Strength Parameters Sensitivity Analysis

An SA on the dilation angle of rock was conducted by Zhao and Cai (2010). They concluded that the dilation angle should be lower than the peak or mobilized friction angle to have a non-associated flow rule. For this study, the friction angle is  $48^\circ$ . The variation of  $\psi$  was from

0° to 20°, with the benchmark being 30°. Figure 3-12 shows the failure profiles and Table 3-6 is the summary and characterization of such profiles. At a dilation angle of 0° the failure was uncontrolled and there is no meaningful profile characterization using the measures discussed in Section 3. At a  $\psi \geq 10^\circ$  the failure was controlled and can be characterized. The main effect of  $\psi$  was in the resulting angle of failure, with little effect on  $d_f$ . The  $\psi$  and angle of failure have a positive correlation, as one increases so does the other. The dilation angle is a parameter that correlates to the volumetric expansion of rock after the onset of failure; therefore, at higher angles, the volumetric expansion in the tangential direction increases creating failure in adjacent zones. The effects shown here gave an initial indication of the importance of a judicious selection of  $\psi$  when using the CWFS approach.



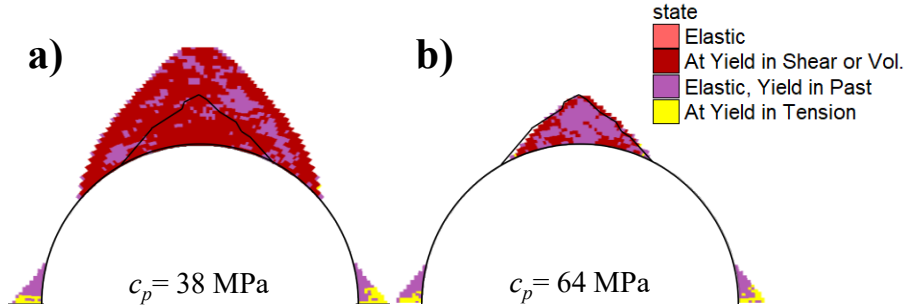
**Figure 3-12 Influence of  $\psi$  on the failure profile in the CWFS approach a)  $\psi = 0^\circ$  b)  $\psi = 10^\circ$  c)  $\psi = 20^\circ$**

**Table 3-6 Influence of  $\psi$  on the failure profile characteristics in the CWFS model**

$\psi$ (°)	Controlled Failure	$d_f$ (m)	Angle of Failure (°)	Area of Failure (m <sup>2</sup> )	Shape of Failure
0	No	NA	NA	NA	NA
10	Yes	0.67	41	0.54	v-notch
20	Yes	0.70	55	0.75	v-notch
30	Yes	0.77	74	1.1	v-notch

According to Walton (2019), the  $c_p$  of a brittle rock should be between 30% and 50% of the in-situ  $\sigma_{UCS}$ . The range correlates to the crack initiation threshold ( $\sigma_{ci}$ ), observed in different rock types. It is also correlated to the unconfined stress at which cohesion loss begins. Hajiabdolmajid, et al. (2002) suggested a  $\sigma_{ci}$  of 128 MPa, which they called in-situ  $\sigma_{UCS}$ . Using these two facts the selected values were 38 MPa and 64 MPa, corresponding to 30 and 50% respectively. The benchmark value was 50 MPa, which corresponds to 39% of the in-situ  $\sigma_{UCS}$ . The  $\sigma_t$  was varied with the  $c$  keeping the ration  $\sigma_t/\sigma_{UCS}$  constant, with 7.6 MPa at the lower  $c$  and 12.8 MPa at the higher  $c$  Figure 3-13 shows the resulting failure

profiles overlayed to the actual failure profile with different  $c_p$ . The failure characterization values are summarized in Table 3-7. Using 64 MPa for peak cohesion gave a profile almost identical to that of the MBE case, all measures were within 1% of the field observation at the MBE. The lower bound for  $c_p$  overestimates the failure profile. This value would imply a low  $\sigma_{ci}$  threshold. The correlation between  $c_p$  and the failure profile is significant and has a large effect on the results.



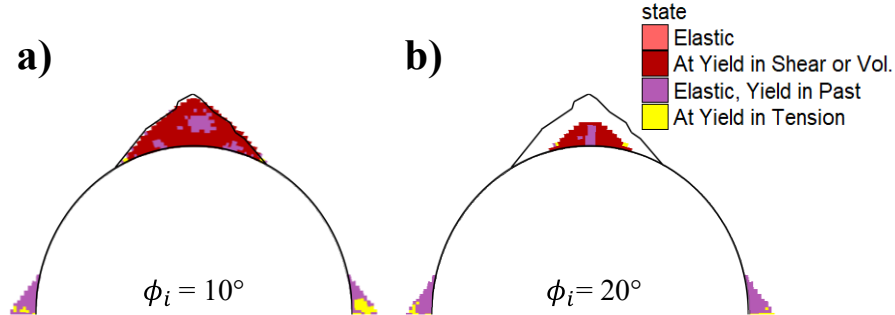
**Figure 3-13 Influence of  $c_p$  on the failure profile in the CWFS approach given a)  $c_p = 38$  MPa b)  $c_p = 64$  MPa**

**Table 3-7 Influence of  $c_p$  on the failure profile characteristics in the CWFS model**

$c_p$ (MPa)	Controlled Failure	$d_f$ (m)	Angle of Failure ( $^\circ$ )	Area of Failure ( $m^2$ )	Shape of Failure
38	Yes	1.1	100	1.9	v-notch
50	Yes	0.77	74	1.1	v-notch
64	Yes	0.53	48	0.46	v-notch

The initial friction angle is suggested to vary from  $0^\circ$  and  $20^\circ$  (Walton, 2019). The lower the friction angle the more brittle the rock. Before failure initiates at the  $\sigma_{ci}$  threshold, the strength of the rock mass is fully dominated by cohesive strength, with little to no impact on the frictional strength, as there are no sliding fracture surfaces present. This  $\phi_i$  of the rock mass is linked to the rock type and the existence of micro-defects and cracks in the rock mass. The more defects, the more frictional the rock is prior to crack initiation. Walton (2019) suggests that crystalline rocks such as LdB granite have a  $0^\circ$  friction angle for modelling. Figure 3-14a is the failure profile for  $\phi_i = 10^\circ$  and Figure 3-14b for  $\phi_i = 20^\circ$ . The benchmark scenario had a  $\phi_i = 0^\circ$ . The summary of the failure characterization is in Table 3-8. With  $\phi_i = 10^\circ$ , a fairly accurate profile was achieved, while using  $\phi_i = 20^\circ$  severely underestimated the failure. This range of values gave very distinct profiles; therefore,  $\phi_i$  is an important parameter to calibrate when using CWFS. Such a significant impact can also be

visualized by the increase in the peak failure envelope and the increase in the rock mass  $\sigma_{UCS}$ . At  $0^\circ$  initial friction angle the  $\sigma_{UCS}$  of the rock mass is 100 MPa while increasing it to  $20^\circ$  increases the  $\sigma_{UCS}$  to 140 MPa; a 40% increase.



**Figure 3-14 Influence of  $\phi_i$  on the failure profile in the CWFS approach a)  $\phi_i = 10^\circ$  b)  $\phi_i = 20^\circ$**

**Table 3-8 Influence of  $\phi_i$  on the failure profile characteristics in the CWFS model**

$\phi_i$ ( $^\circ$ )	Controlled Failure	$d_f$ (m)	Angle of Failure ( $^\circ$ )	Area of Failure ( $m^2$ )	Shape of Failure
0	Yes	0.77	74	1.1	v-notch
10	Yes	0.46	53	0.47	Transition
20	Yes	0.21	29	0.15	Semi-Circle

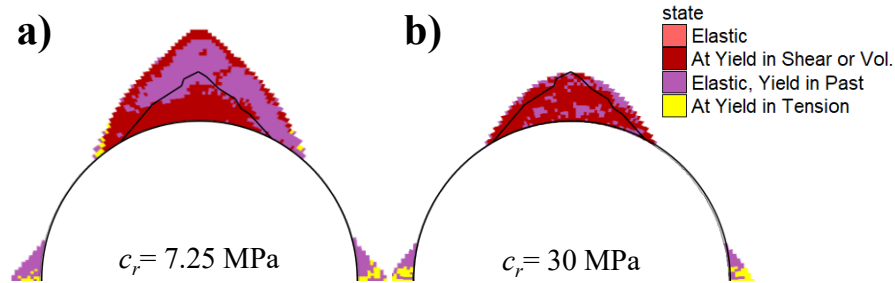
The  $c_r$  is possibly the hardest value to define for the CWFS approach. Physically, the meaning of residual cohesion is difficult to conceptualize (Walton, 2019). In loose, highly fractured rock, this cohesion component between open cracks is zero, yet there is substantial cohesion within the intact rock pieces. The residual cohesion is equivalent to the concept of rock “bridges” between the fractures. Walton (2019) suggested a correlation between  $c_p$  and  $c_r$ , according to the following formula.

$$c_r = -0.46 + 0.76 \times c_p \quad (3-6)$$

This correlation is empirical and weak with an  $R^2$  of 0.77 (Walton, 2019). In the URL scenario, the value for  $c_r$  is 15 MPa, while the  $c_p$  is 50 MPa and is not within the results of Equation (3-6). Therefore, in this study, the values used were half the residual cohesion suggested by Hajiabdolmajid, et al. (2002) for the low end and double for the high end. The values picked were 7.25 MPa and 30 MPa. Figure 3-15 and Table 3-9 are the profiles and the characterization respectively. When using a low cohesion, the depth of failure was significantly overestimated — up to twice the actual depth of failure. Yet, increasing the



cohesion by double did not reduce the  $d_f$  by half. This suggests that underestimating  $c_r$  has more detrimental effects on  $d_f$  prediction than does overestimating it.

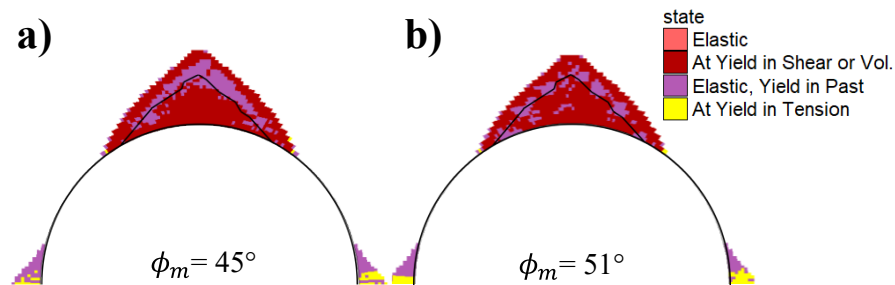


**Figure 3-15 Influence of  $c_r$  on the failure profile in the CWFS approach**  
a)  $c_r = 7.25$  MPa b)  $c_r = 30$  MPa

**Table 3-9 Influence of  $c_r$  on the failure profile characteristics in the CWFS model**

$c_r$ (MPa)	Controlled Failure	$d_f$ (m)	Angle of Failure ( $^\circ$ )	Area of Failure ( $m^2$ )	Shape of Failure
7.25	Yes	0.95	81	1.4	v-notch
15	Yes	0.77	74	1.1	v-notch
30	Yes	0.49	63	0.69	Semi-Circle

The  $\phi_m$  is dependent on the suggested spalling limit (Kaiser et al. 2000) based on the fundamental work by Hoek (1968). This limit for crystalline rocks is around a stress ratio  $\sigma_1/\sigma_3$  of 5 to 20 which corresponds to a  $\phi_m$  of  $45^\circ$  to  $60^\circ$  (Walton, 2019). The brittleness and homogeneity of the rock allow for its approximation. The LdB granite at the MBE is homogeneous and crystalline, an appropriate range for this rock is  $45^\circ$  to  $51^\circ$ , the original  $\phi_m$  being  $48^\circ$ . The results of the SA are shown in Figure 3-16 and Table 3-10. As the range was fairly small, there was minimal impact on the results. Both of these models gave results similar to the ones for the benchmark model. The selection of this parameter does not change the measures of failure significantly.

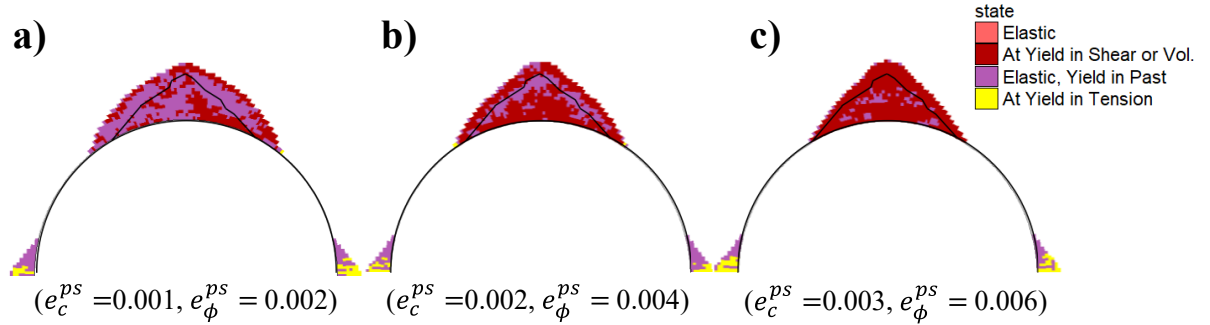


**Figure 3-16 Influence of  $\phi_m$  on the failure profile in the CWFS approach**  
a)  $\phi_m = 45^\circ$   
b)  $\phi_m = 51^\circ$

**Table 3-10 Influence of  $\phi_m$  on the failure profile characteristics in the CWFS model**

$\phi_m$ (°)	Controlled Failure	$d_f$ (m)	Angle of Failure (°)	Area of Failure (m <sup>2</sup> )	Shape of Failure
45	Yes	0.77	74	1.04	v-notch
48	Yes	0.77	74	1.1	v-notch
51	Yes	0.77	74	0.95	v-notch

The  $e_{crit}^{ps}$  has been argued to be a true physical property of the material (Martin, 1997). It does not depend on loading or system conditions; therefore, it can be directly applied from experimental measurements into modelling (Hajiabdolmajid, 2002). To get a more representative critical strain value, laboratory experiments to determine such a parameter should be conducted. Rock type and brittleness can be used to provide guidance in the selection of this parameter. In general,  $e_c^{ps}$  varies between 0.001 and 0.003; weaker rocks have higher  $e_c^{ps}$ . The  $e_\phi^{ps}$  is dependent on the  $e_c^{ps}$ , the  $\phi_i$ , and the brittleness of the rock. For crystalline rocks, such as LdB, the recommended ratio of  $e_\phi^{ps}/e_c^{ps}$  is 2 (Walton, 2019). For this study, the values taken for  $(e_\phi^{ps}, e_c^{ps})$  are (0.001, 0.002), (0.002, 0.004), and (0.003, 0.006). Worth noting is that the values suggested by Hajiabdolmajid (2002) have a higher ratio than 2, based on the authors' calibration to the MBE field observations. Figure 3-17 and Table 3-11 summarize the three conditions studied compared to the benchmark case. The impact of critical strain resulted in a change of shape but no change in  $d_f$ . At lower values, the shape was semi-circular with the higher values giving a v-shape notch. The angle of failure was also affected by the lower critical strain giving a larger angle of failure and as a consequence a larger area of failure. While there were some differences in the results, none of them led to an unreasonable profile. All values proposed by Walton (2019) for the critical strain can be used to model this type of scenario yielding reasonable results.



**Figure 3-17 Influence of  $e_c^{ps}$  and  $e_\phi^{ps}$  on the failure profile in the CWFS approach a) ( $e_c^{ps} = 0.001, e_\phi^{ps} = 0.002$ ) b) ( $e_c^{ps} = 0.002, e_\phi^{ps} = 0.004$ ) c) ( $e_c^{ps} = 0.003, e_\phi^{ps} = 0.006$ )**

**Table 3-11 Influence of  $e_c^{ps}$  and  $e_\phi^{ps}$  on the failure profile characteristics in the CWFS model**

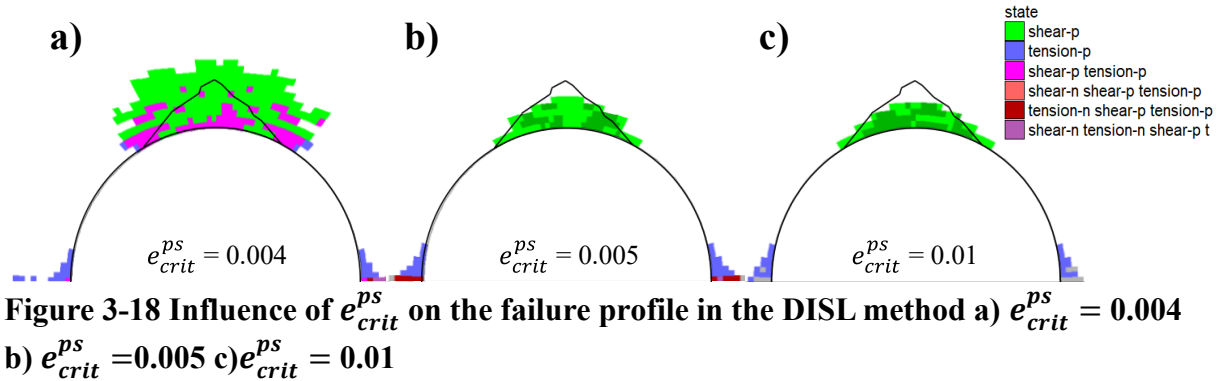
$e_c^{ps}$	$e_\phi^{ps}$	Controlled Failure	$d_f$ (m)	Angle of Failure (°)	Area of Failure (m <sup>2</sup> )	Shape of Failure
0.001	0.002	Yes	0.60	79	0.95	Semicircle
0.002	0.004	Yes	0.63	69	0.84	Transition
0.002	0.005	Yes	0.77	74	1.1	v-notch
0.003	0.006	Yes	0.67	61	0.75	v-notch

### 3.7.3 DISL Sensitivity Analysis

Performing sensitivity analysis with *FLAC* is not as systematic and straightforward for the DISL approach as it was for the CWFS approach, because it was developed using *Phase2* and that software's constitutive models. While for CWFS, Walton (2019) compiled a detailed list of possible values and guidance for the selection of parameters using analytical and empirical reasons, there is no such guidance, to the knowledge of the authors, in the literature for the DISL approach. Equation (3-5) and (3-6) give guidance on the peak values that can be used, but the variation and uncertainty of  $\sigma_{UCS}$  and  $\sigma_T$  are not large enough to give a meaningful range of  $s_p$  and  $m_p$ . Some values in the DISL approach should not be altered significantly, such as the  $s_r$ , which should be close to zero to be able to approximate the s-shape failure envelope and to demonstrate the total loss of cohesion after the  $\sigma_{ci}$  is reached. Yet, a similar SA study can be developed as in the previous section, in which the parameters are varied within a range that can reasonably be used for design. For this study a simple interpretation of the failure profile is of interest; therefore, only yielded elements were considered for its characterization. The results of this investigation can be interpreted

differently if the suggestions of Perras and Diederichs (2016) are followed. Yet, this adds a level of subjectivity beyond the interest of this paper.

The first parameter for SA was the critical strain for a *FLAC* implementation of the approach. As discussed in Section 5.1, Diederichs (2007) used *RS2* that did not utilize  $e_{crit}^{ps}$  as a parameter in *DISL*. Therefore, the selection of this value has increased uncertainty. As a benchmark, 0.001 was used for  $s$ ,  $m$ , and  $a$  giving an uncontrolled profile. It can be increased until a controlled profile is found. The minimum critical strain at which the failure is controlled is 0.004 (0.4%). It gives an unrealistic square failure profile, as seen in Figure 3-18a. To do an adequate SA, the strain was then increased to 0.01. However, this last value deviated substantially from the very brittle nature suggested by the instantaneous nature of *RS2*. All values of strain that gave a controlled profile severely underestimated the failure profile to up to 50% of the true value. Figure 3-18 and Table 3-12 are the summaries of the results for this parameter's SA.



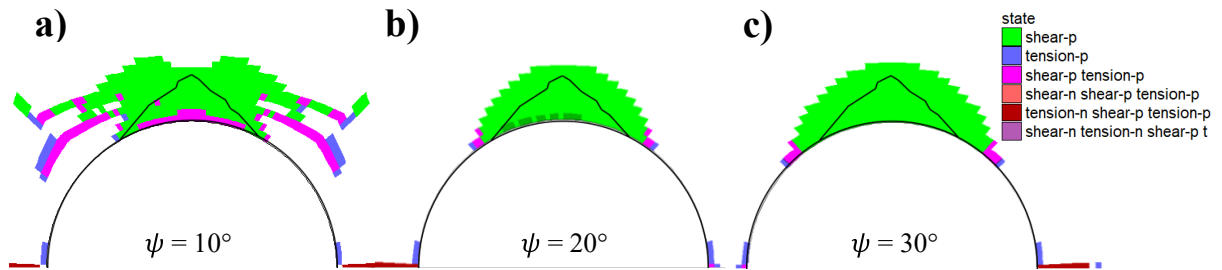
**Figure 3-18 Influence of  $e_{crit}^{ps}$  on the failure profile in the DISL method a)  $e_{crit}^{ps} = 0.004$  b)  $e_{crit}^{ps} = 0.005$  c)  $e_{crit}^{ps} = 0.01$**

**Table 3-12 Influence of  $e_{crit}^{ps}$  on the failure profile characteristics in the DISL model**

$e_{crit}^{ps}$	Controlled Failure	$d_f$ (m)	Angle of Failure (°)	Area of Failure (m <sup>2</sup> )	Shape of Failure
0.001	No	NA	NA	NA	NA
0.004	Yes	0.77	64	1.62	Square
0.005	Yes	0.35	59	0.45	Semicircle
0.01	Yes	0.28	62	0.39	Semicircle

The dilation angle also has a significant effect on the simulated failure profile. Diederichs (2007) suggested 0° for the simulation of the roof. By increasing it to similar values as used in the CWFS SA a controlled failure profile is achieved. The values used for this SA are 10°, 20°, and 30°. At a dilation angle of 10°, the failure profile was still uncontrolled, similar to

the benchmark modelling scenario. At dilation angles of 20° and 30°, the failure becomes controlled. Yet, both values highly overestimated the failure profile and gave a semi-circular shape of failure rather than the expected v-notch. Figure 3-19 shows the three profiles and Table 3-13 is the summary results of this SA. These results indicated that  $\psi$  is a critical parameter in achieving controlled failure in brittle rock modelling.



**Figure 3-19 Influence of  $\psi$  on the failure profile in the DISL approach a)  $\psi = 10^\circ$  b)  $\psi = 20^\circ$  c)  $\psi = 30^\circ$**

**Table 3-13 Influence of  $\psi$  on the failure profile characteristics in the DISL model**

$\psi$ (°)	Controlled Failure	$d_f$ (m)	Angle of Failure (°)	Area of Failure (m <sup>2</sup> )	Shape of Failure
0	No	NA	NA	NA	NA
10	No	NA	NA	NA	NA
20	Yes	0.63	76	1.15	Semicircle
30	Yes	0.7	93	1.48	Semicircle

SA was done on the Hoek-Brown parameters by varying each one until a reasonable failure profile was achieved. The parameters were  $s_p$ ,  $s_r$ ,  $m_p$ , and  $m_r$ . The  $s_p$  took the values of 0.066, 0.02, and 0.1: none of these values achieved a controlled failure. The  $s_r$  were 0.005, 0.01, and 0.1: the latter value gave a stable failure profile (Figure 3-20). This  $s_r$  of 0.1 is larger than the  $s_p$  suggesting an increase in the strength after failure even at low confinement. When  $s_r$  is larger than  $s_p$  the model is no longer consistent with the DISL approach, as it implies a strength increase at low confinement. The  $m_p$  was changed to 0 and 2, yet neither yielded a stable profile. A larger increase of  $m_p$  would suggest more frictional contribution prior to crack initiation; therefore, it was not increased any further. Lastly,  $m_r$  was increased to 7, 8, 9, and 10, with only the last two having a stable failure profile (Figure 3-21). Perras and Diederichs (2016) suggested a range of between 6 and 12 for this value. Increasing  $m_r$  from its original 6 to 9 gives a reasonable failure profile. Table 3-14 is a summary of all the

SA conducted on the Hoek-Brown parameters and a summary of the failure profile characteristics compared to the benchmark modelling case using *FLAC*.

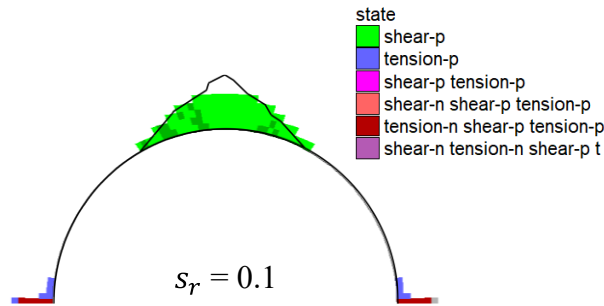


Figure 3-20 Influence of  $s_r = 0.1$  on the failure profile in the DISL approach

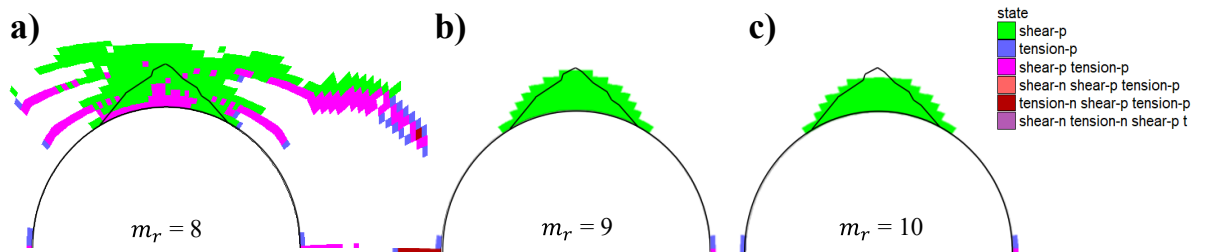


Figure 3-21 Influence of  $m_r$  on the failure profile in the DISL approach a)  $m_r = 8$  b)  $m_r = 9$  c)  $m_r = 10$

Table 3-14 Influence of Hoek-Brown parameters on the failure profile characteristics in the DISL model

HB Parameter	HB Parameter Value	Controlled Failure	$d_f$ (m)	Angle of Failure (°)	Area of Failure (m <sup>2</sup> )	Shape of Failure
Benchmark	NA	No	NA	NA	NA	NA
$s_p$	0.02	No	NA	NA	NA	NA
	0.066	No	NA	NA	NA	NA
	0.1	No	NA	NA	NA	NA
$s_r$	0.005	No	NA	NA	NA	NA
	0.01	No	NA	NA	NA	NA
	0.1	Yes	0.35	54	0.47	Semicircle
$m_p$	0	No	NA	NA	NA	NA
	2	No	NA	NA	NA	NA
$m_r$	7	No	NA	NA	NA	NA
	8	No	NA	NA	NA	NA
	9	Yes	0.49	64	0.69	Semicircle
	10	Yes	0.42	64	0.65	Semicircle

### 3.8 SENSITIVITY ANALYSIS OF HYPOTHETICAL IN SITU STRESS MAGNITUDES

Another set of parameters that can be varied to understand the robustness of the approaches is the in situ stress magnitude. At different magnitudes of stress, if the approach is robust, the results should follow the empirical observation. Both CWFS and DISL were tested to see how they respond to different stress magnitudes and if they follow the expected trends. This investigation deviated from the strength parameters SA as it is purely hypothetical, intended to create a set of “observations” for further analysis of both approaches.

#### 3.8.1 Hypothetical Stress Scenario Sensitivity Analysis Methodology

The MBE at the URL is a single tunnel performance observation within a single stress regime. To use these modelling tools for design, it must be understood how they would perform under a wider range of conditions to evaluate model robustness. One option is to look at multiple different case studies and model them; however, information of this type is limited. A more practical approach is to use the empirical equation suggested by Martin et al. (1999) that relates  $d_f$  to in situ stress and strength as a proxy for case histories. The suggested equation is:

$$\frac{d_f}{a} = 1.25 \frac{\sigma_{max}}{\sigma_{UCS}} - 0.51 \pm 0.1 \quad (3-7)$$

where  $\sigma_{max}$  is the maximum tangential stress calculated elastically, given by (Martin et al., 1999):

$$\sigma_{max} = 3\sigma_1 - \sigma_3 \quad (3-8)$$

The empirical observations and equation were updated by Diederichs et al. (2010). In this update, the authors added more empirical observations to the original database and suggested that  $d_f$  can be better correlated using  $\sigma_{ci}$ .

Different fictitious scenarios were created using the MBE tunnel as a basis by changing the in situ stresses to generate a range of  $\sigma_{max}$ . Then the model predicted  $d_f$  is measured and compared to Equation (3-7). The strength values used for the benchmarks of CWFS and DISL were used for the stress regime investigation. If successful, the approaches should follow the same trend observed by Martin et al. (1999).

There are multiple ways to change  $\sigma_{max}$ . It can either be done by changing the  $\sigma_1$  and keeping  $\sigma_3$  at 11 MPa to generate different  $\sigma_{max}$  scenarios. Alternatively, the ratio  $k$  is given by:

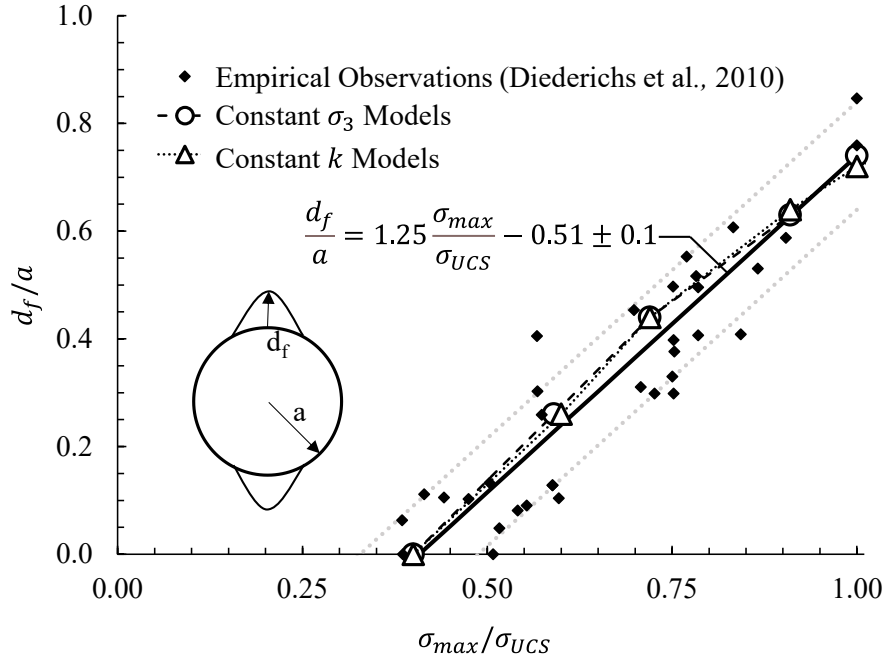
$$k = \frac{\sigma_1}{\sigma_3} \quad (3-9)$$

can be kept constant. This would involve both  $\sigma_1$  and  $\sigma_3$  being changed simultaneously increasing the  $\sigma_{max}$  as a result. In this study, both procedures were explored. A similar investigation was done by Perras and Diederichs (2016) for the DISL approach in *RS2* to determine the different stress thresholds at different stress conditions.

### 3.8.2 CWFS Results

The first set of models was done by keeping  $\sigma_3$  constant and changing  $\sigma_1$ . The ranges of failure according to Equation (3-7) and the empirical observations from Martin (1997) give a ratio of  $\sigma_{max}/\sigma_{UCS}$  between 0.4 and 1. Therefore, the selected values for  $\sigma_1$  were 35 to 90 MPa with a constant  $\sigma_3$  of 11 MPa, resulting in a changing  $k$  ratio. The CWFS parameters used were those provided in Table 3-3. All of these models produced controlled failure. The  $d_f$  for the different models are shown along with Equation (3-7) and the case studies by Martin (1997) in Figure 3-22 . The next set of models uses a constant  $k$ . In the URL MBE, the  $k$  ratio is around 5.5. The range remained the same for the  $\sigma_{max}/\sigma_{UCS}$  as previously mentioned. The stress values given as pairs of in situ stresses ( $\sigma_1, \sigma_3$ ) ranged from (33.4, 6.1) to (82.9, 15.2). For these stress value ranges the strength parameters used were the original CWFS values from Table 3-3. The results are plotted in Figure 3-22 and show an agreement with both the empirical equation for the depth of failure and the different empirical observations.





**Figure 3-22 Stress SA for CWFS models at different stress regimes for both constant  $\sigma_3$  and constant  $k$  compared to the  $d_f$  equations proposed by Martin et al. (1999) and case scenarios observations reported by Diederichs et al. (2010)**

The  $d_f$  follows the trends observed in the field at different stress scenarios. The models show agreement with the empirical equation showing the robustness of the approach. Both stress variation approaches gave almost identical results when the  $\sigma_{max}/\sigma_{UCS}$  is the same. This behaviour shows that the CWFS approach reproduces the empirical observations under different stress conditions for the same rock model parameters. There is no need for special calibration of the rock strength at different stress magnitudes. There are no empirical observations after  $\sigma_{max}/\sigma_{UCS} = 1$ , meaning that extrapolating Equation (3-7) beyond this range is inappropriate. When the ratio is greater than 1, the conditions transition from brittle failure to potential rockburst conditions (Kaiser et al., 2000). The approach presented in this study is not suitable for the dynamic rockburst behaviour associated with those stress levels.

### 3.8.3 DISL Results

Applying the same in situ stress sensitivity methodology to the DISL approach is more involved. It was established that using the values suggested by Diederichs (2007), there was uncontrolled zone failure and the  $d_f$  cannot be measured, by using the yielded zone interpretation rather than the interpretation suggested by Perras and Diederichs (2016). Using

the benchmark strength values resulted in uncontrolled failure at all stress regimes. Therefore, the  $d_f$  could not be readily compared to Equation (3-7) without a more in-depth model interpretation.

In Section 6.3., it was shown that the dilation angle has a large impact on model results. According to the SA, the dilation angle is a key parameter for the use of the DISL approach. It was found that dilation angles of 20° and 30° produce reasonable failure profiles in the benchmark study. The hypothetical stress scenario SA was run using the proposed original parameters, but with the modified  $\psi$ . The scenarios were conducted by keeping the  $\sigma_3$  constant at 11 MPa and changing the  $\sigma_1$  to get a change in the  $\sigma_{max}$ . The results showed that even using the “calibrated” dilation angles, the DISL approach is still sensitive to stress regimes. At a  $\sigma_{max}/\sigma_{UCS}$  higher than 0.8 the models no longer produce controlled failure. At higher ratios, the zone failure pattern was uncontrolled, leading to harder-to-interpret results.

Alternatively, it was shown that if an  $m_r$  of 9 is used, and all other values are kept the same as in Table 3-4, at the MBE stress regime the profile was controlled. The same stress SA was done using these new revised strength parameters ( $m_r = 9$ , and benchmark). This investigation yielded the same results as with the modified dilation angle SA where, after a certain stress threshold of  $\sigma_{max}/\sigma_{UCS} = 0.8$ , the failure profile cannot be categorized using the yielded zone approach. What this entails is that not only is the DISL approach sensitive to the strength parameters as seen in the previous section, but even after calibration, it is sensitive to the stress regime in which it was calibrated. To make use of the DISL approach in *FLAC* the calibration needs to take into account the stress regime. This is an additional complication, as often design projects have an unknown or estimated stress regime. If the strength of the rock is calibrated to a certain regime, but the in situ conditions turn out to be different, a new calibration of the strength parameters is needed.

### 3.9 DISCUSSION

For both brittle rock failure modelling methods, each of the variables has a unique effect on the results of the predicted failure. The dilation angle has a similar effect on CWFS as it does on the DISL approach. Having a low dilation angle makes the model more prone to uncontrollable failure. For brittle rock, it is recommended to use a dilation angle similar to or equal to the initial friction angle of the rock (Zhao and Cai, 2010). A dilation of 0° means

that there is no volumetric expansion and associated confinement stress increase in the rock as it fails with the implication that the mesh zones fail with no confinement due to a dilational tendency. This allows for the zone failure to cause a sort of “chain reaction” causing uncontrolled failure. The  $\psi$  should be high enough to create a controlled zone failure. After controlled failure is achieved the dilation angle has an effect on the angle of failure, with little-to-no effect to  $d_f$ . This is due to the increase in volume in the direction of minimum compressive stress (radial to the excavation). Similar observations with confinement levels were made by Kaiser et al. (2000) who suggested that support design for brittle tunnels is selected depending on the confinement the support can generate. When using either approach for design or performance prediction, great care needs to be applied to doing an SA on the dilation angle.

For the CWFS approach, the residual and mobilized values have a small effect on the failure profile. The range of values of  $\phi_m$  does not change the ultimate profile. While it appears from Figure 3-15 that the  $c_r$  has a large effect, this is only because the values varied substantially, from 50% to 200% of the original, an extremely large range. So, comparatively, the effect is correspondingly proportionate to the input. Similar observations were made by Eldelbro (2010) and Renani and Martin (2018), where the peak and initial parameters have a larger effect on the ultimate profile as an inverse correlation. By reducing the  $c_p$  by 12 MPa (24%) in the sensitivity study, the depth of failure increased by 0.56 m (100%). Similarly, by increasing the  $\phi_i$ , the depth of failure was reduced substantially. These results again match those presented by Eldelbro (2010) and Renani and Martin (2018). Lastly, the critical strain influences the angle and shape of failure rather than the depth. Smaller critical strains yield a more rounded and wider failure. The larger  $e_c^{PS}$  and  $e_\phi^{PS}$  the sharper and narrower the failure is. Yet, the influence is not overly significant, as all values have similar depth, angle, and area of failure. Therefore, critical strain has a smaller impact on the prediction of failure than most other parameters.

The DISL approach is more sensitive to all input parameters than the CWFS. Slight variations, such as changing the critical strain from 0.003 to 0.004, change the model from uncontrolled to a failure profile smaller than that of the field observations. For most parameters, the values needed to be increased substantially from the suggested for the

benchmark case. The most drastic example of this is increasing  $s_r$  up to 0.1. Doing so suggests that the  $\sigma_{UCS}$  of the rock mass is larger than the initial  $\sigma_{UCS}$ . Having those conditions is no longer consistent with a DISL model. Increasing  $m_r$  substantially results in a controlled zone failure. These adjustments are valid when calibrating a model for an existing tunnel; however, when it comes to design, the selection of these parameters is too sensitive. Furthermore, when a controlled zone failure is achieved via calibration, it is presented with a semicircular shape. The selection of parameters is determined by Equation (3-1) and Equation (3-2) as a single value, which makes finding a range of adequate values challenging. Perras and Diederichs (2016) suggest that the depth of failure should be determined by the distance away from the excavation boundary at which confinement increases from the value at the boundary. This means that  $d_f$  is determined by when the modeled rock mass is able to take confinement, rather than the zone failures. While this was not explored in this study, this new application adds a level of subjectivity to the DISL approach.

### 3.10 CONCLUSION

This study detailed the application of two continuum numerical modelling approaches for assessing the stability of brittle rock around underground excavations using the software *FLAC*. The two approaches explored were the CWFS developed by Hajiabdolmajid et al. (2002) and the DISL proposed by Diederichs (2007). With these tests the application of both approaches using *FLAC* was better understood, particularly the plastic strain dependency of each approach. Then the approaches were applied to the MBE at the URL case study with the current version of *FLAC* to set as benchmarks using the values proposed by the original authors. From there, a sensitivity analysis of all strength parameters was conducted to understand the effect of each parameter on the result given a case scenario. The SA was done following the guidelines suggested by Walton (2019) for the use of the CWFS approach for design. For the DISL approach, the SA was conducted partly using the guidance given by Perras and Diederichs (2016) and keeping parameters within reasonable selection for design. Lastly, to demonstrate how the approaches work for different scenarios, a set of hypothetical cases was developed by changing the stress magnitudes from the base case. This allowed for a comparison of the approaches with multiple observations of other case scenarios presented by Martin et al. (1999). The CWFS is a robust approach that can be used with reasonably

well-understood parameter selection guidelines and can be readily interpreted with relatively objective means. This makes it a good approach for use by capable and qualified rock engineering practitioners who may not necessarily be considered numerical modelling specialists. Following the set of guidelines by Walton (2019) and understanding the effects of each parameter presented in this study helps practitioners to apply the approach for their design scenarios. The DISL approach shows more sensitivity to strength parameters which complicates its interpretation. It can still be feasibly used especially with the *RS2* software, but the user must be aware that to interpret the results there needs to be a fundamental understanding of not only the approach but numerical modelling itself. To better understand the results from the approach, the suggestions by Perras and Diederichs (2016) should be understood first.

The SA conducted addressed the gaps in the literature by analyzing the effects of each *FLAC* model strength input parameter individually. Notably, the selection of the dilation angle has a significant impact on the results for both the CWFS and DISL approach. To achieve a controlled failure profile in both, the dilation angle selected must be greater than  $0^\circ$ . As both approaches are highly dependent on confining stresses, the dilation has a great impact on the results of the numerical models. For the CWFS approach, the parameters that have a large effect on the results of the simulation are the peak strength envelope values. Peak cohesion and initial friction angle dominate the strength of the brittle rock, whereas the residual parameters ( $c_r, \phi_m$ ) have less of an impact on the failure profile produced. The CWFS approach can also reproduce the empirical observation of  $d_f$  at different stress regimes reported by Martin et al. (1999). The DISL approach is more sensitive to all strength parameters as well as the stress regime being modelled. More in-depth knowledge is needed from the numerical modeller to correctly interpret the results of these models. All parameters, selected within reasonable design values, can produce results that require skill to interpret. This does not render the approach invalid; it does complicate its application, especially for construction monitoring stages. For ease of use for practitioners, the CWFS approach is recommended for the design and interpretation of excavation in brittle rock using *FLAC*.

## **CHAPTER 4 - APPLICATION OF THE CWFS METHOD IN FLAC2D TO MODEL BRITTLE FAILURE AROUND THE QIREHATAER DIVERSION TUNNEL**

Luis F. Gomez de Alba, Andrew Corkum & Navid Bahrani

Extended abstract submitted and published to the 2024 Itasca International Symposium

The symposium proceedings are available at:

<https://www.itascainternational.com/events/6th-itasca-symposium-on-applied-numerical-modeling>

This abstract was presented June 5th, 2024 at the 2024 Itasca International Symposium in Toronto, Canada

### **4.1 INTRODUCTION**

The simulation of failure around underground excavations in hard brittle rocks using continuum numerical methods remains a challenge. Many authors have proposed various techniques to simulate spalling failure (Martin 1997, Hajiabdolmajid et al. 2002, Hajiabdolmajid et al. 2003, Diederichs 2007). Amongst them, Hajiabdolmajid et al. (2002) suggested the cohesion weakening friction strengthening (CWFS) method. This method proposes that the failure of brittle rocks is dominated by the loss of cohesion as new fractures are developed, with an increase in friction due to sliding and interlocking. This process is often described as non-simultaneous, with the cohesion loss being a faster process than the friction strengthening. The CWFS method was originally proposed and developed based on the Mine-by Experiment (MBE) tunnel at the Underground Research Laboratory (URL). This method was developed from the laboratory experiments conducted by Martin and Chandler (1994) where they found that brittle rock undergoes cohesion loss and friction increase during uniaxial compressive strength test. Walton (2019) expanded the CWFS method by proposing a set of guidelines for selecting the input parameters. Such guidelines provide an initial step towards the use of the CWFS, although some model calibration may still be necessary when using them. This study explores the use of the CWFS method in *FLAC2D* for the analysis of brittle failure around the Qirehataer Diversion Tunnel in western China, utilizing Walton's (2019) CWFS modeling guidelines. Following these guidelines and adjusting the input parameters, the simulation results are compared with field observations of the depth of failure to assess the effectiveness of the CWFS method in *FLAC2D*.

## 4.2 BACKGROUND

The Qirehataer Diversion Tunnel is a water diversion tunnel for a hydropower station located in the Kunlun Mountains in western China. The tunnel was excavated in Gneissic Granite using the drill and blast method between 2009 and 2014 (Zhao, 2017). The length of the tunnel is approximately 16 km with depths varying from 68 to 1720 m, with 21% having an overburden  $> 1000$  m. The main diversion tunnel has a D-shape cross-section measuring 5.75 m in height and 5.30 m in width. The granite has an average peak strength ( $\sigma_{UCS}$ ) of around 100 MPa, a crack initiation stress ( $\sigma_{ci}$ ) of 45 MPa, and an approximate tensile strength ( $T$ ) of 8 MPa. The elastic properties of this rock are  $E = 20$  GPa and  $\nu = 0.21$ . The quality of the rock is good to excellent, with a GSI range of 80 to 85. This makes the rock ‘massive’ and brittle, which suggests if the rock fails it would be by spalling (Zhao, 2022). Different stress measurement methods such as hydraulic fracturing and overcoring, were employed to determine the in situ state of stresses. At a depth of 814 m, using the overcoring method, the stresses were measured as follows:  $\sigma_1 = 28$  MPa with a plunge of  $19^\circ$ ,  $\sigma_2 = 19$  MPa with a plunge of  $70^\circ$ , and  $\sigma_3 = 18$  MPa with a plunge of  $0^\circ$ . The diversion tunnel was constructed approximately parallel to  $\sigma_3$  (Zhao et al. 2017).

During the construction of the tunnel, 29 unique spalling occurrences were reported (Zhao et al. 2017). These cases varied in severity, ranging from minor spalling to severe spalling. Failure was primarily observed at the shoulders of the excavation where the tangential stresses are the highest. Out of these 29 cases, 12 were classified as minor spalling, 13 as intermediate sidewall spalling, and 4 as severe spalling. Zhao, et al. (2017) reported that most cases of spalling from minor to major occurred near the #4 adit of the diversion tunnel, where the overburden ranges from 800 m to  $> 1000$  m. Therefore, it is expected that all spalling cases occurred at a similar stress magnitude. This study focuses on the severe spalling cases. They presented depths of failure ( $d_f$ ) between 0.5 and 1 m from the planned excavation boundary (Zhao et al., 2017). Zhao et al. (2022) provided a profile of severe spalling shown in Figure 4-1. To match the profiles presented by the authors, the strength parameters are adjusted until an adequate profile is simulated.

### 4.3 METHODOLOGY

Hajiabdolmajid et al. (2002) introduced the CWFS method as a means to model brittle failure. Multiple parameters are required to use this method; peak cohesion ( $c_p$ ), initial friction angle ( $\phi_i$ ), residual cohesion ( $c_r$ ), mobilized friction ( $\phi_m$ ), dilation ( $\psi$ ), cohesion critical plastic strain ( $e_c^{ps}$ ), and friction critical plastic strain ( $e_\phi^{ps}$ ). To develop this method, Hajiabdolmajid et al. (2002) used the MBE tunnel as a case study by calibrating the model to match the failure profile to that observed in the field.

To expand on the CWFS, Walton (2019) proposed a set of guidelines. These guidelines were derived from a compilation of successful applications of the method found in the literature. The formulas provided as guidelines are the result of linear regressions of CWFS input parameters compared to the strength of the rock in case studies that have successfully used the CWFS method. Their guidelines provide an initial estimate of the appropriate parameter values for brittle failure simulation around underground excavations in hard brittle rocks. The guidelines are relationships between the properties required for the CWFS, the strength of the intact rock, and the geological characteristics of the rock. The value of  $c_p$  is determined using the following equation:

$$c_p = \frac{\sigma_{In-situ} \times (1 - \sin \phi_i)}{2 \times \cos \phi_i} \quad (4-1)$$

where  $\sigma_{In-situ}$  is the in situ unconfined compressive strength of the rock. It has been suggested that this parameter is the  $\sigma_{ci}$  measured in laboratory experiments (Diederichs, 2007). The selection of  $\phi_i$  depends on the strength and the brittleness of the rock. The suggested range is  $0^\circ$  to  $20^\circ$ , with stronger rock (high  $\sigma_{UCS}$ ) having a lower  $\phi_i$  i.e.,  $0^\circ$ . The  $c_r$  is suggested to be dependent on  $c_p$  according to:

$$c_r = -0.46 \text{ MPa} + 0.76 \times c_p \quad (4-2)$$

The value of  $\phi_m$  is determined by the spalling limit of the rock ( $\sigma_1/\sigma_3$ ) which tends to range from 10 to 20, corresponding to a friction angle range of  $45^\circ$  to  $65^\circ$ . It can also be estimated using the following equation:

$$\phi_m = 20^\circ + 1.33 m_i \quad (4-3)$$

where  $m_i$  is a Hoek-Brown constant. The critical plastic strains depend on the brittleness of the rock. The range of  $e_c^{ps}$  is 0.001 – 0.003 with  $e_\phi^{ps}/e_c^{ps}$  being either 1 or 2. Determining the



dilation angle is a complex task. Walton (2019) suggests a mobilized confinement dependent  $\psi$ . For this paper, a mobilized associated flow rule  $\psi$  is used, where  $\psi$  changes at the same rate and values as  $\phi$  ( $\phi_i = \psi_i$ ,  $\phi_m = \psi_m$ , and  $e_\phi^{ps} = e_\psi^{ps}$ ).

Using Equations (4-1), (4-2), and (4-3) as well as some understanding of the rock, the following input parameters were found and later used for initial simulation. These initial input parameters are summarized in Table 4-1.

**Table 4-1 Initial parameter selection for the gneissic granite at the Qirehataer Diversion Tunnel for CWFS modelling.**

<b>Parameter</b>	<b>Peak/Initial</b>	<b>Residual/Mobilized</b>
$c$ (MPa)	20	14
$\phi$ ( $^\circ$ )	10	50
$T$ (MPa)	8	0
$\psi$ ( $^\circ$ )	10	50
$e_c^{ps}$		0.002
$e_\phi^{ps}$		0.004

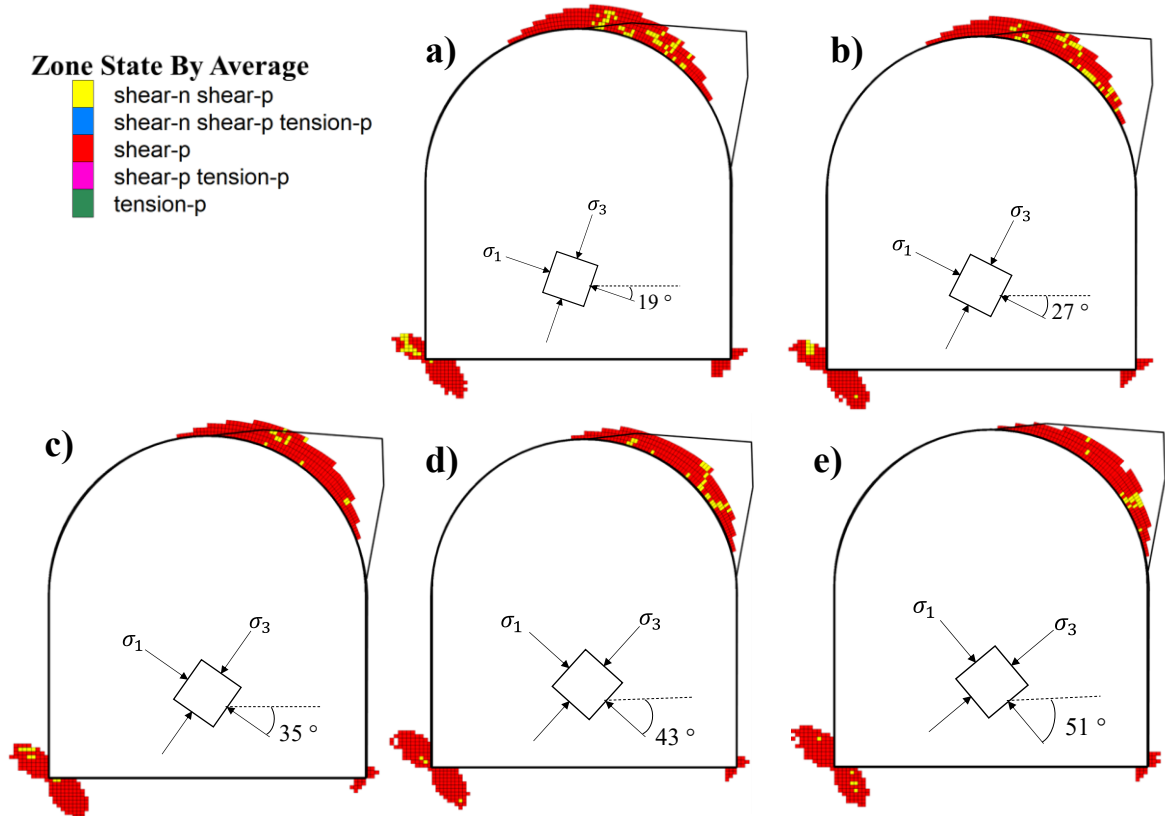
All modeling is conducted using *FLAC2D* 9.0.162 (Itasca, 2023). The zones are divided into two densities. The fine zones, with a size of 5 cm per side, extend 10 m on both sides from the center of the tunnel, while the coarse mesh consists of zones ranging from 10 to 40 cm per side, which extends to the outer boundary 50 m away from the tunnel center in all directions. The model boundary conditions are fixed in all directions. The values from Table 4-1 are adjusted using engineering judgment and sensitivity analysis to capture the best fit for the  $d_f$  and failure shape observed in the field.

The results of stress measurement indicate a maximum stress plunge of approximately  $19^\circ$ . However, the spalling observed in the field shows that the tip of the v-shaped notch is at an angle steeper than expected, given that spalling always occurs at a location where the tangential stress is the highest (Martin 1993, Martin 1997). Therefore, the plunge of  $\sigma_1$  was adjusted to align the simulated failure profile direction with field observations (Zhao, 2022).

#### 4.4 RESULTS

The results obtained using the parameters given in Table 4-1, as shown in Figure 4-1a, underestimate the depth of the v-shaped notch failure observed in the field and do not match the profile. To better replicate the direction of the v-shaped notch, the plunge of  $\sigma_1$  is increased by  $7.5^\circ$  until a match was achieved. This process is illustrated in Figure 4-1, where

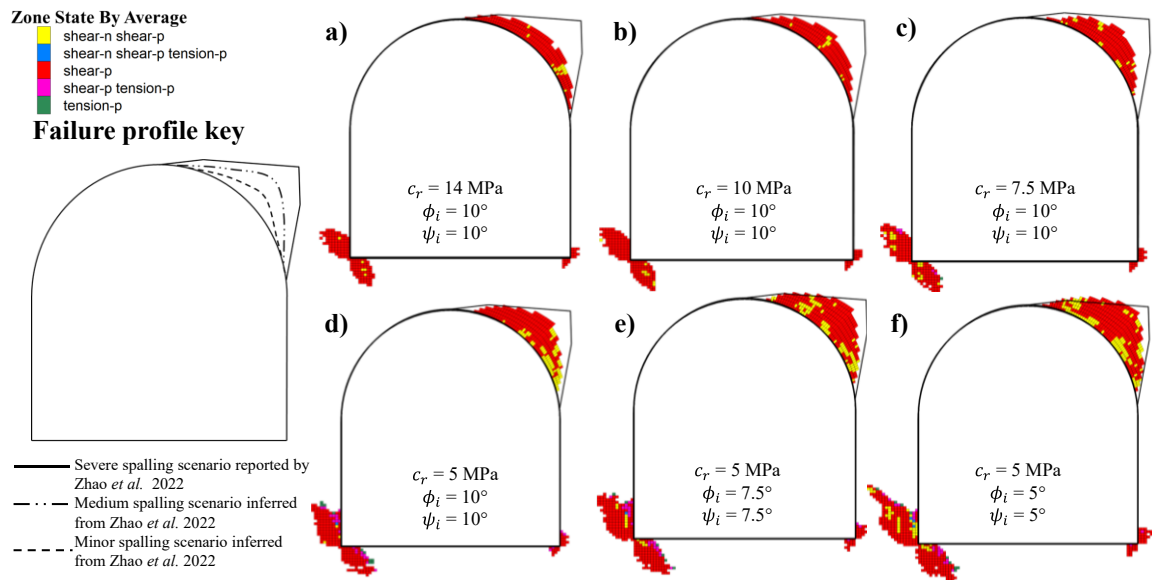
Figure 4-1a is the results from the model at the measured stresses (plunge of 19°) and Figure 4-1e represents the resulting and best-fitting angle (plunge of 51°). This new angle was used for further model calibration.



**Figure 4-1 Results of *FLAC2D* CWFS models using the suggested strength parameters from Table 4-1 shows  $\sigma_1$  plunge angle calibration to obtain the most adequate v-notch direction where the angles used are a) 21°, b) 27°, c) 35°, d) 43°, e) 51°.**

The strength properties provided in Table 4-1 underestimate the profile presented by Zhao et al. (2022). While it did not replicate the worst-case scenario depicted in the profile, these results align with other observed spalling incidents, particularly the 12 minor spalling cases and 13 moderate spalling cases, as shown in the comparative key in Figure 4-2. Back analysis was used to achieve a better agreement with the worst-case scenario profile. There was a reduction in some strength parameters to achieve a deeper  $d_f$ . After multiple iterations, the two parameters modified were the  $c_r$  and  $\phi_i$ . The value of  $c_r$  was reduced to increase the  $d_f$  until it matched the field observations. Then the value of  $\phi_i$  was reduced to further increase  $d_f$  and change the shape of the failure to match the field observations. All other parameters remained the same across iterations. Figure 4-2 shows the process followed for the

calibration, starting with the original parameters (Figure 4-2a) and progressing until an acceptable match was found (Figure 4-2f). Table 4-2 provides the strength values used for the calibrated model. The final  $c_r$  used is 5 MPa. It is a significant reduction from the initial 14 MPa. This initial value is particularly high for fractured rock. The  $c_p/c_r$  ratio after calibration is similar to those used in literature for the MBE tunnel at the URL, which is close to 4 (Hajiabdolmajid et al. 2002, Hajiabdolmajid et al. 2003). The  $c_r$  is greater than 0 MPa as it represents the cohesion of the zone using the CWFS method, and does not represent the “true” cohesion for a real fracture. However, even for a zone representing rock containing fractures, there may be still some cohesive strength within the zone. Using a non-zero  $c_r$  is a consequence of using continuum numerical models to simulate a fracturing process. The calibrated  $\phi_i$  is  $5^\circ$ , indicating an increased level of brittleness compared to the initial  $10^\circ$ , but it still falls within the acceptable range for the CWFS method, as indicated by Walton (2019).



**Figure 4-2 Results for the simulation of the Qirehataer Diversion Tunnel using the CWFS in *FLAC2D*: a) the initial parameters suggested by the guidelines of Walton (2019) b) – e) the calibration procedure, f) the final parameters and results of the calibration with an acceptable match to the field observations. The comparative failure profile key, showing the reported v-notch formed in the field and the interpretation of the authors of other spalling cases as reported by Zhao et al. (2022).**

**Table 4-2 Calibrated model parameters for the gneissic granite at the Qirehataer Diversion Tunnel for CWFS modeling in *FLAC2D*.**

<b>Parameter</b>	<b>Peak/Initial</b>	<b>Residual/Mobilized</b>
$c$ (MPa)	20	5
$\phi$ ( $^{\circ}$ )	5	50
$T$ (MPa)	8	0
$\psi$ ( $^{\circ}$ )	5	50
$e_c^{ps}$		0.002
$e_{\phi}^{ps}$		0.004

#### 4.5 CONCLUSION

The Qirehataer Diversion Tunnel in western China is an excavation constructed in competent brittle rock, with medium to high in situ stresses. As such, spalling failure was observed during the tunnel construction. In this study, the CWFS method was used to simulate the failure observed in the field. For this method, an initial set of values was determined using the guidelines for selecting strength parameters proposed by Walton (2019). Using these guidelines, the results initially underestimated the depth of failure for the worst-case scenario. Nevertheless, these results aligned with various other field observations, suggesting that the initial parameters yield reasonable results that may be encountered in actual field conditions. Through a back analysis process and the adjustment of some of the strength parameters, the CWFS method successfully reproduced the spalling failure observed in the severe spalling cases. By reducing the  $c_r$  and  $\phi_i$ , a profile matching the field observations was achieved.

## **CHAPTER 5 - THE IMASS METHOD FOR BRITTLE ROCK FAILURE MODELLING IN UNDERGROUND EXCAVATIONS**

### **5.1 INTRODUCTION**

As shown in Chapter 2, there is an extensive list of methods for modelling brittle rock failure in underground excavations. All have advantages and disadvantages, and their design applications are different. One of the big disadvantages of most of these methods is the uncertainty of the selection of initial parameters. This is particularly true for continuum methods, where, due to their nature, the selection of parameters is an abstraction of actual material behaviour. Brittle rock failure is a fracturing process that cannot be perfectly modelled with a continuum; therefore, fictitious parameters need to be simplified into a continuum. The selection of such parameters is often challenging for design. This leaves a gap in the methods to represent brittle failure with a continuum. There is room for a method in which the selection of strength parameters is simpler, which still yields valuable results for the design of excavations in this type of rock. With this goal in mind, the IMASS method for brittle rock failure modelling is proposed. It makes use of the IMASS constitutive model developed in *FLAC3D* (v 9.166) by Itasca. It uses its built-in assumptions to facilitate the selection of appropriate strength criteria. Introducing this novel method aims to show the spalling failure around underground excavation. Similar to all other continuum numerical modelling methods, this one does not represent the true spalling mechanism. It is an approximation that can be used to design underground excavations but cannot explicitly reproduce the complex mechanisms of brittle rock failure. The application of the IMASS constitutive in this investigation does not capture displacement and bulking of the rock. Other methods (Garza-Cruz et al., 2014) should be used if those are the goals of the designer.

### **5.2 IMASS OVERVIEW**

The Itasca Model of Advanced Strain Softening (IMASS) constitutive model was developed to facilitate the simulation of caving and bulking for underground cave mines. It is meant to represent the strength degradation and bulking as the rock goes from being damaged to disintegrated (Ghazvinian et al. 2020). It modifies the behaviour of the rock due to plastic deformation according to four different mechanisms:

1. Cohesion Weakening and Friction Strengthening: Based on the suggestions by Martin and Chandler (1994), Martin (1997), and Hajiabdolmajid et al. (2002), as rock fails, the creation of new fractures reduces the cohesive strength of the rock mass and increases the friction.
2. Post-peak Brittleness: This is the behaviour of the rock after its peak strength. The reduction of the rock strength after yielding is controlled by the rate of plastic deformation.
3. Modulus Softening: As rock increases in volume and fractures, the modulus of elasticity is reduced. A failed material has a lower deformation modulus and capacity to take and redistribute load.
4. Dilational Behaviour: It is the change in volume as fractures develop within the rock. This determines the amount of displacement as the rock fails.

Three distinct failure envelopes define the IMASS constitutive model: 1) peak strength; 2) post-peak strength; and 3) ultimate strength. The peak strength envelope is the strength of the rock from its intact state up to the initial state of failure. It is defined by the generalized Hoek-Brown failure criterion. The input parameters for the peak strength are  $GSI$ ,  $m_i$ ,  $\sigma_{UCS}$ , and  $\sigma_t$  (Ghazvinian et al. 2020). The stiffness is determined by the equation (Hoek and Diederichs, 2006):

$$E_{rm} = E_i \left[ 0.02 + \frac{1}{1 + \exp\left(\frac{60 - GSI}{11}\right)} \right] \quad (5-1)$$

where  $E_i$  is the input of Young's modulus. The  $\nu$  is given by (Itasca, 2024):

$$\nu = 0.32 - 0.0015 \times GSI \quad (5-2)$$

Once the peak strength envelope is reached, the strength of the rock transitions to the post-peak envelope. A Hoek-Brown failure envelope determines the post-peak failure envelope. This post-peak Hoek-Brown envelope is defined by:

$$s = 0 \quad (5-3)$$

$$a = 0.6 + \frac{VSI}{0.67} \times 0.25 \quad (5-4)$$

$$m_b = 0.1614 \times \exp(0.0836 \times \phi_b) \quad (5-5)$$

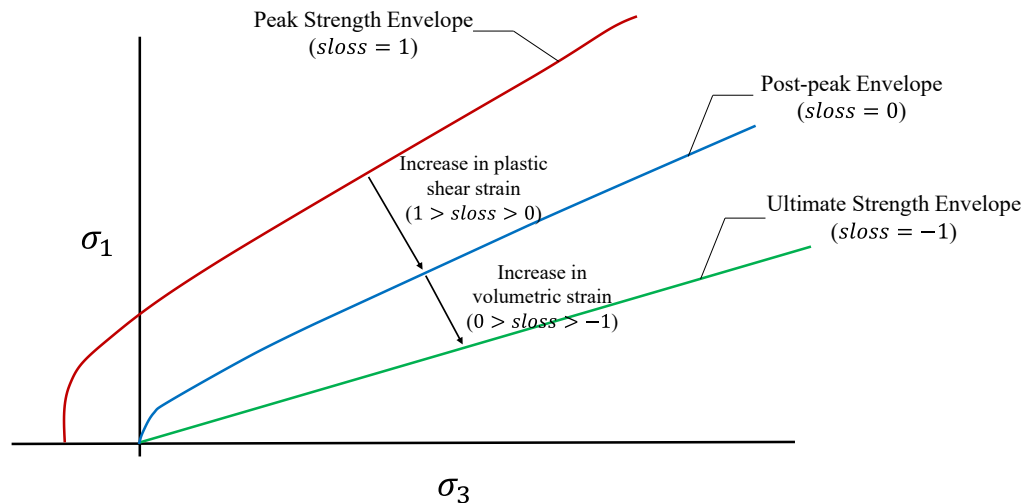
where  $VSI$  is the volumetric strain increment with a maximum value of 0.67 and  $\phi_b$  is the basic friction angle of rock blocks (Ghazvinian et al., 2020). Both of these parameters are

based on some assumptions of loose rock material behaviour, the detailed selection is in Itasca (2024). The change from peak to post-peak envelope is not instantaneous, it is dependent on the plastic shear strain. It changes from the peak as a function of  $e^{ps}$ . The post-peak strength is reached when the plastic shear strain has reached a critical value ( $e_{crit}^{ps}$ ). The critical plastic shear strain is determined by (Lorig and Varona, 2013):

$$e_{crit}^{ps} = \frac{12.5 - 0.125 \times GSI}{100 \times d} \quad (5-6)$$

where  $d$  is the zone size in meters. This strength transition is similar to the mechanism proposed by Hajiabdolmajid et al. (2003) and derived from the experiments of Martin and Chandler (1994)

The previous equations also define the ultimate strength envelope, which occurs when the rock has reached maximum porosity. This occurs when the rock is entirely disintegrated and loosened. It mimics the behaviour of highly fractured rock at low confinements. The maximum porosity of any rock is assumed by IMASS to be 40% (Itasca, 2024). The transition of post-peak to ultimate strength envelope is a function of  $VSI$ . Once the maximum VSI has been reached (0.67), the strength of the rock mass is defined by the ultimate strength envelope. Figure 5-1 illustrates the three failure envelopes and the transition between them.



**Figure 5-1 The three IMASS constitutive models strength envelopes in the principal stress space and the mechanisms that control the transition from one envelope to the next with the corresponding *sloss* values for each transitional state.**

To better monitor the damage in the rock mass and the current strength envelope, the IMASS has a parameter named “*sloss*”. It serves as a measure of the softening after the peak strength has been reached. The value of *sloss* varies from 1 to -1, where it is given by (Ghazvinian et al., 2020):

$$sloss = \begin{cases} 1 - \frac{e^{ps}}{e_{crit}^{ps}}, & \text{peak to post-peak strength} \\ -\frac{VSI}{VSI_{max}}, & \text{post-peak strength to ultimate} \end{cases} \quad (5-7)$$

The values of *sloss* corresponding to the current strength envelope can be visualized in Figure 5-1. This allows for monitoring the state of damage the rock is at, with 1 being fully intact elastic rock, 0 being fractured rock that is yet to unravel, and -1 fully unravelled rock. From peak to post-peak strength, the *sloss* is dependent on the plastic shear strain. From post-peak to ultimate strength, the *sloss* depends on the volumetric strain increment (Ghazvinian et al., 2020). For more details on the IMASS constitutive model, the reader should refer to Itasca (2024).

### 5.3 METHODOLOGY

The capacity to model the plastic behaviour of the rock mass in such a detailed way makes the IMASS constitutive model a good tool for modelling brittle failure around underground excavations. Drawing from the DISL method proposed by Diederichs (2007) and the CWFS by Hajiabdolmajid (2002), the IMASS constitutive model can be modified to produce peak and post-peak failure envelopes that mimic brittle rock behaviour. The investigation in this chapter used the IMASS constitutive model to apply the concepts of the DISL and the CWFS methods. These processes often include strengthening of the material after failure at certain confinement stresses. The IMASS constitutive model was developed to represent strain-softening behaviour; therefore, the use of this constitutive model in this study is not as intended by the developers. However, it can still produce results that can be used for the design of these types of excavations. This new IMASS method was tested and applied to simulate the brittle failure observed in the MBE at the URL in LdB granite.



### 5.3.1 IMASS constitutive model strength envelopes for brittle rock failure modelling

To effectively model brittle rock failure around underground excavations, the strength envelopes of the IMASS constitutive model need to be modified as to achieve CWFS/DISL-type behaviours. Since the Hoek-Brown failure criterion provides the strength parameters, the DISL peak and residual envelopes proposed by Diederichs (2007) can be easily applied. The peak strength envelope should correspond to the Damage Initiation. For the excavation scale, the Damage Initiation strength corresponds to the crack initiation envelope (Diederichs, 2007). This crack initiation envelope is characterized by having unconfined compressive strength equal to the  $\sigma_{ci}$ , and confined strength occurring at a constant deviatoric stress (Martin, 1997). In practice, it means that the peak strength envelope in IMASS is defined by the  $\sigma_{ci}$  of LdB granite and a low  $m_b$ . The tensile strength of the Damage Initiation envelope is suggested to be the laboratory  $\sigma_t$  (Diederichs, 2007). The Spalling Limit suggested by Diederichs (2007) determines the post-peak envelope. This limit is given by the ultimate in situ strength of rock at the tunnel scale. It is often associated with the crack damage envelope obtained in laboratory experiments. The Spalling Limit is given by the ratio of  $\frac{\sigma_1}{\sigma_3}$  and recommended to be at around 7 to 10. It is cohesionless, meaning that the post-peak strength envelope should have  $\sigma_{UCS}$  of 0 (Diederichs, 2007).

Applying these failure envelopes in the IMASS constitutive models is not as direct as when using the Hoek-Brown or the Mohr-Coulomb constitutive models. The input parameters required to define the peak strength envelope are  $GSI$ ,  $\sigma_{UCS}$ ,  $m_i$ , and  $\sigma_t$ . To determine the post-peak envelope, the required parameter is  $\phi_b$ . Other parameters for the post-peak envelope are already determined by the constitutive model itself, such as the  $VSI_{max}$ . Other parameters required to determine the constitutive model behaviour are the  $E$  of the intact rock and  $e_{multi}^{ps}$ . This last parameter allows for the  $e_{crit}^{ps}$  to be modified to achieve more brittle or ductile behaviour of the rock by multiplying Equation (5-6) by the input factor. This makes the  $e_{crit}^{ps}$  be defined as:

$$e_{crit}^{ps} = \frac{12.5 - 0.125 \times GSI}{100 \times d} \times e_{multi}^{ps} \quad (5-8)$$

The parameters selected for the present purposes do not necessarily correspond to true material properties. Instead, they are a numerical manipulation of the IMASS constitutive

model to obtain the desired failure envelopes. Table 5-1 shows the selected input parameters to make the IMASS constitutive model replicate the failure envelopes of the DISL method. There are some important notes on the selection of these parameters. The  $\sigma_{UCS_{input}}$  selected is not the unconfined compressive strength of the LdB (200 – 215 MPa), it is the crack initiation stress of this rock (90 – 115 MPa). The naming convention of  $\sigma_{UCS_{input}}$  is used to match the input parameters required in *FLAC3D*. The *GSI* selected was not a field measurement of the lithology and structure as intended by Marino and Hoek (2000). Instead, it was a mathematical manipulation of the constitutive model to obtain the desired strength envelope. The value was 99, not 100, because 100 is not an allowable input in *FLAC3D*. The  $m_i$  was selected to match the  $\sigma_{ci}$  strength envelope where failure occurs at a constant deviatoric stress. The  $\sigma_t$  was selected to match the laboratory tensile strength of the LdB as measured by Martin (1997). The *E* was the intact rock young's modulus determined by Hajiabdolmajid et al. (2002) for the CWFS method. The  $\phi_b$  was selected to match the residual friction angle as calibrated by Hajiabdolmajid et al. (2002). The  $e_{multi}^{ps}$  was set to 1 as to keep Equation (5-6) without modification.

**Table 5-1 Preliminary IMASS input parameters for the MBE at the URL to obtain a DISL-like behaviour.**

IMASS input parameter	Value
$\sigma_{UCS_{input}}$	100 MPa
<i>GSI</i>	99
$m_i$	1
<i>E</i>	60 GPa
$e_{multi}^{ps}$	1
$\phi_b$	48°
$\sigma_t$	6 MPa

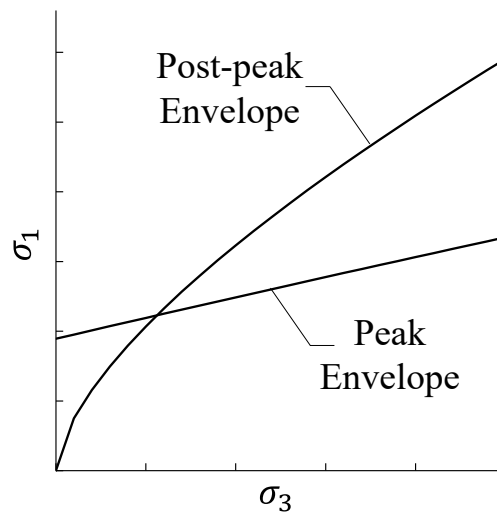
Using Equation (5-3) to Equation (5-5), the strength envelopes can be determined given the input parameters. The strength envelopes resulting from the input values from Table 5-1 are shown in Table 5-2. For the application of this method, only the peak and post-peak strength envelopes are of interest. These results can also be plotted in  $\sigma_1 - \sigma_3$  space to better understand the relationship between strength and confining pressure. Figure 5-2 is the two resulting theoretical failure envelopes in the IMASS constitutive model with the input

parameters. For the IMASS method to be able to simulate brittle failure, these theoretical strength envelopes should be replicated by the models.

**Table 5-2 Preliminary Hoek-Brown values of the peak and post-peak failure envelopes of the IMASS method for the MBE at the URL**

Parameter	Peak	Post-Peak
$\sigma_{UCS_{input}}$	100 MPa	
$m_b$	0.96	8.92
$s$	0.89	0
$a$	0.50	0.6*

\*At the post-peak failure envelope, the *VSI* is 0

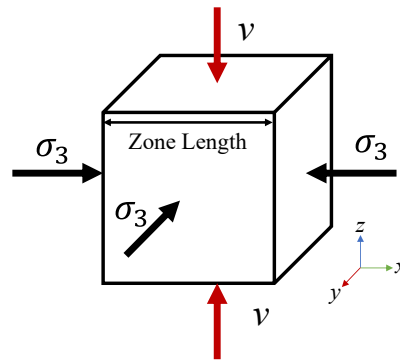


**Figure 5-2 Theoretical peak and post-peak failure envelopes in principal stress space for the input parameters suggested for the MBE at the URL applying the theory of the DISL method with the IMASS constitutive model.**

### 5.3.2 UCS and Triaxial Tests

Unconfined and confined compression tests were modelled in *FLAC3D* using the input parameters from Table 5-1 to test the effectiveness of replicating the theoretical failure envelopes. These models are to test the behaviour of the IMASS constitutive model. They are not meant to simulate laboratory experiments of the LdB granite. Therefore, to directly understand the constitutive model, the UCS and triaxial test were performed on a single zone element. With this, the behaviour of the constitutive model can be dissected to understand all mechanisms of plasticity, dilation, and strain.

The first stage of creating a single-zone triaxial test environment was to determine the appropriate size of the zone. As this method was applied to a tunnel, and most of the failure was expected to occur along the tunnel boundary, the appropriate size for the test zone (2.5 cm) is similar to the zone size near the excavation boundary. To keep the results consistent and symmetrical, a cubic zone was used for the simulation. Once the zone size was determined, the confining stresses were applied throughout the sample in all directions. Since this model is in three dimensions, the stresses were applied in the  $x$ ,  $y$ , and  $z$  directions. This created an initial state of stress to which the test was applied. The loading on the specimen was done along the  $z$  direction. A velocity loading ( $v$ ) was applied to the top and bottom of the specimen. The velocity needed to be slow enough to avoid a dynamic loading condition in the specimen. The selection of the velocity is a function of the specimen size and the stiffness of the block. For this study, an adequate velocity was determined via trial and error. The final velocity selected was  $8.e-9$  m/s. Figure 5-3 shows the model setup and the stresses. Boundary conditions of constant stress were applied to the other two faces ( $x$  and  $y$ ) to maintain the confining stress throughout the testing. The test was repeated multiple times to obtain the strength at different confinement levels.



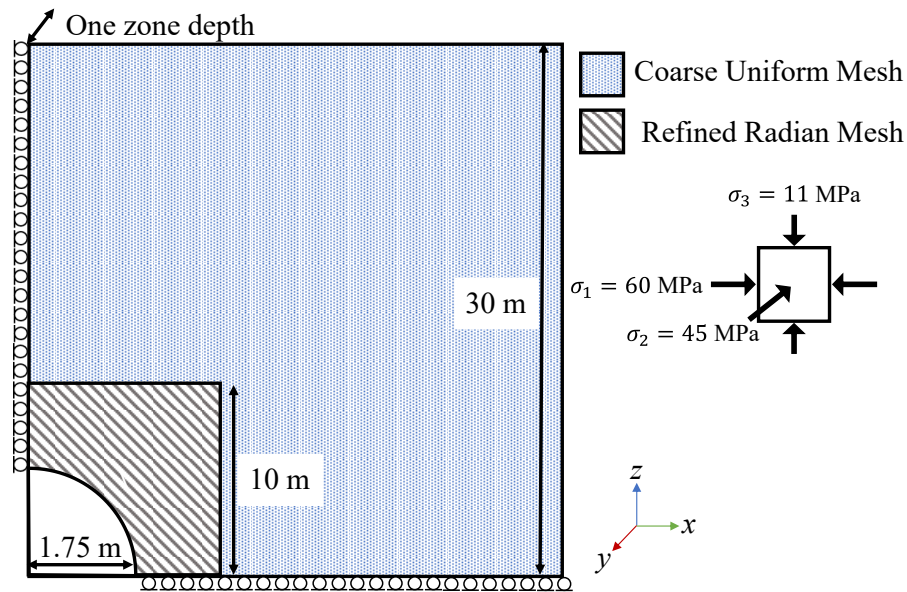
**Figure 5-3 Single zone triaxial test model set up showing the loading velocity boundary in the  $z$ -direction and the confining stress application on the  $y$ - and  $x$ -directions.**

The test model for a single zone can help investigate more than the peak and post-peak strengths. With these models, a more in-depth study of the mechanical behaviour of the zones was conducted. Stress-strain curves were created to analyze how a zone deformed as it was loaded. The peak and post-peak strength were obtained and compared to the theoretical DISL envelopes to assess the capacity to reproduce these envelopes. The change in the strength as plastic strain increases was investigated. This helped to deepen the understanding

of the transition between peak and post-peak strength envelopes. Dilation behaviour can also be tested by measuring the change in volume as loading increases. This allowed to understand how the rock mass displacement is modelled in IMASS. The *sloss* parameter was also monitored to understand the transition between the strength envelopes. For this in-depth investigation, multiple histories were taken during loading. The values monitored throughout the experiment were axial stress, axial strain, lateral strain, volumetric strain, friction angle, cohesion, and *sloss*. These histories comprehensively explained the inner workings of the IMASS constitutive model. All models were run with *FLAC3D* v9.166.

### **5.3.3 Application to the MBE at the URL**

Once the IMASS constitutive model was understood and it was corroborated that the IMASS model can recreate DISL failure envelopes, the method was applied to a case scenario. As done for the previous investigation into CWFS and DISL, the first case scenario investigated was the MBE at the URL. This demonstrated whether the IMASS method is viable for modelling the spalling failure around a tunnel. The tunnel was modelled using symmetry, where only a quarter was modelled. The mesh was uniform with small 2.5 cm zones near the excavation boundary and 40 cm zones at the edge of the model, the change of zone size was gradual, following a 2:1 density increase. The zones closest to the excavation are radial, while far from it they transition to uniform. The external boundary of the model is 30 m from the center of the excavation, far enough so the boundary does not affect the stress redistribution. Since the IMASS constitutive model is only available in *FLAC3D*, the models were in 3D plane-strain. To achieve the plane strain condition, the model was one zone deep in the *y*-direction, with the velocity of the nodes fixed in the *y*-direction. The zones were kept to 1:1:1 in all directions to avoid bad zone geometry that could cause mesh-dependent issues. For symmetry purposes, the boundary conditions on the edge of the excavation were rollers, while all other boundaries were fixed in all directions. Figure 5-4 is a simplified diagram of the *FLAC3D* model for the MBE.



**Figure 5-4 Model setup for the MBE at the URL using the IMASS method, showing the excavation location and the mesh sizes. The stresses are rotated to achieve the symmetry, only one-quarter of the tunnel is simulated using roller boundaries for symmetry, and the model is one zone in the y-direction, making it a 2.5D model.**

The in situ stress regime at the MBE is:  $\sigma_1 = 60$  MPa,  $\sigma_2 = 48$  MPa,  $\sigma_3 = 11$  MPa (Martin, 1997). While in the field, the stresses had some rotation, in this investigation the stresses were rotated so that  $\sigma_1$  was in the  $x$ -direction. This is to achieve symmetry and simplify the geometry into a quarter circle. Gravity was not considered, as the in situ stresses were high enough to render its effects minimal. The strength parameters shown in Table 5-1 are applied to the rock. The tunnel excavation was done using FISH's "zone relax" function. This mimics the effect of the face as the tunnel is excavated. This study used it to achieve static equilibrium to the model without creating artificial failure of elements from instantaneous removal of the excavated zones.

For this method, the numerical failure of a zone in the model is considered to simulate spalling failure in the field. The failure was assessed according to the number of zones that failed in the model. This is similar to the methodology from Chapter 3. The measures of failure of interest in this method were the same as detailed in Chapter 3. The five parameters of failure for this study were controlled or uncontrolled,  $d_f$ , angle of failure, area of failure, and shape of failure. The results were also compared graphically to the failure profile presented by Martin (1997). The combination of the numerical failure characterization and

the graphical characterization helped assess the capacity of this new IMASS method to reproduce spalling around underground excavation in brittle rock.

### 5.3.4 Input strength parameters sensitivity analysis

As a novel method of modelling brittle rock failure, it is essential to test its robustness. This was done via a sensitivity analysis of the input strength parameters. With this investigation, the effect of each parameter can be better understood in isolation. Investigating each parameter on its own also tests the robustness of the method and gives an idea of how sensitive the method is to a single parameter. This investigation was conducted by doing a sensitivity analysis on each parameter independently. The parameter of interest was changed, while all other parameters were kept to their original values. Each variable was treated as if it were independent of each other. While this is not the case for rock, this investigation was done to test the robustness of the method by isolating variables.

The values that were investigated were:  $\sigma_{UCS_{input}}$ ,  $m_i$ ,  $e_{multi}^{ps}$ , and  $\phi_b$ . The variation of each value was done following the suggestions of DISL parameter selections by Diederichs (2007) and the CWFS selection guidelines by Walton (2019). The range for  $\sigma_{UCS_{input}}$  is based on the range of  $\sigma_{ci}$  from LdB granite experiments (Martin, 1997). The range selected was 90 MPa to 118 MPa. This corresponds to 42% and 55% of the laboratory intact LdB granite  $\sigma_{UCS}$  (213 MPa). For the  $m_i$ , the selected range followed the suggestion by Diederichs (2007), and Perras and Diederichs (2016), where it should follow the Damage Initiation envelope. The  $m_i$  should create a strength envelope where failure occurs at a constant deviatoric stress (Martin, 1997). For this investigation, the range selected was from 0 to 2. Defining a suitable critical plastic strain is a complicated endeavour. Martin and Chandler's (1994) experiments on LdB granite determined that with cyclic loading, the  $e_{crit}^{ps}$  of intact rock can be found, making this value a physical quality of the rock. However, this type of testing is rarely commonplace for rock mechanics investigations. Walton (2019) proposed a range of appropriate values from 0.1% to 0.6% for crystalline rock. For this investigation, the  $e_{multi}^{ps}$  was changed so that the  $e_{crit}^{ps}$  is within the suggested ranges. The range for  $e_{multi}^{ps}$  were from 0.1 to 1 to modify  $e_{crit}^{ps}$  from 0.4% to 2%. Lastly, the  $\phi_b$  had ranges following the

CWFS guidelines by Walton (2019). It ranged from 40° to 60°. Table 5-3 summarizes the selected ranges for each input parameter.

**Table 5-3 Range of parameters for the SA of the MBE at the URL using the IMASS method**

Input Parameter	Range
$\sigma_{UCS_{input}}$ (MPa)	90 – 118
$m_i$	0 – 2
$\phi_b$ (°)	40 – 60
$e_{multi}^{ps}$	0.1 – 1

### 5.3.5 Sensitivity Analysis of Hypothetical In Situ Stress Scenarios

The MBE at the URL is a single-case scenario for spalling around underground excavations. To test if the method can be used for design, multiple case scenarios should be explored. However, such experiments and results are seldom performed due to their high cost and complexity. It is rare to find field observations as well documented as the MBE. The  $d_f$  equation from Chapter 2 (Equation (2-1)), give multiple observations of the failure behaviour of brittle rock around tunnels. For the method to apply to multiple scenarios, the results of those equations should be able to be replicated. By performing an investigation on multiple fictitious stress scenarios, the method can be compared to the equations of  $d_f$  proposed.

The test was performed similarly to the one explained in Chapter 3. The strength parameters used are the ones selected for the LdB granite from the previous section (Table 5-1). To change the  $\sigma_{max}/\sigma_{ci}$  from Equation (3-8), the in situ stresses were changed. The change in the stresses was done by keeping the  $k$  ratio ( $\sigma_1/\sigma_3$ ) constant. Changing the stress values changes the maximum elastic-induced stress,  $\sigma_{max}$ . The  $k$  ratio in the MBE at the URL is 5.45 (Martin, 1997). The pairs of principal stresses used for each scenario are shown in Table 5-4. The model was run at each in situ stress regime, then the  $d_f$  was measured. The  $\sigma_{UCS_{input}}$  was assumed to be  $\sigma_{ci}$ . The results are then plotted compared to the chart by Diederichs et al. (2010).



**Table 5-4 Principal stress values for the hypothetical stress scenarios using the IMASS method.**

$\sigma_1$ (MPa)	$\sigma_3$ (MPa)
33.4	6.1
47.0	8.6
60.0	11.0
70.7	13.0
83.4	15.3
100.1	18.3

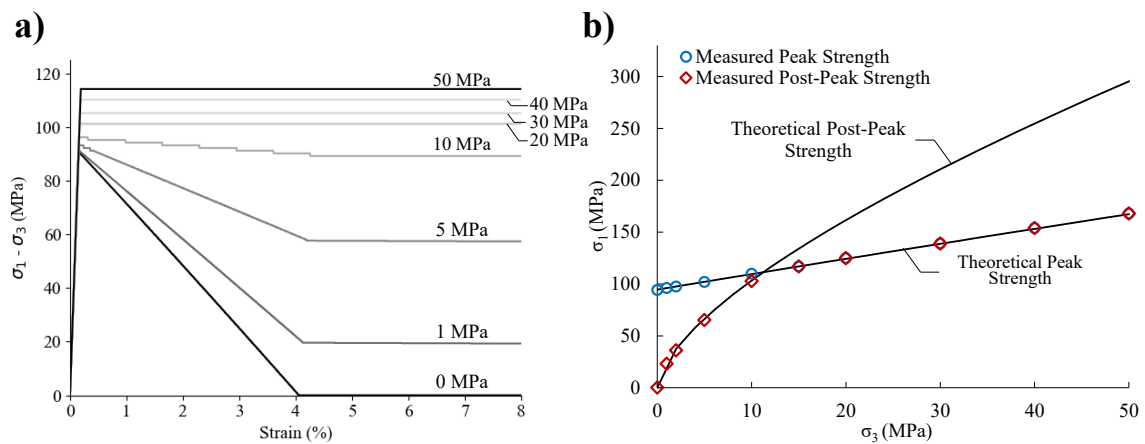
## 5.4 RESULTS

The method suggested in this study was applied for the first time here. Therefore, the initial results showed how feasible it is for the use in practice. The first step is to understand how the IMASS constitutive model works in detail. Then, it was applied to the MBE case scenario to test its ability to reproduce failure in brittle rock. The results helped assess the usefulness of this tool. Yet, the results are still preliminary and need a deeper investigation before the method can be fully recommended for design. The way the IMASS constitutive model was used is not the only way to simulate brittle failure in underground excavations, it can be used in other ways to produce equally valuable results.

### 5.4.1 UCS and Triaxial Test

The simulated laboratory tests were conducted on a  $2.5 \times 2.5 \times 2.5$  cm zone. Using Equation (5-8), the resulting  $e_{crit}^{ps}$  is 5%. This is an unrealistic value for rock, as it has been noted to be in the 0.1 to 0.6 % range (Martin and Chandler, 1994; Hajiabdolmajid et al., 2002; Walton, 2019). Figure 5-5a shows the deviatoric stress-strain curves for the single zone triaxial test, for a confining pressure from 0 to 50 MPa. The zone had two different behaviours, depending on the confining pressure. At low confining pressures, the behaviour was strain-softening, where the transition from peak to post-peak strength is a gradual reduction of stress as a function of plastic strain. The second mechanism was that at high confinement ( $\sigma_3 > 10$  MPa), the zones behaved perfectly plastic. This dual behaviour has been noted to occur in brittle rocks where, at high confinements, the rock is no longer brittle but perfectly plastic (Paterson, 1958; Gerogiannopoulos, 1976). The peak and post-peak strength were also plotted in  $\sigma_1 - \sigma_3$  space to compare to the theoretical DISL failure envelopes from Figure 5-1. The results of this comparison are shown in Figure 5-5b. There

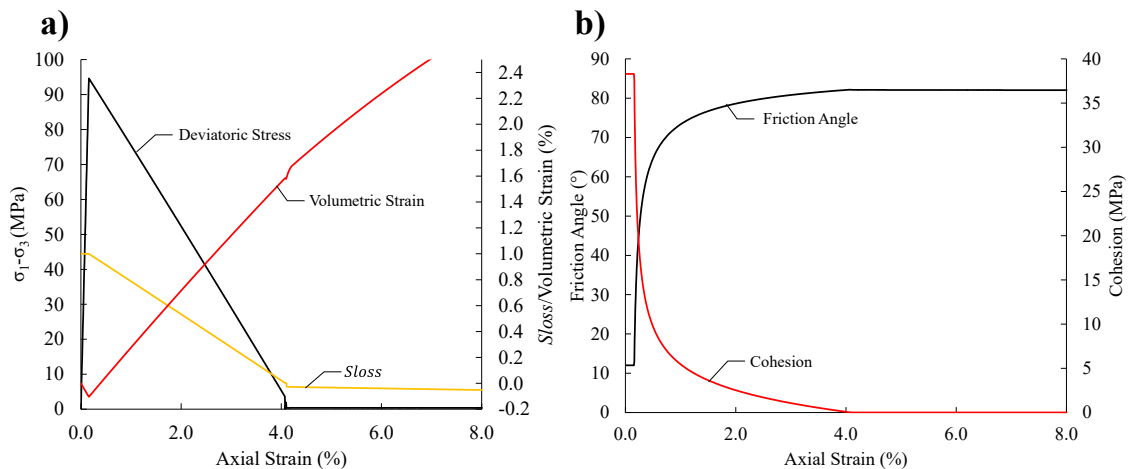
is a significant difference between the single-zone behaviour and the theoretical envelopes. The IMASS constitutive model does not allow for the post-peak strength to be higher than the peak strength (Itasca, 2024). This means that after the intersection between the peak and post-peak envelopes, the post-peak becomes the same as the peak. While this behaviour might appear to hinder the IMASS method, authors have noted that such behaviour can be appropriate to model failure around brittle rock pillars in high-stress situations (Hamediazad and Bahrani, 2024). The behaviour also occurs only at high confinements (10 MPa), this stress level is rarely encountered near the boundary of underground excavation, where confinement is relatively low. There was no indication that this behaviour of the post-peak envelope would hinder the use of the IMASS method.



**Figure 5-5 Simulated triaxial test results for LdB granite using the IMASS method a) in deviatoric stress vs strain space b) in principal stress space showing the peak and post-peak failure envelopes of the models compared to the theoretical envelopes.**

The triaxial test served to investigate the IMASS constitutive model in more detail. This model is complex and involves many parameters, so creating a comprehensive explanation of parameters helped to understand the results in design situations. It also aided in the selection of parameters for calibration. The first simulation investigated was the UCS test, which represents the conditions at the boundary of an excavation. The results from this investigation are shown in Figure 5-6. In Figure 5-6a, the relationship between axial loading, *loss*, and volumetric strain is explored. In Figure 5-6b the relationship between strength parameters, friction angle and cohesion, with respect to strain, is shown. At the beginning of the test, from equilibrium at the confining level to failure, all parameters behaved as expected, elastically. There was a reduction in volume as the sample contracted. The *loss* remained

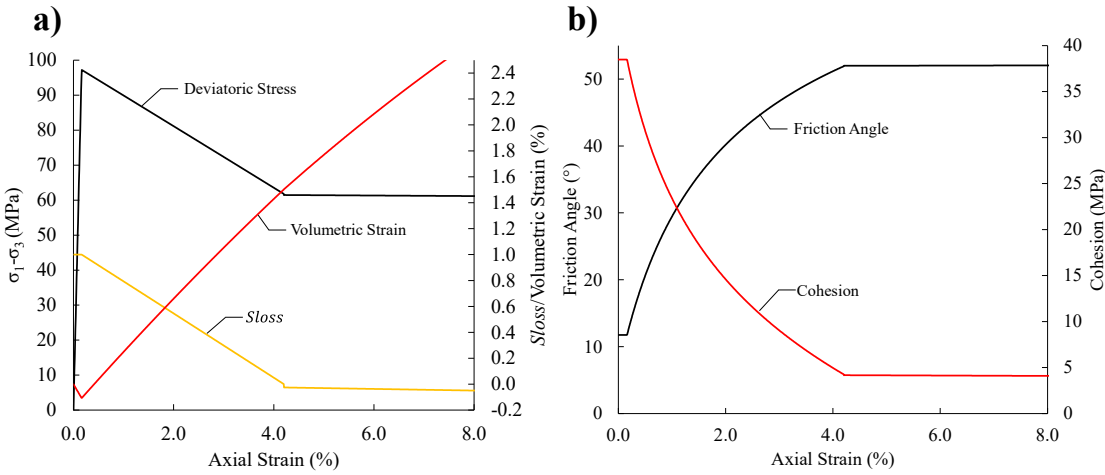
at 1 as there was no  $e^{ps}$ . Strength parameters remained at the values of peak strength. Once peak strength was reached, multiple mechanisms took place. The most notable is the gradual degradation of strength with the increase in axial strain. This behaviour was simultaneous and nonlinear for both friction angle and cohesion, in contrast to the CWFS behaviour. Renani and Martin (2018) suggested that strength mobilization of this type is preferable over the linear non-simultaneous behaviour initially proposed in the CWFS method (Hajiabdolmajid et al., 2002). After the peak strength was reached, volumetric strain reversal started. The  $sloss$  parameter decreases linearly from 1 at  $e^{ps} = 0$  to 0 when  $e^{ps} = 5\%$ , this was consistent with Equation (5-8). At this point, the post-peak envelope was reached. From  $sloss = 0$  onwards the model behaves perfectly plastic. There is no more change in strength parameters with strain increase. Notably, the  $sloss$  parameter decreases at an insignificant rate. This means that the rate of  $VSI$  is low enough as to render the ultimate strength envelope irrelevant for the model at this confinement level.



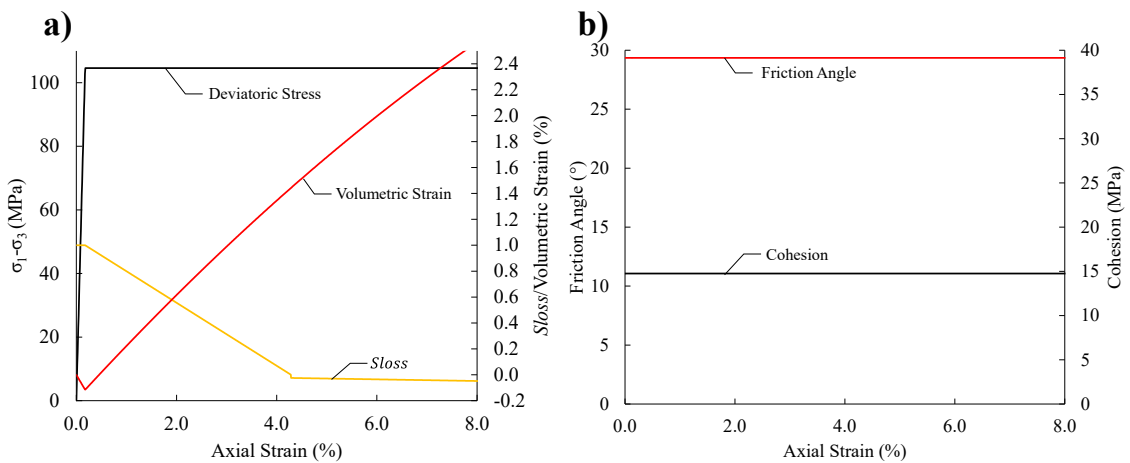
**Figure 5-6 Simulated triaxial test results for LdB granite using the IMASS method with 0 MPa confinement where a) deviatoric stress,  $sloss$ , and volumetric strain compared to axial strain, b) change in strength parameters  $c$  and  $\phi$  with respect of axial strain increase.**

The same investigation was repeated at confining stresses of 5 MPa and 20 MPa. Figure 5-7 presents a summary of the behaviour of the zone under a 5 MPa confinement. The results from this investigation are shown in Figure 5-7. The behaviour in this unconfined situation was very similar to the UCS test. There was one notable exception; once the post-peak strength was reached, the volumetric expansion did not change its behaviour as in the

unconfined situation. This is due to the dilation starting after the post-peak was reached, at a plastic strain of 4%. The change in volume before this point was due to the continuous plastic strain as strength degrades, after such point, the volume increase is due to dilation behaviour. This change can be seen from Equation (5-8), where  $VSI$  is 0 prior to  $sloss < 0$ . The test that was analysed with the same methodology at a confinement stress where the material becomes perfectly plastic. Figure 5-8 shows the plot of deviatoric stress, volumetric strain,  $sloss$ ,  $c$ , and  $\phi$  for  $\sigma_3 = 20$  MPa. The difference from the previous plots was that there is no change in strength parameters after peak strength is reached. This was the expected result since the stress-strain plots in Figure 5-8a showed no change of strength after reaching plasticity.



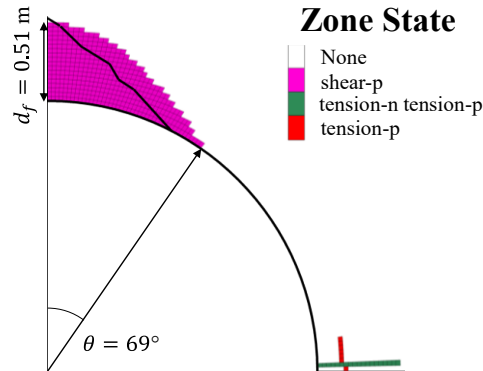
**Figure 5-7 Simulated triaxial test results for LdB granite using the IMASS method with 5 MPa confinement where a) deviatoric stress,  $sloss$ , and volumetric strain compared to axial strain, b) change in strength parameters  $c$  and  $\phi$  with respect of axial strain increase.**



**Figure 5-8 Simulated triaxial test results for LdB granite using the IMASS method with 20 MPa confinement where a) deviatoric stress,  $s_{loss}$ , and volumetric strain compared to axial strain b) change in strength parameters  $c$  and  $\phi$  with respect of axial strain increase.**

#### 5.4.2 Application to the MBE at the URL

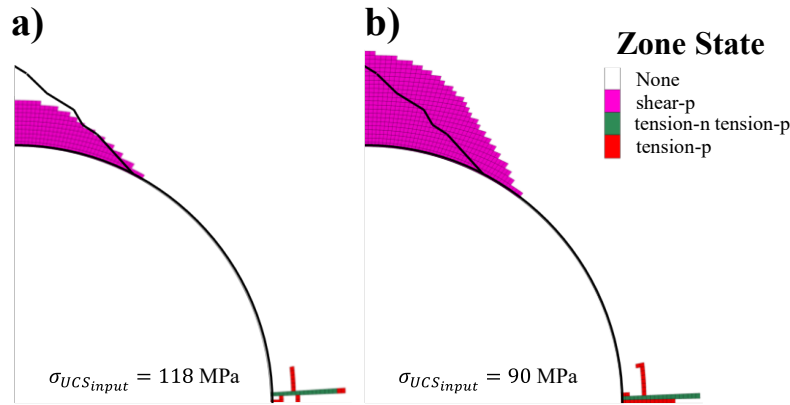
Once the IMASS constitutive model was understood, it was applied to a case study in an underground excavation. While the fact that there is no strength increase caused concern, the confining stress at which this would happen is  $> 10$  MPa. Such high confining stresses are not expected around the MBE at the URL model. Therefore, the method was still applicable. The initial set of results with the strength parameters detailed in Table 4-1 are shown in Figure 5-9. As a first approximation, the results matched the field observations to a reasonable degree of accuracy. The main difference between the field observations and the model is the shape and the angle of failure. Spalling failure in brittle rock is often observed in the v-shaped notch shape (Martin, 1997). The IMASS method shows a semicircular shape of failure. The  $d_f$  of failure from the model is 0.51 m a value comparable to the 0.54 m observed in the field (Martin, 1997). The angle of failure is significantly overpredicted from the observed  $57^{\circ}$  to a  $69^{\circ}$  modelled failure. Similarly, the area of failure is overpredicted, the IMASS method suggests  $0.68 \text{ m}^2$  while in the field,  $0.48 \text{ m}^2$  was observed. While the results did not demonstrate an identical match to the MBE failure profile, the method shows promise for use in design situations where the main concern is the  $d_f$  around the excavation. To better understand the method, the effect of each input parameter was investigated individually.



**Figure 5-9 Results of the IMASS method using the preliminary strength parameters showing the failure profile (using zone state) and its characterization compared to the observed failure profile at the MBE rotated for simplicity of visualization compared to the field observation at the MBE by Martin (1997) (chainage unknown).**

### 5.4.3 Input strength parameters sensitivity analysis

If the method is to be suggested for designing underground excavations in brittle rock, the effect of strength parameters needs to be understood. A sensitivity analysis of all inputs was conducted to do so. The first parameter of interest was the  $\sigma_{UCS_{input}}$ . The two different strengths investigated were 90 MPa and 118 MPa. Based of the  $\sigma_{UCS}$  value of 213 MPa for laboratory LdB (Martin, 1997), these suggested values corresponded to 42% and 55% of the intact rock UCS, respectively. There was an inverse correlation between  $\sigma_{UCS_{input}}$  and all measures of failure. The larger the input value, the less failure is encountered. Figure 5-10 shows the results of this investigation compared to the observed v-notch. Table 5-5 shows the numerical results of the same investigation. This value had a significant impact on the strength of the rock. By increasing the strength by 18% (from 100 MPa to 118 MPa), the  $d_f$  was decreased by almost 40% (from 0.51 m to 0.31 m). Similarly, decreasing the strength by 10% (from 100 MPa to 90 MPa), increased the  $d_f$  by around 30% (from 0.51 m to 0.65 m). The change in the angle of failure was less significant. The shape of failure was also not affected, as all had the same semi-circular shape.

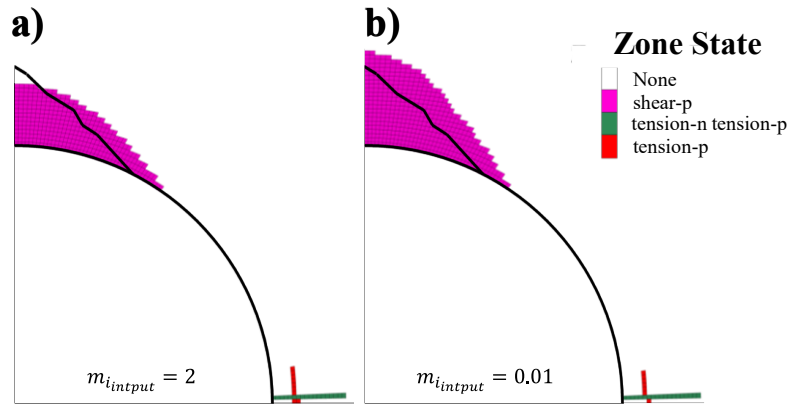


**Figure 5-10 Influence of  $\sigma_{UCS_{input}}$  on the failure profile in the IMASS method a)  $\sigma_{UCS_{input}} = 118$  MPa b)  $\sigma_{UCS_{input}} = 90$  MPa**

**Table 5-5 Influence of  $\sigma_{UCS_{input}}$  on the failure profile characterization in the IMASS method**

$\sigma_{UCS_{input}}$ (MPa)	Controlled	$d_f$ (m)	Angle of failure ( $^\circ$ )	Area of failure ( $m^2$ )	Shape of failure
118	Y	0.31	60	0.37	Semi-circle
90	Y	0.65	74	0.97	Transition

The next strength input parameter investigated was the  $m_{i_{input}}$ . It was changed according to the suggestions for the use of the DISL method by Diederichs (2007). The two values tested were 0.01 and 2. The value 0.01 was used instead of 0 due to the limitations of the IMASS constitutive model, which cannot take 0 as an input. The results are visualized graphically in Figure 5-11 and numerically in Table 5-6. The relationship between the  $m_{i_{input}}$  and the measure of failure was inversely correlated. Low values of  $m_{i_{input}}$  yield larger failure profiles. However, the effect of this parameter does not have the same level of consequences as the selection of  $\sigma_{UCS_{input}}$ . Doubling the  $m_{i_{input}}$  only decreases the  $d_f$  by 18% (from 0.51 m to 0.42 m). Decreasing the  $m_{i_{input}}$  to approximately 0 increases the  $d_f$  by 30% (from 0.51 m to 0.65 m). The low effect this parameter has is more evident when looking at the angle of failure, it stays relatively similar (change of 3%) regardless of the value selection. The shape of failure sees more effect, as with low  $m_{i_{input}}$  the shape of failure resembles more the v-notch shape observed at the MBE.



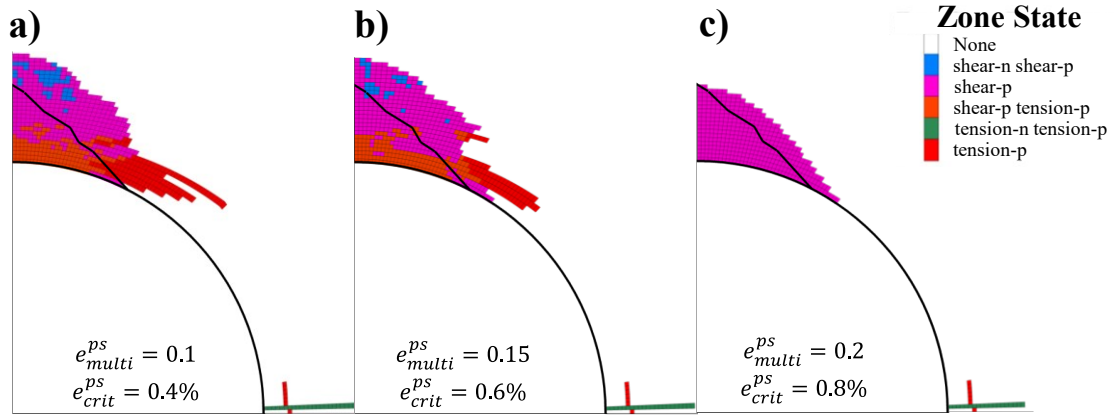
**Figure 5-11 Influence of  $m_{i_{input}}$  on the failure profile in the IMASS method a)  $m_{i_{input}} = 2$  b)  $m_{i_{input}} = 0.01$**

**Table 5-6 Influence of  $m_{i_{input}}$  on the failure profile characterization in the IMASS method**

$m_{i_{input}}$	Controlled	$d_f$ (m)	Angle of failure (°)	Area of failure (m <sup>2</sup> )	Shape of failure
0	Y	0.65	68	0.82	Transition
2	Y	0.42	69	0.59	Semi-circle

A critical value for the IMASS constitutive model is the  $e_{crit}^{ps}$ : which defines the rate at which the strength transitions from peak to post-peak failure envelopes. With the zone size from this model, the  $e_{crit}^{ps} = 4\%$ , this is 10-fold the suggestions by Walton (2019). The  $e_{multi}^{ps}$  was changed to obtain a value in line with Walton's (2019) suggestions, between 0.1% and 0.6%. The range of value for  $e_{multi}^{ps}$  started at 0.1 and increased by 0.05 until the original value of 1 was reached. When the multiplier was low 0.1 and 0.15, uncontrolled numerical failure occurred. Once the multiplier was  $> 0.2$ , there was no change in the results, i.e. from 0.2 to 1 the measures of failure were the same. Figure 5-12 shows the two types of results for controlled and uncontrolled outcomes. For all  $e_{multi}^{ps} > 0.2$  the results are identical to Figure 5-12c. Table 5-7 describes the measures of failure for all the values used for this investigation. What was found from this SA, was that there is a minimum value of  $e_{crit}^{ps}$  which yields controlled failure, which is 0.2. Increasing  $e_{multi}^{ps}$  beyond this value does not have an effect on the result.



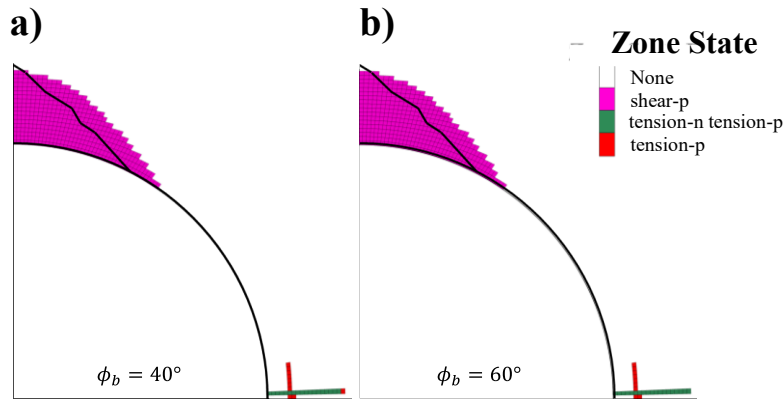


**Figure 5-12 Influence of  $e_{multi}^{ps}$  on the failure profile in the IMASS method a)  $e_{multi}^{ps} = 0.1$  b)  $e_{multi}^{ps} = 0.15$  c)  $e_{multi}^{ps} = 0.20$**

**Table 5-7 Influence of  $e_{multi}^{ps}$  on the failure profile characterization in the IMASS method**

$e_{multi}^{ps}$	$e_{crit}^{ps}$ (%)	Controlled	$d_f$ (m)	Angle of failure (°)	Area of failure (m <sup>2</sup> )	Shape of failure
0.1	0.4	No	NA	NA	NA	NA
0.15	0.6	No	NA	NA	NA	NA
0.2	0.8	Yes	0.51	67.5	0.68	Semi-circle
0.25	0.9	Yes	0.51	67.5	0.68	Semi-circle
0.5	1.9	Yes	0.51	67.5	0.68	Semi-circle

The last strength input parameter to analyze was the  $\phi_b$ . The SA performed here followed Walton's (2019) suggestions for crystalline rock. The two values explored were 40° and 60°. The results from this investigation are shown in Figure 5-13 and Table 5-8. The results of this  $\phi_b$  values and the benchmark value of 48° were identical. This can be explained by looking at the plots of  $e^{ps}$  and  $sloss$  near the excavation boundary after the model reached equilibrium. At the location of the highest plastic deformation, the crown, the plastic strain is only 0.24% for the model with  $\phi_b = 40^\circ$ . This gave an  $sloss = 0.94$  and a  $\phi_r = 19^\circ$ . For the model with  $\phi_b = 60^\circ$ , the resulting  $e^{ps} = 0.23\%$  at equilibrium, resulting on a  $sloss = 0.94$  and  $\phi_r = 29^\circ$ . At these values of residual friction, the change from initial  $m_b$  to residual is not significant enough for there to be change in the failure profile. Both of these values allow for the failure of the zones to be controlled while not changing their shape significantly.



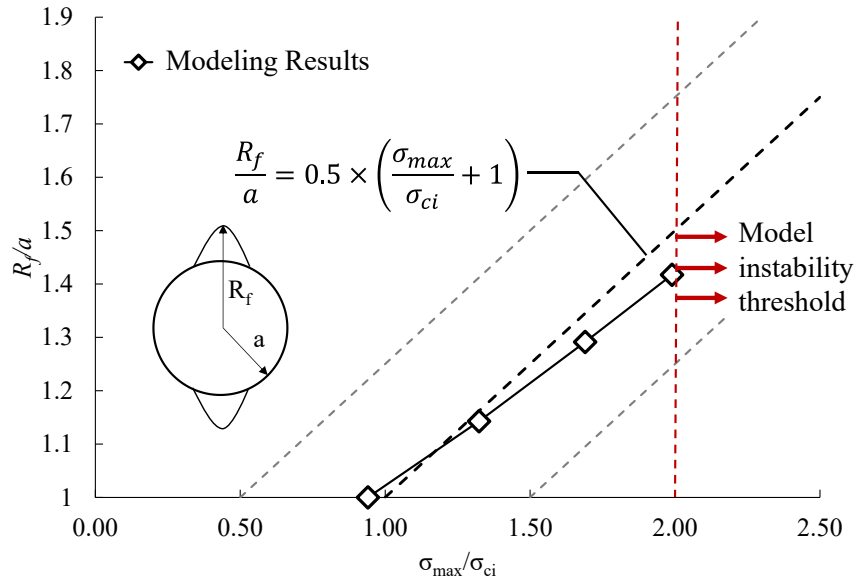
**Figure 5-13 Influence of  $\phi_b$  on the failure profile in the IMASS method a)  $\phi_b = 40^\circ$  b)  $\phi_b = 60^\circ$**

**Table 5-8 Influence of  $\phi_b$  on the failure profile characterization in the IMASS method**

$\phi_b$ ( $^\circ$ )	Controlled	$d_f$ (m)	Angle of failure ( $^\circ$ )	Area of failure ( $m^2$ )	Shape of failure
40	Y	0.51	69	0.69	Semi-circle
60	Y	0.51	69	0.69	Semi-circle

#### 5.4.4 Sensitivity Analysis of Hypothetical In Situ Stress Scenarios

Different stress scenarios were investigated to determine if the IMASS method can replicate the field observations by Martin (1997) and Diederichs et al. (2010). In this section, the measure of interest was the  $d_f$  as it is the value to compare with Equation (2-4). Figure 5-14 shows the comparison between this investigation and the empirical relationship by Diederichs et al. (2010). The  $\sigma_{UCSinput}$  was assumed to be the  $\sigma_{ci}$  value from the equation. The results showed that the IMASS method follows the empirical trends observed. The relationship between  $\sigma_{max}/\sigma_{ci}$  with  $R_f/a$  was linear as suggested in the literature, with a slope slightly less steep than anticipated. This held until the stress reached  $\sigma_{max}/\sigma_{ci} > 2$ , as shown in Figure 5-14. At this point, the failure becomes uncontrolled, and the model cannot reach equilibrium. In this investigation, this happened when  $\sigma_1 = 83$  MPa and  $\sigma_3 = 15$  MPa, which gave an upper limit of the stress level at which the IMASS method can operate. If the induced stress expected is two times the  $\sigma_{ci}$  of the rock, the IMASS method cannot longer anticipate the failure expected. At this stress level, rockburst is the expected condition; therefore, dynamic analysis is a more adequate method. For any stresses lower than this threshold, the IMASS method produces results that can be interpreted and applied to the design.



**Figure 5-14 Stress SA for the IMASS method at different hypothetical stress regimes compared to the  $R_f$  equation proposed Diederichs et al. (2010) and showing the maximum  $\sigma_{max}/\sigma_{ci}$  threshold at which the model becomes unstable.**

### 5.5 PRELIMINARY SET OF GUIDELINES FOR THE USE OF THE IMASS METHOD

Using the results from the previous investigation, a preliminary set of guidelines was proposed for using the IMASS method. This guidelines apply to *FLAC3D* v 9.166 and above, previous version of the software might yield different results. The concepts and recommendations for the CWFS and DISL methods were also used to improve the proposed guidelines. For the effective use of the IMASS method, the following recommendations are made:

1. The IMASS method should only be used when the Hoek-Brown method is not applicable. It only applies to situations where the field  $GSI > 85$
2. The  $GSI_{input}$  should be entered as 99. This is not a reflection of the true characteristics of the field rock mass but a manipulation of the constitutive model to obtain the desired peak and post-peak failure envelopes.
3. The  $\sigma_{UCS_{input}}$  for the model should be the laboratory  $\sigma_{ci}$  of an intact rock specimen. If the  $\sigma_{ci}$  of the laboratory specimen is not known, then the input value can be estimated as 40% to 50% of the laboratory  $\sigma_{UCS}$ .
4. The  $\sigma_t$  for the model can be the measured tensile strength in the lab for intact rock.

5. The  $m_{input}$  should be such that the peak strength envelope follows a constant deviatoric stress. The recommended values are from 0.01 to 2 (0 is not a valid input)
6. The  $\phi_b$  should be high enough to make the post-peak failure envelope follow the spalling limit of the rock mass. It is recommended to be between  $40^\circ$  and  $60^\circ$ , with higher values for crystalline rock masses with more angular grains.
7. The  $e_{multi}^{ps}$  should be kept at 1 if the zones are small enough to reduce the effect of mesh-dependent failure.
8. The stiffness  $E_{input}$  should be entered as the measured laboratory  $E$  of the intact rock.
9. If the maximum induced stress is expected to be higher than two times the  $\sigma_{ci}$ , the IMASS method does not produce valid results. At this stress level, an alternative rock-bursting modelling method is recommended.

The previous guideline can serve as a starting point for the modelling of underground excavations. The user should understand the limitations and the simplification that the continuum method entails when dealing with these problems. They are only meant to estimate the depth and shape of failure around underground excavations and do not estimate displacements or dilation of the rock mass. These guidelines should be understood as preliminary and a starting point for a more in-depth investigation.

## **5.6 APPLICATION OF THE IMASS METHOD TO THE QIREHATAER DIVERSION TUNNEL**

The IMASS methods should be tested in other case scenarios to be validated as a useful tool for design. Another case scenario where spalling was observed and documented can be used to test the method and the proposed guidelines. The QDT case scenario is detailed in Zhao et al. (2017) and Zhao et al. (2022). It has all the characteristics necessary to be modelled with the IMASS method. The tunnel was excavated in strong rock,  $\sigma_{UCS} = 100$  MPa, with a high  $GSI$ , 80 to 85. All the required parameters for using the IMASS method are known from the field investigations (Zhao et al., 2017; Zhao et al., 2022). For this section, the QDT was modelled using the IMASS method. First, an initial set of parameters for input were defined according to the guidelines provided in the previous section. Then, the results were calibrated according to the field observations until an adequate match was found.

### 5.6.1 Methodology

The guidelines proposed in the previous section were followed to replicate the field observations at the QDT. From field observations, the  $GSI$  of the rock mass around the QDT was rated at 80 to 85 (Zhao et al. 2022). While at the lower limit of the guidelines, it was still used to model this case. The rock mass parameters for the gneissic granite for the QDT site are detailed in Table 5-9. The  $\sigma_{UCS}$  was found to be 100 MPa; however, there was also a detailed investigation into  $\sigma_{ci}$  which is on average 45 MPa so this value was used for the  $\sigma_{UCS_{input}}$ . The  $\sigma_t$  was found to be 8 MPa. The  $m_{i_{input}}$  was kept at the midpoint of the suggested values, i.e. 1. The rock is granite, therefore a  $\phi_b = 50^\circ$ , was an adequate initial value (Walton, 2019). The  $e_{multi}^{ps}$  was kept at one as small zones ( $d < 2.5$  cm) were used around the tunnel boundary. The stiffness in the laboratory experiments was measured at  $E = 20$  GPa (Zhao et al, 2022). A summary of the input parameters is shown in Table 5-10. The induced elastic stresses are expected to be lower than 90 MPa, therefore the IMASS method is still valid.

**Table 5-9 Geotechnical properties of the gneissic granite at the QDT (after Zhao et al., 2017; Zhao et al., 2022)**

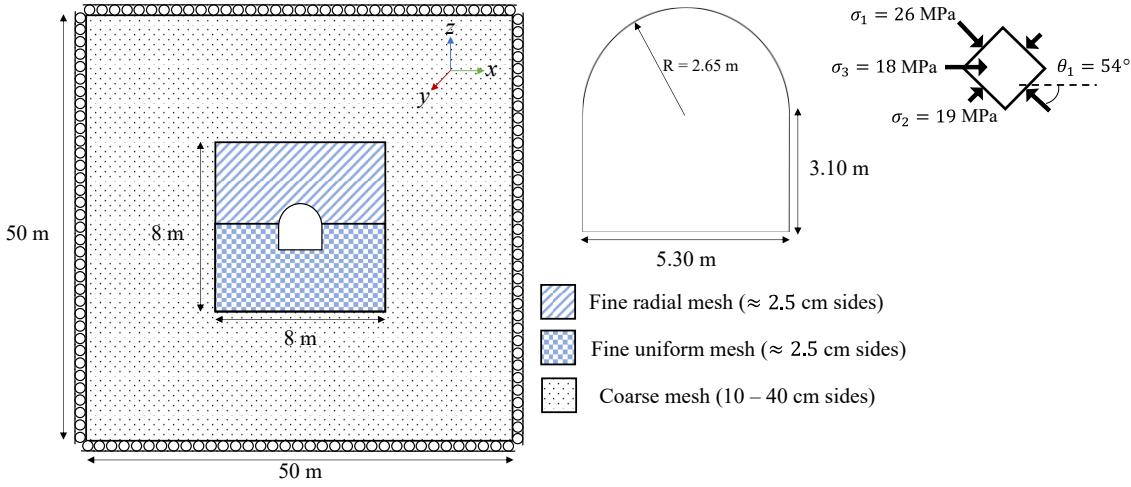
Parameter	Value
$GSI$	80-85
$\sigma_{UCS}$	100 MPa
$\sigma_{ci}$	45 MPa
$\sigma_t$	8 MPa
$E$	20 GPa

**Table 5-10 Preliminary estimates of the input parameters to simulate the QDT using the IMASS method**

IMASS method input parameter	Value
$GSI_{input}$	99
$\sigma_{UCS_{input}}$	45 MPa
$m_{i_{input}}$	1
$e_{multi}^{ps}$	1
$\phi_b$	$50^\circ$
$\sigma_t$	8 MPa
$E_{input}$	20 GPa

The modelling was done using *FLAC3D* (V9.166). To simplify the computing time, a 2.5D plane strain model was made. The model consists of an arched back tunnel with a width of 5.30 m and a height of 5.75 m. The stress regime was [26, 19, 18] MPa, with the tunnel

being driven parallel to the  $\sigma_3$  direction with  $\sigma_1$  having a plunge of  $54^\circ$ , similar to the stress rotation investigated in Chapter 3.2. The outer boundary of the model is 50 m by 50 m in the  $x$  and  $z$ -directions, with the model extending one zone in the  $y$ -direction. As it is a plane strain model, the zones' velocities were fixed in the  $y$ -direction, and roller boundaries were applied at the model's top, bottom, and sides. A structured mesh was used, with small zones (2.5 cm per side) near the excavation boundary and larger zones (up to 40 cm per side) near the outer boundary. The circular part of the tunnel was meshed with radial zones, while the square part was meshed with uniform zones. Figure 5-15 shows the model setup for the QDT simulation. To excavate the tunnel, the 'zone relax' command was used to achieve static equilibrium in the model without creating artificial failure of zones from instantaneous excavation.

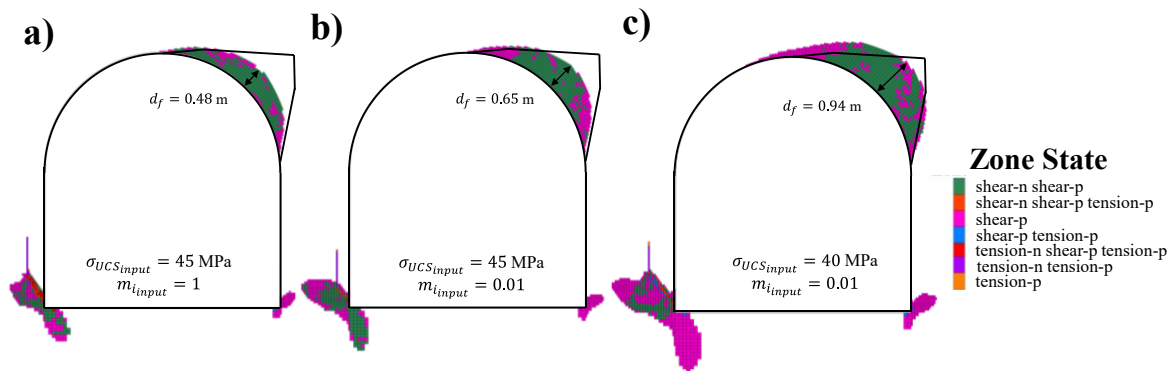


**Figure 5-15 Numerical model setup for the QDT tunnel using the IMASS method in 2.5D, with the direction and magnitude of the principal stresses shown, the excavation size, the mesh parameters, and boundary conditions.**

**5.6.2 Calibration and Results**

With the input strength parameters from Table 5-10, the depth of spalling is underestimated. Figure 5-16a shows the comparison between the model results and the field observations. At the QDT, a maximum failure of 1 m from the excavation boundary was observed, the IMASS method resulted in  $d_f = 0.48$  m. The input parameters can be calibrated to increase the  $d_f$  to match the QDT. Using the ranges provided before, certain parameters were reduced. The first decreased parameter was  $m_{input}$ . It was changed from 1 to 0.01. The simulation yielded a  $d_f = 0.65$  m, which still underestimated. Figure 5-16b is the modelling results with the

updated  $m_{i_{input}}$ . Another iteration of strength reduction is required to find a better estimate of failure. The next parameter that was reduced was the  $\sigma_{UCS_{input}}$ . The measured  $\sigma_{ci}$  was an average from 10 laboratory experiments (Zhao et al. 2022), it was reduced as to reflect a lower  $\sigma_{ci}$ . The  $\sigma_{UCS_{input}}$  used for the next iteration was 40 MPa. With this new updated parameters, the  $d_f$  found was 0.96 m. There was still an underestimation of the  $d_f$ , but as seen in Figure 5-16c the expected failure was matched to an acceptable degree of accuracy. As seen in the MBE investigation from the previous section, when the  $d_f$  was matched, the angle of failure was slightly overestimated. The shape of failure for all models did produce the expected v-shape, it instead presented a semi-circular failure.



**Figure 5-16 Initial results and calibration of the QDT tunnel using the IMASS method with change in  $\sigma_{UCS_{input}}$  and  $m_{i_{input}}$  where a)  $\sigma_{UCS_{input}} = 45$  MPa and  $m_{i_{input}} = 1$  b)  $\sigma_{UCS_{input}} = 45$  MPa and  $m_{i_{input}} = 0.01$  c)  $\sigma_{UCS_{input}} = 40$  MPa and  $m_{i_{input}} = 0.01$**

The model presented some failure around the bottom left corner of the excavation. This was not reported in the field investigation of QDT (Zhao et al., 2017; Zhao et al., 2022). Yet, this zone failure does not invalidate the results of the model. Two reasons can be proposed to explain the difference between model and field observations. The first one is that the model presents a failure within the rock mass, not at the excavation surface, that could not be visible in the field. Failure of this sort can only be monitored via acoustic emission, which was not done during the construction of the QDT. The second explanation is that continuum numerical models overestimate stresses around sharp corners. This generates artificial numerical failure that extends due to the nature of the IMASS constitutive model.

## 5.7 CONCLUSIONS AND RECOMMENDATIONS

A new method for simulating brittle rock failure around underground excavations was proposed and investigated. The method uses the IMASS constitutive model and the theory of DISL and CWFS to simulate spalling. The method works by having two distinct strength envelopes. The first one, before failure, is the damage initiation envelope dominated by the  $\sigma_{ci}$  strength. The second one, after plasticity, is the spalling limit, dominated by a high  $\phi$  and low  $c$ . The transition between these two strength envelopes is a function of the plastic shear strain. What this allows for is that at certain confinement levels, the rock mass transitions from brittle behaviour to perfectly plastic. This behaviour has been noted as characteristic of brittle rock. The principles were applied to the MBE at the URL to test the IMASS method. It demonstrated the capacity of the method to replicate field observations. By adjusting some of the strength parameters the  $d_f$  was estimated within 3 cm of the case scenario. To better develop the method, all input parameters of strength were investigated. The  $\sigma_{UCS_{input}}$  was found to be the parameters with the largest effect on the failure profile. The  $e_{multi}^{ps}$  was found to be a value that when incorrectly modified can produce uncontrolled numerical failure of the model. Different hypothetical stress regimes were also tested to determine the method's viability in representing failure in multiple possible scenarios. This investigation proposed an initial set of guidelines for using the IMASS method. These guidelines use the rock's laboratory strength to determine the model's input parameters. An alternative case study, the Qirehataer Diversion Tunnel, was modelled to test them. The guidelines used with the suggested values underestimated the  $d_f$  of this scenario. Model calibration following these guidelines found an adequate match between the field observations and simulation results.

The proposed use of the IMASS constitutive model for brittle failure is just one of its possible applications. Other uses of the constitutive model can be applied, such as using the equivalent Hoek-Brown envelope to represent the s-shape envelope as proposed by Bewick et al. (2019). Another technique to use the IMASS method is to define the depth of failure by the  $sloss$  parameter rather than the state of the zone. It can be argued that a failed zone does not mean that the rock has unravelled and detached, it could mean that it has started fracturing (Perras and Diederichs, 2016). Therefore, a better measure of failure is if it has fully



unravelling and started bulking, which occurs at  $s_{loss} = 0$ . These two possible interpretations can also be explored simultaneously for a different use of the IMASS constitutive model.

While this study thoroughly explored the method, further application and validation are needed to prove its viability. The two cases used here are not enough of a sample size to determine if the method can be used for design. Furthermore, only failure was explored for this model. For the complete design of underground excavations in brittle rock, displacement is crucial. This is particularly true when support systems are the goal of the design (Kaiser et al. 2000). As proposed here, the method only determines the HDZ, which is just the initial step for DGR design. The extent of all parts of the EDZ is necessary for further understanding. The IMASS method can be expanded to include a way to determine other EDZ characteristics.

## CHAPTER 6 - CONCLUSION

The simulation of brittle rock behaviour around underground excavations is crucial for the design and construction of DGR. As permanent nuclear waste storage facilities, their design needs to be well understood, and their construction must be closely monitored, as failure of such structures can lead to significant negative impacts on the environment and human health. Any underground excavation disturbs the ground and the stress regime it is built on. This disturbance of rock is termed the Excavation Damage Zone (EDZ), and it is a crucial aspect of the design of a DGR. The EDZ in brittle rock has two main sections of interest. The first one is the HDZ or spalling zone, which involves the unravelling of the rock and occurs nearest to the excavation boundary. It is also referred to as the spalling or v-notch zone. The second one is the EDZ<sub>SI</sub>, which is deeper into the rock mass and disturbs the rock by changing its structural and hydrogeological characteristics (Siren et al. 2015). Many means of modelling the EDZ, particularly its associated spalling, have been proposed. Generally, the approaches to do so can be divided into four broad categories: empirical methods, continuum numerical methods, discontinuum numerical methods, and hybrid finite-discrete numerical methods. Within each category, multiple approaches have been developed. No one method can be proposed as the perfect means of modelling the EDZ; instead, the designer must decide which approach better suits their situation and expertise. This thesis summarizes some of the common and validated approaches found in the literature.

### 6.1 SENSITIVITY ANALYSIS AND ROBUSTNESS EVALUATION OF THE CWFS AND DISL APPROACHES

Two of the most prominent continuum numerical modelling approaches, CWFS and DISL, were investigated in detail to increase the understanding of such methods and provide insight into future uses on the effects of parameter selection for each approach. The investigation applied both methods to a common case study, the MBE at the URL, using the latest version of the continuum numerical software *FLAC* (v 8.10.484). The aim was to obtain a simple and objective means to interpret the response of the modelled excavation. The simulated failed zone was compared to the field observations using different measures of failure such as the depth of failure, angle of failure, area of failure, and shape of failure. A parametric sensitivity analysis was conducted on each strength input parameter for both methods. Both approaches were also applied to different fictitious stress scenarios to test their capability to reproduce

the empirical observations by Martin et al. (1999). From this investigation the following observations were made

- The CWFS approach can represent the empirical observations of brittle failure with easy to interpret results.
- The CWFS approach is a more robust method that can be applied by rock practitioners for initial stages of the design process and construction monitoring.
- The DISL approach yields hard-to-interpret results that require a high level of numerical modelling expertise as well as subjective interpretation of the results.
- The detailed investigation also addressed the gaps in the literature by analyzing each parameter in isolation, giving potential users a better understanding of parameter selection and its effects.
- It was found that the dilation angle is a key parameter for both approaches, where a non-zero dilation is required to obtain an easy-to-interpret failure profile.

The CWFS method was applied to a different case study, the Qirehataer Diversion Tunnel in China. With the guidelines provided by Walton (2019) and calibration, it was shown that this method can accurately represent spalling failure around this tunnel. The guidelines gave an initial set of values to match the field observations. To calibrate the model the  $c_r$  and  $\phi_i$  were reduced to determine the most suitable strength values to simulate the QDT. This calibration process increased understanding of the impact of strength parameters on the modelling outcomes for the CWFS approach. It also helped validate and improve the guidelines. The guidelines can be updated to account for the values selected in this investigation and reassessed to find a better correlation between rock mass characterization and CWFS input parameter selection. The investigation showed the steps necessary to effectively and adequately use this method.

## **6.2 DEVELOPMENT AND EVALUATION OF THE IMASS APPROACH**

This dissertation also proposed a novel method to simulate spalling in brittle rock excavation using the IMASS constitutive model in *FLAC3D* (v 9.166 or higher). This approach uses the ideas developed for the DISL and CWFS methods to create two distinct failure envelopes (Damage Initiation envelope and Spalling Limit envelope) using the IMASS strength parameters. First, the modification of the constitutive model was investigated in detail using

unconfined and confined compression tests simulated in single zone elements. Once understood, the method was applied to two case scenarios, the MBE and the QDT. The effect of each parameter was also explored, which showed that the  $\sigma_{UCS_{input}}$  is a critical parameter for the use of the method. The  $m_i$  has a lesser effect on the failure extent, while  $\phi_b$  has a minimal effect on the extent of failure. From the development of this method, it was found that:

- The IMASS constitutive model can be modified to represent failure envelopes similar to the ones proposed for the DISL approach at low confinements.
- The relationship between plastic parameters of the IMASS constitutive model were explored in ways seldom found in literature, increasing the understanding of this complex constitutive model.
- With appropriate parameter selection and calibration, spalling can be accurately simulated.
- An initial set of guidelines were proposed for the future use of the method.
- Thanks to its assumptions and in-built logic the parameter selection and calibration for the IMASS method is more constrained than that for the CWFS and DISL methods.

### **6.3 RECOMMENDATIONS AND FUTURE WORK**

The work described in this thesis expanded some of the most prominent continuum numerical modelling approaches for predicting brittle failure around underground excavations. A new approach using the Itasca constitutive model was also proposed for the same purpose. However, there are still some gaps in the research that can be better explored. Some suggestions for future work on this topic are:

- The topic and literature of EDZ modelling can be better explored with a systematic literature review. Many methods, some explored in Chapter 2, have been proposed, each with benefits and drawbacks. No extensive and comprehensive investigation has been done on the topic. Therefore, a systematic review can help create an objective means to analyze and compare all methods proposed to date so that rock engineers can decide which method is best for their purposes.

- A Monte Carlo Simulation (MCS) can assess risk around underground excavations in brittle rock. Rock mass strength parameters such as the  $\sigma_{UCS}$ ,  $\sigma_{ci}$ ,  $\phi$ ,  $c$  and  $e_{crit}^{PS}$  are obtained via repeated laboratory testing and are better described as probabilistic parameters, not deterministic values (Martin and Christiansson, 2009). Furthermore, there is always uncertainty between the laboratory measurements and the actual in-situ rock mass conditions. As such, the parameters required to apply the CWFS guidelines by Walton (2019) can be considered probabilistic distributions. Having multiple pertinent distributions for each parameter and an MCS could better represent this scenario's possible range of outcomes. An investigation of this type would first require determining the most appropriate distributions for each strength parameter, e.g. normal distribution, uniform distribution, exponential, etc. Then, the failure characterization scheme proposed in Chapter 3 and Chapter 4 can be automated to determine the numerical values of the failure profile on each realization. With that, the distributions of  $d_f$ , angle of failure and area of failure are found, giving a probabilistic failure profile to use for risk assessment of underground excavation in brittle rock.
- Continuum numerical methods can be modified to better represent the HDZ and spalling. One of the main drawbacks of the continuum numerical models is their inability to demonstrate unravelling explicitly. In these models, failed elements are still part of the continuum and can hold stress, even if small. This is not the case in the field, as there is no actual material in the v-shape notch formation. A new approach or scheme can be developed using the existing methods (CWFS, DISL, or IMASS) in which the yielded elements are no longer considered within the continuum, explicitly simulating the v-shape notch formation and the final equilibrium state.
- The initial guidelines suggested by Walton (2019) are the outcome of the compilation of multiple uses of the CWFS method in the literature. The method can be used and calibrated to more case studies to improve those guidelines. The calibrated values used from these studies can then be added to the linear regression analysis conducted by Walton (2019) to refine the guidelines. However, this was done with the QDT tunnel in Chapter 4; more scenarios in different rock types can be found in the literature and simulated with the CWFS method and the guidelines.

- A better determination of the entire EDZ profile can be devised. Most of the approaches detailed in Chapter 2, particularly the continuum-based ones, mainly focus on determining HDZ and the depth of spalling. However, for DGRs, the entire EDZ profile is of interest. The EDZ extends further into the rock mass than just the HDZ. It is suggested that in the EDZ<sub>SI</sub> the hydraulic conductivity of the rock mass is affected by the initiation of microfractures that have yet to interact and create spalling (Tsang et al., 2005). For a DGR, this change in hydraulic conductivity is key, as the transport of radionuclides into the water table is controlled by this change in hydraulic conductivity. Some investigation can be conducted into determining how numerical models can be used to determine this change in hydraulic conductivity. Hybrid continuum-discontinuum numerical models are an ideal tool for this task as they can explicitly replicate the fracturing process, which can later be related to porosity and permeability within the rock mass.

## BIBLIOGRAPHY

- Ahn, J., Apted, M.J., (2010) Geological repository systems for safe disposal of spent fuels and radioactive waste. Woodhead Publishing Series in Energy: Number 9.
- An, H., Liu, H., Han, H., (2020) Hybrid Finite-discrete element modelling of excavation damaged zone formation process induced by blast in deep tunnel. *Advances in Civil Engineering* 2020.
- Atkinson, B.K. (1987) *Fracture Mechanics of Rock*. Department of Geological Sciences University College London.
- Azocar, K.D. (2016) Investigating the mesh dependency and upscaling of 3d grain-based models for the simulation of brittle fracture processes in low-porosity crystalline rock. Thesis for Master of Applied Science, Queens University.
- Baratta, A.J. (2010) The role of nuclear power in the reduction of greenhouse gas emissions in: Apikyan, S., Diamond, D., (eds) *Nuclear Power and Energy Security*. Springer, Dordrecht, The Netherland. pp 79- 88.
- Barton, N., Shen B., (2017) Risk of shear failure and extensional failure around over-stressed excavation in brittle rock. *Journal of Rock Mechanics and Geotechnical Engineering* 9: 210-225.
- Bewick, R.P., Kaiser, P.K., Amann, F. (2019) Strength of massive to moderately jointed hard rock masses. *J Rock Mech Geotech Eng* 11: 562-575
- Bossart P., Meier P.M., Moeri A., Trick T., Mayor J.C. (2002) Geological and hydraulic characterization of the excavation disturbed zone in the Opalinus Clay of the Mont Terri Rock Laboratory. *Engineering Geology* 66(1-2):19-38
- Cai, M., (2008) Influence of stress path on tunnel excavation response – Numerical tool selection and modeling strategy. *Tunnng Underground Space Technology* 23(6): 618-628
- Cai, M., Kaiser, P. K. (2004) Numerical simulation of the brazilian test and the tensile strength of anisotropic rocks and rocks with pre-existing cracks. *SINOROCK2004 Symposium. International Journal of Rock Mechanics and Mining Sciences* 41(3)
- Cai M, Kaiser P.K. (2014) In-situ Rock Spalling Strength near Excavation Boundaries. *Rock Mechanics Rock Engineering* 47: 659-675.
- Corkum, A.G., Lorig L.J., DeGagne D.O., (2012) Continuum representation of brittle rock failure bulking-induced displacement around tunnels. *46th U.S. Rock Mechanics / Geotechnical Symposium 2012* 3: 2194-2202.
- Cundall, P.A. (1971) A computer model for simulating progressive large scale movements in blocky rock systems. *Proceedings of the Symposium of International Society of Rock Mechanics* 1:II-8.
- Cundall P.A., Strack O.D.L. (1979) A discrete numerical model for granular assemblies. *Geotechnique* 29(1):47–65.
- Diederichs, M.S. (2007) The 2003 Canadian Geotechnical Colloquium: Mechanistic interpretation and practical application of damage and spalling prediction criteria for deep tunnelling. *Canadian Geotechnical Journal* 44 1082-1116.

- Diederichs, M.S., Carter, T., Martin, C.D., (2010). Practical Rock Spall Prediction in Tunnels. Proceeding of the ITA World Tunnel Congress Vancouver.
- Diederichs, M.S., Martin C.D., (2010) Measurements of spalling parameters from laboratory testing in : Zhao, J., Labiouse, V., Dudt, J.P., Mathier, J.F. (eds.) Rock Mechanics in Civil and Environmental Engineering. Taylor & Francis Group London, United Kingdom. pp 322-326
- Dressel E.J., Diederichs M.A., (2022) A numerical investigation on the influence of rockmass parameters and yield mechanics in pillar design. 1st RocScience International Conference 492-498.
- Edelbro, C., (2009) Numerical modelling of observed fallouts in hard rock masses using an instantaneous cohesion-softening friction-hardening model. Tunnelling and Underground Space Technology 24: 398-409
- Edelbro, C., (2010) Different Approaches for Simulating Brittle Failure in Two Hard Rock mass Cases: A Parametric Study. Rock Mechanics and Rock Engineering 43(2): 151-165
- Elfving, M., Evins, L.Z., Gontier, M., Graham, P., Matersson, P., Tunbrant, S., (2013) SFL concept study Main Report. Technical Report TR-13-14. SKB.
- Garza-Cruz, T.V., Peirce, M., Kaiser, P.K. (2014) Use of 3DEC to study spalling and deformation associated with tunnelling at depth. Deep Mining 2014.
- Geomechanica Inc. (2017) IRAZU 2D/3D Finite-Discrete Element Software Package
- Germanovich, L.N., Dyskin, A.V. (2000) Fracture mechanism and instability of openings in compression. International Journal of Rock Mechanics and Mining Sciences 37: 263-284.
- Ghazvinian, E., Diederichs, M.S., Quey, R., (2014) 3D random Voronoi grain-based models for simulation of brittle rock damage and fabric-guided micro-fracturing. Journal of Rock Mechanics and Geotechnical Engineering 6 506-521
- Ghazvinian, E., Garza-Cruz, T., Bouzeran, L., Fuenzalida, M., Cheng, Z., Cancino, C., Pierce, M., (2020) Theory and Implementation of the Itasca Constitutive Model for Advanced Strain Softening (IMASS). Proceedings of the Eight International Conference on & Exhibition on Mass Mining.
- Gerogiannopoulos, N.G., (1976) A critical state approach to rock mechanics. PhD Thesis. University of London.
- Hajiabdolmajid, V.R. (2001) Mobilization of strength in brittle failure of rock. PhD thesis, Queen's University, Kingston, Canada
- Hajiabdolmajid V., Kaiser P.K., Martin C.D., (2002) Modelling brittle failure of rock. International Journal of Rock Mechanics and Mining Sciences 39(6): 731-741.
- Hajiabdolmajid, V., Kaiser, P.K., Martin, C.D. (2003). Mobilized strength components in brittle failure of rock. Geotechnique 53(3): 327-336.
- Hamdi, P. (2015) Characterization of brittle damage in rock from the micro to macro scale. Doctor of Philosophy Thesis, Simon Fraser University.
- Hamdi, P., Stead, D., Elmo, D., (2017) A review of the application of numerical modelling in the prediction of depth of spalling damage around underground openings. 51st U.S. Rock Mechanics Symposium. ARMA-2017-0778.



- Hamediazad, F., Bahrani, N., (2024) Evaluation of the rock mass strength for hard rock pillars design using bonded block models. *Rock Mechanics and Rock Engineering*.
- Hoek, E., (1965) *Rock Fracture Under Static Stress Conditions*. CSIR Report MEG 383, National Mechanical Engineering Research Institute, Council for Scientific and Industrial Research, Pretoria, South Africa
- Hoek, E., (1968) Brittle fracture of rock in: Stagg, K.G., Zienkiewicz O.C. (eds.) *Rock Mechanics in Engineering Practice*. John Wiley and Sons, Lincoln, United Kingdom, pp 99-124.
- Hoek, E., (2002) *Practical Rock Engineering*. RocScience.
- Hoek, E., Brown E.T., (1980) Empirical strength criterion for rock masses. *Journal of Geotechnical Engineering* 106: 1013-1035.
- Hoek, E., Brown E.T., (2018) The Hoek-Brown failure criterion and GSI – 2018 edition. *Journal of Rock Mechanics and Geotechnical Engineering* 11(3): 445-463.
- Hoek, E., Carranza-Torres C, Corkum B, (2002) Hoek-Brown failure criterion – 2002 edition. *Proceeding NARMS-TAC Conference, Toronto* 1: 267-273.
- Hoek, E., Diederichs, M.S., (2006) Empirical estimation of rock mass modulus. *International Journal of Rock Mechanics & Mining Sciences*. 43: 203-215
- Hoek, E., Martin, C.D., (2014) Fracture initiation and propagation in intact rock – A review. *J. Rock Mech. Geotech. Eng.* 6(4): 287-300.
- Igraffea, A.R., (1989) Theory of crack initiation and propagation in rock in: Atkinson, B.K., (eds.) *Fracture Mechanics of Rock*. Department of Geological Sciences University College London.
- Itasca Consulting Group (2015) *FLAC Basics: An introduction to FLAC8 and a guide to its practical applications in geotechnical engineering*. Revision 01 Itasca Consulting Group.
- Itasca Consulting Group (2019) *PFC Documentation: flat-jointed model*.
- Itasca Consulting Group (2023) *FLAC2D Version 9.0 Continuum Modelling for Geomechanics*.
- Itasca Consulting Group (2024) *3DEC 9.0 Documentation*.
- Kaiser, P.K., Diederichs, M.S., Martin C.D., Sharp, J., Steiner, W. (2000) Underground works in hard rock tunnelling and mining. *Geoteng* 2000(1) 841-926
- Kelsall, P.C., Case, J.B., Chabannes, C.R. (1984) Evaluation of Excavation-induced Changes in Rock Permeability. *International Journal of Rock Mechanics & Geomechanics Abstracts* 21(3) 123-135.
- Kirsch, G., (1898) *Die Theorie der Elastizität und die Bedürfnisse der Festigkeitslehre*. *Zeitschrift des Vereines deutscher Ingenieure*. Ingenieure, 42, 797–807.
- Klerck, P.A., Sellers, E.J., Owen, D.R.J., (2004) Discrete fracture in quasi-brittle materials under compressive and tensile stress states. *Computer Methods in Applied Mechanics and Engineering* 192: 10387-10407.
- Li Y, Bahrani N (2021a) A continuum grain-based model for intact and granulated Wombeyan marble. *Computers and Geotechnique* 129:103872.
- Lan H., Martin C.D, Hu B., (2010) Effect of heterogeneity of brittle rock on micromechanical extensile behaviour during compression loading. *J. Geophys. Res.* 115, (B01) 202.

- Li Y., Bahrani N. (2021) Strength and failure mechanism of highly interlocked jointed pillars: insight from upscaled continuum grain-based models of a jointed rock mass analogue. *Computers and Geotechnique* 137:104278.
- Lisjak, A., Grasselli, G., (2014) A review of discrete modeling techniques for fracturing processes in discontinuous rock masses. *Journal of Rock Mechanics and Geotechnical Engineering* 6 301-314. *Engineering* 193 3035-3056.
- Lorig, L.J., Varona, P., (2013) Guidelines for numerical modelling of rock support for mines. in Y Potvin & B Brady (eds), *Ground Support 2013: Proceedings of the Seventh International Symposium on Ground Support in Mining and Underground Construction*, Australian Centre for Geomechanics, Perth, 81-105.
- Marinos, P., Evert H. (2000). GSI: a geologically friendly tool for rock mass strength estimation. *ISRM International Symposium*, Melbourne, Australia, 2000, 1422-1446
- Martin, C.D. (1994) The strength of massive Lac du Bonnet granite around underground opening. Ph.D. thesis, Department of Civil Engineering, University of Manitoba, Winnipeg, Man.
- Martin, C.D. (1995) Brittle rock strength and failure: Laboratory and in situ. *Proceedings of the 8th ISRM Congress*. 1033-1040.
- Martin, C.D. (1997) Seventeenth Canadian Geotechnical Colloquium: The effect of cohesion loss and stress path on brittle rock strength. *Canadian Geotechnical Journal*, 34(6): 698-725.
- Martin, C.D., (1997). The effect of cohesion loss and stress path on brittle rock strength. *Canadian Geotechnical Journal* 34(5): 698 - 725.
- Martin C.D., Christiansson R., (2009) Estimating potential for spalling around a deep nuclear waste repository in crystalline rock. *International Journal of Rock Mechanics & Mining Sciences*
- Martin, C.D., Kaiser P.K., (1996) Mine-by experiment committee report Phase 1: excavation response summary and implications. AECL-11382, COG-95-347
- Martin, C.D., Kaiser, P.K., McCreath, D.R., (1999) Hoek-Brown parameters for predicting the depth of failure around tunnels. *Canadian Geotechnical Journal* 36(1): 136-151
- Martin C.D., Read, R.S., Martino, J.B. (1997) Observation of brittle failure around a circular test tunnel. *International Journal of Rock Mechanics and Mining Sciences* 34(7) 1065-1073
- Munjiza, A. (2004) *The combined finite-discrete element method*. Chichester, UK: JohnWiley & Sons Ltd.
- Munjiza, A., Owen, D.R.J., Bicanic, N., (1995) A combined finite-discrete element method in transient dynamics of fracturing solids. *Engineering Computations* 112(2) 145-174
- Ojovan, M.I., Lee, W.E., Kalmykov, S.N. (2019) *An introduction to Nuclear Waste Immobilization*. Third Edition. Elsevier, London, United Kingdom.
- Paterson, M.S., (1958) Experimental deformation and faulting in wombeyan marble. *Bulletin of the Geological Society of America*
- Perras, M.A., Diederichs, M.S., (2016) Predicting excavation damage zone depths in brittle rocks. *Journal of Rock Mechanics and Geotechnical Engineering* 8 60-74.

- Potyondy, D.O. (2015) The bonded-particle model as a tool for rock mechanics research and application: current trends and future directions, *Geosystem Engineering*, 18(1), 1-28
- Potyondy, D.O., Cundall, P.A. (2004) A bonded-particle model for rock. *International Journal of Rock Mechanics & Mining Sciences* 41 1329-1364.
- Potyondy, D.O., (2024) A 3D Subspring Network Breakable Voronoi model for rock: laboratory-scale behavior. 58th US Rock Mechanics/Geomechanics Symposium ARMA 24-493
- Potyondy, D.O., Mas Ivars, D., (2020) Simulating spalling with flat-jointed material. 5th International Itasca Symposium – Applied Numerical Modeling in Geomechanics Paper: 03-01
- Potyondy, D.O., Pruvance M.D., (2024) A 3D Subspring Network Breakable Voronoi model for rock: grain-breakage scheme. 6th International Itasca Symposium on Applied Numerical Modeling in Geomechanics: 04-01
- Ramirez N., Delonca A., (2023) Influence of geotechnical parameters and in-situ stresses on strainburst potential. *Proceedings of the Rocscience International Conference (RIC 2023)*
- Rasmussen, L.L. (2021) Hybrid lattice/discrete element method for bonded block modeling of rock. *Computers and Geotechnics* 130: 103907.
- Rasmussen, L.L. (2022) A breakable grain-based model for bi-modular rock. *International Journal of Rock Mechanics & Mining Science*. 51: 105028.
- Read, R.S., Chandler, N.A. (1997) Minimizing excavation damage through tunnel design in adverse stress conditions. *Proceedings of the International Tunnelling Association World Tunnel Congress, Vienna*. Vol. 1. A.A. Balkema, Rotterdam, pp. 23–28.
- Read, R.S., Chandler, N.A., Dzik, E.J., (1998) In Situ Criteria for Tunnel design in Highly-stressed Rock Masses. *Int. J. Rock Mech. Min. Sci.* 35(3): 261-278.
- Renani R.H., Martin C.D (2018) Cohesion degradation and friction mobilization in brittle failure of rocks. *International Journal of Rock Mechanics and Mining Sciences* 106: 1-13
- Rinne, M., Shen, B., Lee, H.S (2004) Aspo Pillar stability Experiment: Modelling of fracture development of APSE by FRACOD. SKB R-04-04
- Rockfield Software (2024) ELFEN 2D/3D numerical modelling package.
- RocScience, (2022) RS2 User Guide. RocScience Inc.
- Sanipour, S., Bahrani, N., Corkum, A.G., (2022) Simulation of Brittle Around Canada's Mine-By Experiment Tunnel Using 2D Continuum-Based Voronoi Tessellated Models. *Rock Mechanics and Rock Engineering* 50(10): 6387-6408.
- Shen, B. (2014) Development and Applications of rock fracture mechanics modelling with FRACOD a general review. *Geosystems Engineering* Vol 17, No.4, 235-252.
- Sinha, S., Walton, G., (2020) A study on Bonded Block Model (BBM) complexity for simulation of laboratory-scale stress-strain behaviour in granitic rocks. *Computers and Geotechnics*. 118: 103363
- Sinha, S., Walton, G. (2021) Integration of three-dimensional continuum model and two-dimensional bonded block model for studying the damage in a granite pillar at the

- Creighton Mine, Sudbury, Canada. *Journal of Rock Mechanics and Geotechnical Engineering* 13 275-288
- Siren, T., Kantia, P., Rinne, M. (2015) Considerations and observations of stress-induced and construction-induced excavation damage zone in crystalline rock. *International Journal of Rock Mechanics & Mining Sciences* 73 165-174.
- Starfield, A.M., Cundall, P.A., (1999) Towards a Methodology for Rock Mechanics Modelling. *Int. J. Rock Mech. Min. Sci.* 31 25(3) 99-106
- Tatone B.S.A., Grasselli, G., (2015) A calibration procedure for two-dimensional laboratory-scale hybrid finite-discrete element simulations. *International Journal of Rock Mechanics and Mining Sciences* Volume 75: 56-72
- Tsang, C.F., Bernier, F., Davies, C. (2005) Geohydromechanical processes in the Excavation Damaged Zone in crystalline rock, rock salt, and indurated and plastic clays—in the context of radioactive waste disposal. *International Journal of Rock Mechanics & Mining Sciences* 42 109-105.
- Walton, G., (2019) Initial guidelines for the selection of input parameters for cohesion-weakening-friction-strengthening (CWFS) analysis of excavations in brittle rock. *Tunn. Undergr. Space Technol.* 84, 189-200.
- World Nuclear Association (2022) Radiation and Health Effects. Obtained, February 26, 2024 from: <https://world-nuclear.org/information-library/safety-and-security/radiation-and-health/radiation-and-health-effects.aspx>
- Xu, D.P., Huang, X., Li, S.J., Xu, H.S., Qiu, S.L., Zheng, H., Jiang, Q., (2022) Predicting the excavation damage zone within brittle surrounding rock masses of deep underground caverns using a comprehensive approach integrating in situ measurements and numerical analysis. *Geo. Front.* 13 101273.
- Zhao, X.G., Cai, M., (2010) A mobilized dilation angle model for rocks. *Int. J. Rock Mech. Min. Sci.* 31 47(3): 368-384.
- Zhao, X.G., Cai, M., (2010) Influence of Plastic Shear Strain and Confinement-dependent rock dilation on rock failure and displacement near an excavation boundary. *Int. J. Rock Mech. Min. Sci.* 31 47(5): 723-738.
- Zhao G., Wang D., Gao B., Wang S. (2017) Modifying rock burst criteria based on observations in division tunnel. *Engineering Geology* 216 153-160
- Zhao G., Wang D., Shi L. (2022) Influences of EDZ and cross-section shapes on spalling failure depth of non-circular tunnels in gneissic granite. *Geotech Geol Eng*